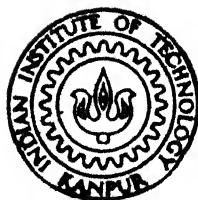


# CLASSICAL AND SEMICLASSICAL MICROSCOPIC APPROACHES FOR HEAVY - ION FUSION REACTIONS

*by*

SUBODH S. GODRE

TH  
PHY/1988/D  
PHY 6548 C  
1988  
D  
GOD  
CLA



DEPARTMENT OF PHYSICS

INDIAN INSTITUTE OF TECHNOLOGY, KANPUR

AUGUST, 1988

# **CLASSICAL AND SEMICLASSICAL MICROSCOPIC APPROACHES FOR HEAVY - ION FUSION REACTIONS**

*A Thesis Submitted*

In Partial Fulfilment of the Requirements  
for the Degree of

**DOCTOR OF PHILOSOPHY**

*by*

**SUBODH S. GODRE**

*to the*

**DEPARTMENT OF PHYSICS**

**INDIAN INSTITUTE OF TECHNOLOGY, KANPUR**

**AUGUST, 1988**

106281

PHY-1988-D-GOD-GLA

*DEDICATED*

*TO*

*MY PARENTS*



## CERTIFICATE

Certified that the work presented in this thesis entitled, "Classical and Semiclassical Microscopic Approaches for Heavy-Ion Fusion Reactions" is the original work of Mr. S. S. Godre carried out under my supervision.

This work has not been submitted elsewhere for a degree.



( Y. R. Waghmare )  
PROFESSOR OF PHYSICS

Department of Physics  
Indian Institute of Technology  
Kanpur 208016 , INDIA

## ACKNOWLEDGEMENTS

I express my deepest sense of gratitude and indebtedness to Professor Y.R. Waghmare for his valuable guidance, keen interest, and stimulating discussions during the course of this work. He provided me with necessary manoeuvrability and freedom, albeit keeping a watchful eye on the progress. I am also grateful to him and his family for making me always feel at home throughout my stay in I.I.T., Kanpur.

I am also sincerely thankful to Dr. V.S. Ramamurthy of B.A.R.C. Bombay for taking a keen interest in my work and for many fruitful discussions. I also wish to thank Prof. J.R. Nix of Los Alamos Laboratory, Los Alamos, Prof. S.P. Pandya of Physical Research Laboratory, Ahmedabad, Dr. B.K. Jain of B.A.R.C., Bombay and Dr. S.K. Sharma of I.I.T. Kanpur for their interest in my work and for useful discussions.

It is indeed a pleasure and my duty to thank my senior colleague Dr. T.K. Mani from whom I learned a lot about the computational methods in heavy-ion reaction studies. I also thank him for numerous discussions. Thanks are also due to Dr. A.K. Dutta for many helpful discussions. I also thank my colleague Mr. R. C. Misra for his help.

I learnt a number of tricks in better utilization of the computers from the discussions with my colleagues and friends Dr. G. Mukherjee, Dr. Pradeep Khowash, Mr. Rajan R. Rane, and Mr.

Siddhartha Sen. I sincerely thank them for their help. The cooperation and assistance of the staff of the Computer Centre of I.I.T. Kanpur is also gratefully acknowledged.

I take this opportunity to record my thanks to Drs. Arvind Agarwal, B. Ghosh, J.R. Govindrajan, Krishna Kumar, P.K. Rath, M.M. Sharma, B.R. Srinivasan, Prabhat Thakur, Dr(Ms) R. Venkataraman, Ms. Mythili, and Messers Ashish Agarwal, D. Bahuguna, Alok Banerjee, Subrato Banerjee, Ajit Jaiswal, U.C. Johri, R.R. Mishra, Bipin B. Pande, P.K. Raina, G. Ravi Kumar, S.C. Sivasubramaniam, Raghava Varma, and Vinay Kumar for their cooperation and help in various forms during the course of this work. I would specially like to thank Messers G. Ravi Kumar, Raghava Varma, and Vinay Kumar for their kind help in proof-reading, *word-smithing* and final preparation of the thesis.

Thanks are also due to Mr Ghanshyam Rao Hoshing for skillfully typing-in the manuscript.

Finally, I do record my deep sense of gratitude to my Parents and all the members of my family for their cheerful cooperation and endless encouragement.

S.S. Godre

## TABLE OF CONTENTS

CHAPTER	PAGE No.
CERTIFICATE	ii
ACKNOWLEDGEMENTS	iii
TABLE OF CONTENTS	v
LIST OF TABLES	x
LIST OF FIGURES	xii
SYNOPSIS	xx
 1. INTRODUCTION	 1
1.1 Heavy-Ion Reactions as a Nuclear Probe	1
1.2 Classification of Heavy-Ion Collisions	4
1.3 Theoretical Approaches and Motivations for the Present Work	7
REFERENCES	15
2. CALCULATIONAL DETAILS OF THE CLASSICAL-MICROSCOPIC APPROACH	19
2.1 Introduction	19
2.2 Construction of the Nuclei in the Ground-States	21
2.2.1 Algorithms	21
(a) "DYNAMIC" Cooling Procedure	21
(b) "STATIC" method	23
2.2.2 Frozen Ground-States	26
2.3 Two-Body Potentials	27

2.4	Collision Calculations	28
2.4.1	Initial Conditions	28
2.4.2	Trajectory Calculations	30
2.5	Fusion Cross Section Calculations	31
2.5.1	Definition of Fusion	31
2.5.2	Expressions for Fusion Cross Sections	37
2.5.3	Initial Relative Random Orientations and Statistical Averaging	38
	REFERENCES	41
3.	CLASSICAL-MICROSCOPIC CALCULATION OF FUSION CROSS SECTIONS FOR THE $^{16}\text{O}+^{16}\text{O}$ REACTION WITH THE LENNARD- JONES FORM OF NN POTENTIAL	43
3.1	Introduction	43
3.2	Importance of the Correct Initial Conditions	45
3.3	Dependence of Fusion Cross Sections on the Ground-State Nuclear Properties	50
3.4	Summary and Discussions	53
	REFERENCES	56
4.	CLASSICAL-MICROSCOPIC CALCULATIONS FOR $^{16}\text{O}+^{16}\text{O}$ AND $^{40}\text{Ca}+^{40}\text{Ca}$ REACTIONS WITH A SOFT-CORE GAUSSIAN FORM OF THE NN POTENTIAL	57
4.1	Introduction	57
4.2	Fusion Cross Section Calculations	60

4.2.1	The $^{16}\text{O}+^{16}\text{O}$ Reaction	60
	Systematic Study of the Dependence of Fusion Cross Sections on the Range of The NN Potential	
4.2.2	The $^{40}\text{Ca}+^{40}\text{Ca}$ Reaction	72
4.2.3	Discussions	80
4.3	Heavy-Ion Collisions at High Energies	86
4.3.1	$\ell$ -Window for Fusion	86
4.3.2	Sideward-Flow of Nuclear Matter	92
4.4	Summary and Conclusions	97
	REFERENCES	100
5.	THE EFFECTS OF THE FINITE SIZE OF NUCLEONS	103
	("FROZEN" WAVE-PACKET CALCULATIONS)	
5.1	Introduction	103
5.2	Calculational Details	105
5.2.1	Description of a nucleon	105
5.2.2	Assumptions	106
5.2.3	Equations of Motion	108
5.2.4	Ground-State Properties of Nuclei	109
5.2.5	Potentials and Forces	113
5.3	Results and Discussions	116
5.3.1	The case of $r_N = 0.8$ fm	116
	(a) Effects of the Finite Size On	117
	(i) Coulomb and NN Potentials	117
	(ii) Nuclear Compressibility	121
	Coefficient	
	(iii) Nuclear Density Distribution	123

	(iv) Fusion Cross Sections	126
	(b) An Equivalent-Radius Point Particle Calculation	128
	(c) Inclusion of Zero-Point Energy	129
5.3.2	The Case of $r_N = 1.4$ fm	134
	(a) Effects of the Finite Size On	134
	(i) Coulomb and NN Potentials	134
	(ii) Nuclear Compressibility Coefficient	136
	(iii) Nuclear Density Distribution	136
	(iv) Fusion Cross Sections	138
	(b) Inclusion of the Zero-Point Energy	139
5.4	Summary and Conclusions	140
	REFERENCES	142
6.	SEMICLASSICAL MICROSCOPIC APPROACH WITH GAUSSIAN WAVE PACKETS	143
6.1	Introduction	143
6.2	Calculational Details	144
6.2.1	Nucleon Wave Packets	144
6.2.2	Many Particle Nuclear Wave-Function and Nuclear Hamiltonian	146
6.2.3	Determination of $\sigma$	148
6.2.4	Two-Body Potentials	153
6.2.5	Ground State Solution of Many-Body Systems	154
6.2.6	Dynamic Evolution of a Many-Particle Gaussian Wave Packet System	156

6.3	Results and Discussions	160
6.3.1	Study of a Two-Body System	160
	(a). Case of $v_{12} = 0$	162
	(b) Case of $v_{12} \neq 0$	163
6.3.2	Study of a Many-Body System	166
	(Ground State of $^{16}\text{O}$ )	
6.4	Summary and Conclusions	176
	REFERENCES	180
APPENDIX A	INITIAL COULOMB TRAJECTORIES OF HEAVY-IONS	181
APPENDIX B	EVALUATION OF DOUBLE-FOLDING INTEGRALS FOR THE TWO-BODY POTENTIALS	185



## LIST OF TABLES

TABLE	PAGE NO
3.1 Parameters of the Lennard-Jones Potential (eq. 3.1 and the calculated binding energies and rms radii of $^{16}\text{O}$ for different calculations.	51
4.1 Parameters of the effective NN Potential (eq. 4.1) and the calculated binding energy and rms radius of $^{16}\text{O}$ in the ground-states with different potentials.	61
4.2 Ratios of the Principal Moments of Inertia in the ground-states of $^{16}\text{O}$ with different potentials.	62
4.3 Average values of the static-barrier parameters for the $^{16}\text{O}+^{16}\text{O}$ system ( $b=0$ ) with different potentials	70
4.4 Parameters of the potential (eq. 4.1) and the calculated binding energy and rms radius of $^{40}\text{Ca}$ in the ground-states with different potentials	73
5.1 Parameters of the effective NN potential and the calculated ground-state properties of $^{16}\text{O}$	118

- 5.2 Fusion cross sections for the  $^{16}\text{O}+^{16}\text{O}$  reaction 130  
at  $E_{\text{CM}} = 16.7\text{MeV}$  with different potentials.
- 5.3 The ground-state properties of  $^{16}\text{O}$  and the 132  
parameters of the effective NN potentials  $\langle W1 \rangle$   
and  $\langle W2 \rangle$  modified to include zero-point kinetic  
energy in the binding energy.
- 6.1 Parameters of the effective NN potential and the 169  
ground-state properties of  $^{16}\text{O}$

## LIST OF FIGURES :

FIGURE	CAPTION	PAGE No.
1.1	Schematic diagram showing heavy-ion trajectories at different impact parameters corresponding to different reactions. (Ref. 18)	5
2.1	Schematic diagram depicting specification of the initial conditions for heavy-ion collision calculations in the centre-of-mass frame.	29
2.2	C.M. trajectories of one of the $^{16}\text{O}$ nuclei in the $^{16}\text{O}+^{16}\text{O}$ reaction (with the potential P3 referred in Chapter 4) at $E_{\text{CM}} = 66.8$ MeV and different impact parameters.	34
2.3	Relative distance ( $R_{\text{CM}}$ ) between the centres-of-mass of two ions as a function of time for the $^{16}\text{O}+^{16}\text{O}$ reaction at $E_{\text{CM}} = 66.8$ MeV and different impact parameters.	35
2.4	Time evolution of the kinetic energy in the relative motion ( $T_{\text{CM}}$ ) for the $^{16}\text{O}+^{16}\text{O}$ reaction at $E_{\text{CM}} = 66.8$ MeV and different impact parameters.	36

- 2.5 The nucleon coordinate projections of  $^{16}\text{O}$  and  $^{40}\text{Ca}$  39  
nuclei in various orientations (with the Potential  
P3 referred in Chapter 4).
- 3.1 Centre-of-mass trajectories of one of the  $^{16}\text{O}$  ions 47  
in the  $^{16}\text{O}+^{16}\text{O}$  reaction with the initially correct  
Coulomb trajectories at (A)  $E_{\text{CM}} = 16.7$  MeV; and  
(B)  $E_{\text{CM}} = 66.8$  MeV. (A') and (B') are the  
initially straight line trajectories for the two  
energies respectively.
- 3.2 Calculated fusion cross sections for the  $^{16}\text{O}+^{16}\text{O}$  49  
reaction  
 □ - potential L1 and initially Coulomb trajectories;  
 ◆ - potential L1 and initially straight line  
 trajectories (L1');  
 + - potential L2, which reproduces ground-state  
 properties of  $^{16}\text{O}$ . Calculated points with different  
 potentials and initial conditions are connected to  
 guide the eye. Experimental data are shown by  
 ○ (Ref. 6), X (Ref. 7), Δ (Ref. 8), ◆ (Ref. 9),  
 ■ (Ref. 10), and ∇ (Ref. 11).
- 3.3 Plots of Lennard-Jones potential for the parameter 52  
sets L1 and L2 given in Table 3.1.
- 4.1 Pair-distribution in the ground-state configurations 63  
of  $^{16}\text{O}$  with the potentials P1, P2 and P3.

- 4.2 The effective NN potential (eq. 4.1) with the 65  
different values of  $r_0$  and the other parameters  
given in Table 4.1.
- 4.3 Fusion cross section Vs.  $E_{CM}^{-1}$  for the  $^{16}O+^{16}O$  66  
reaction with the potentials P1, P2 and P3. For a  
given potential the calculated points at different  
values of  $E_{CM}^{-1}$  are connected with straight lines to  
guide the eye. Experimental data <sup>are</sup> shown by  $\circ$  (Ref.  
8),  $\times$  (Ref. 9),  $\Delta$  (Ref. 10),  $\blacklozenge$  (Ref. 11),  $\blacksquare$  (Ref.  
12) and  $\nabla$  (Ref. 13).
- 4.4 Static fusion barrier for the  $^{16}O+^{16}O$  reaction with 68  
the potential P3.
- 4.5 Fusion cross section Vs.  $E_{CM}^{-1}$  for the  $^{16}O+^{16}O$  71  
reaction. The solid line is the prediction of the  
static 1-dimensional potential model (eq. 4.2) with  
the barrier parameters for the reaction given in  
Table 4.3 for the potential P3. Dashed curve  
shows the prediction of the dynamical calculations.
- 4.6 Fusion cross section Vs.  $E_{CM}^{-1}$  for the  $^{40}Ca+^{40}Ca$  75  
reaction with the potentials P3 and P4.  
Experimental data are shown by  $\circ$  (Ref. 14),  $\Delta$  (Ref.  
15) and  $\square$  (Ref. 16).
- 4.7 Plot of the effective NN potentials P3 and P4. 77

- 4.8 Comparison of the pair-distributions in the ground-state of  $^{40}\text{Ca}$  with the potential P3 and P4. Pair-distribution of  $^{16}\text{O}$  with the potential P3 is also shown. 78
- 4.9 The coordinate-projections of the  $^{16}\text{O}+^{16}\text{O}$  collision at  $E_{\text{CM}} = 66.8$  MeV and  $b = 5.4$  fm. The time  $T$  in each frame is in the unit of  $10^{-22}$  sec.. 82
- 4.10 The binding energy <sup>per nucleon</sup> Vs. the rms radius of the compressed or the expanded configurations of  $^{16}\text{O}$  with the potentials P1, P2 and P3. 85
- 4.11 Same as in Figure 4.9 but for  $E_{\text{CM}} = 150$  MeV and  $b = 0.0$  fm. 88
- 4.12 Same as in Figure 4.9 but for  $E_{\text{CM}} = 200$  MeV and (a-c) 89-91  
(a)  $b = 0.0$  fm, (b)  $b = 1.0$  fm and (c)  $b = 3.0$  fm.
- 4.13 The coordinate-projections of the  $^{40}\text{Ca}+^{40}\text{Ca}$  collision at  $E_{\text{CM}} = 418$  MeV/nucleon and  $b = 0.0$  fm. The time  $t$  is in the unit of  $10^{-22}$  sec. 93
- 4.14 Same as in Figure 4.13 but the Figure shows a superposition of the coordinate-projections of the reaction for six initial-orientations of the colliding nuclei. 94
- 4.15 Same as in Figure 4.14 but for  $b = 4.5$  fm. 96

- 5.1 The effective Coulomb potential (eq. 5.29) for 119  
gaussian wave-packets with  $r_N = 0.8$  fm and  $1.4$  fm  
are compared with the Coulomb potential (eq. 5.25)  
between two point charges ( $r_N=0$  fm)
- 5.2 Comparison of the effective NN potential  $\langle W1 \rangle$  for 120  
gaussian wave-packets ( $r_N = 0.8$  fm) to a potential  
 $W1$  with the same parameters but for point particles  
( $r_N = 0$  fm). The potentials  $\langle W1 \rangle$  and  $W1$  are  
compared with the potential  $P3$  for point particles  
also.
- 5.3 Comparison of the effective NN potential  $P3$  and  $P5$  122  
for point particles and potential  $\langle W1 \rangle$  for gaussian  
wave-packets with  $r_N = 0.8$  fm. Parameters of the  
potentials are given in Table 5.1.
- 5.4 Calculated radial density distributions  $\rho(r)$  of 124  
nucleons in the ground-state of  $^{16}\text{O}$  with the  
potential  $\langle W1 \rangle$  ( $r_N = 0.8$  fm) and with the potential  
 $\langle W2 \rangle$  ( $r_N = 1.4$  fm).
- 5.5 Radial distribution  $n(r)$  of the position of the 125  
point particles or the centroids of the wave-packets  
in the ground-state of  $^{16}\text{O}$  with the potential :  
(a)  $P3$  for point nucleons, (b)  $\langle W1 \rangle$  for gaussian  
wave-packets with  $r_N = 0.8$  fm, (c)  $P5$  for point  
nucleons; and (d)  $\langle W2 \rangle$  for wave-packets with  $r_N =$   
 $1.4$  fm.

- 5.6 Comparison of the calculated fusion cross sections 127  
for the  $^{16}\text{O}+^{16}\text{O}$  reaction with the potential P3 and  
potential  $\langle W1 \rangle$  with  $r_N = 0.8$  fm.
- 5.7 Comparison of the effective NN potentials  $\langle W1 \rangle$  and 133  
 $\langle W2 \rangle$  for the gaussian wave-packets with  $r_N = 0.8$  fm  
and 1.4 fm, respectively, and the corresponding  
potentials  $\langle W1+ \rangle$  and  $\langle W2+ \rangle$  with the inclusion of the  
corresponding constant zero-point energies.
- 5.8 Plots of the potentials P3 for point particles and 135  
the potentials  $\langle W1 \rangle$  and  $\langle W2 \rangle$  for the gaussian  
wave-packets with  $r_N = 0.8$  fm and 1.4 fm,  
respectively.
- 5.9 Plot of the potentials W1 and W2 with the parameters 137  
of the respective potentials  $\langle W1 \rangle$  and  $\langle W2 \rangle$  but for  
the case of  $\sigma = 0$ .
- 6.1 Some configurations of the 3-dimensional gaussian 152  
wave-packets in the simple cases of  $A = 2, 3$ , and 4.  
The points shown are the sites where the centroids  
of the wave-packets are located and the numbers are  
the width ( $\sigma$ ) of the corresponding wave-packets in  
fm.; the length  $a$  is equal to 1.0 fm.



- 6.2 Potential  $\langle v_{12}^N \rangle$ , Q.M. kinetic energy  $T_{QM}$  and 165  
 $(\langle v_{12}^N \rangle + T_{QM})$  for two wave-packets versus the centroid  
separation  $R_{12}$  for the parameters  $V_O = 3200$  MeV,  
 $C = 0.8$  fm, and  $r_O = 1.2$  fm.
- 6.3 Time evolution of the centroid positions  $R_1$  and  $R_2$ , 167  
centroid separation  $R_{12}$  and the width  $\sigma_1$  and  $\sigma_2$  of  
the two wave-packets with the potentials shown in  
the Figure 6.2.
- 6.4 The distribution  $(n(\sigma))$  of the number of 170  
wave-packets with widths  $\sigma$  in the ground-state of  
 $^{16}O$  for the potential given in the Table 6.1.
- 6.5 The distribution  $(n(r))$  of the number of 171  
wave-packets with their centroids located at radius  
 $(r)$  in the ground state of  $^{16}O$ .
- 6.6 Calculated radial density  $(\rho(r))$  of nucleons in the 172  
ground-state of  $^{16}O$ .
- 6.7 Plot of the average kinetic energy per nucleon 174  
 $(\langle T \rangle / A)$ , average potential energy per nucleon  
 $(V/A)$ , and the total energy per nucleon versus rms  
radius  $(R)$  of the compressed or expanded  
configurations of  $^{16}O$  around  $R = R_{gs}$ .

- 6.8 Potential  $\langle v_{12}^N \rangle$ , Q.M. kinetic energy  $T_{QM}$  and 175  
( $\langle v_{12}^N \rangle + T_{QM}$ ) Vs. the centroid separation  $R_{12}$  in  
the case of a two wave-packet system with the  
potential given in Table 6.1.
- A.1 Schematic diagram showing the Coulomb trajectory of 182  
one of the ion in the centre-of-mass reference  
frame. C and C' are the two focii of the hyperbola  
that corresponds to the trajectory of the ion.

## SYNOPSIS

### CLASSICAL AND SEMICLASSICAL MICROSCOPIC APPROACHES FOR HEAVY-ION FUSION REACTIONS

SUBODH S. GODRE

Ph. D.  
Department Of Physics  
Indian Institute of Technology, Kanpur

August, 1988

In heavy-ion collisions nuclei are subjected to much stronger perturbations than it is possible with the lighter projectiles, which opens up channels for new reaction processes. At projectile energies of the order of a few MeV/nucleon, reaction processes such as deep-inelastic scattering and fusion dominate, which involve large scale rearrangement of nucleons and transfer of energy from the relative motion to the internal excitations. In this thesis a study of heavy-ion fusion reactions in the classical-microscopic approach and the formulation of a semiclassical-microscopic approach are presented. The thesis consists of six chapters. Problems and motivations for the present work are discussed in the first chapter along with an overview of the heavy-ion reactions and a brief account of the various theoretical approaches.

In the classical-microscopic approach nucleons are considered as classical point particles interacting via suitable two-body forces. The ground-states of the individual nuclei used in the collision calculations are first obtained by either

proper choice of the parameters of the NN potential, calculated fusion cross sections for  $^{16}\text{O}+^{16}\text{O}$  and  $^{40}\text{Ca}+^{40}\text{Ca}$  reactions agree well with the experiments. At incident energies above a certain threshold, Time-Dependent Hartree-Fock (TDHF) calculations predict the existence of an l-window for heavy-ion fusion reactions - for which there is no conclusive experimental evidence so far. It is shown in chapter 4 that l-window for fusion does not exist in the classical-microscopic approach. Calculations in this approach at still higher energies show the experimentally observed "side-splash" of nuclear matter in heavy-ion collisions - an effect that is completely absent in the TDHF calculations due to the neglect of two-body collisions.

Thus, we find that the classical-microscopic approach provides a good description of the heavy-ion fusion reactions, without requiring any additional assumptions such as those of frictional forces or shape parametrizations as in the case of macroscopic approaches. However, due to the explicit neglect of the zero-point energy we find that the effective NN potential has large repulsive-core, smaller depth and narrow width, which gives higher values of the compressibility coefficients. Also, due to the description of nucleons as point particles, the nuclei do not have continuous density distributions.

On the other hand, we know from the experiments that nucleons do have finite size which is not negligible compared to the average internucleon separation in the ground-states. Therefore, in chapter 5, we replace point nucleons by gaussian

cyclically minimizing the total potential energy of an initially-random distribution of nucleons with respect to small spatial displacements of individual nucleon coordinates or by a dynamic cooling method. The zero-point motion of nucleons in the ground-state configuration is explicitly neglected due to the problem of premature evaporation of nucleons from the nuclei. However, an effective nucleon-nucleon (NN) potential is used which correctly reproduces the ground-state binding energy and the rms radius. With the given initial conditions for collisions, trajectories of all the constituent nucleons are determined by numerically integrating coupled Newton's equations of motion. Nucleon trajectories thus obtained are then analyzed to find fusion cross sections. Details of this approach are given in chapter 2.

Fusion cross sections for some heavy-ion reactions, earlier calculated in this approach, are overestimated compared to the experimental data at lower energies. Taking  $^{16}\text{O}+^{16}\text{O}$  reaction as an example, these calculations are re-examined in chapter 3. We find that the above discrepancy was due to certain assumptions earlier made in the specification of the initial conditions; in particular due to the neglect of the Coulomb interaction between the colliding ions at far off distances. The use of Lennard-Jones form of the NN potential in the earlier calculations is also critically examined.

In chapter 4, a systematic study of the dependence of fusion cross sections on the range of a soft-core gaussian form of the NN potential shows that fusion cross sections are sensitive to the long-range attractive-tail of the NN potential. With a

wave-packets with "frozen" widths and find that the incorporation of the finite size of nucleons gives a smoother nuclear density distribution and smaller values of the compressibility coefficients compared to the point particle calculations. The effective NN potential has smaller repulsive-core and longer attractive-tail. However, due to the longer tails, calculated values of fusion cross sections for the  $^{16}\text{O}+^{16}\text{O}$  reaction are enhanced.

Finally, in chapter 6, we describe a semiclassical-microscopic approach in which it is assumed that the wave-packets always remain as gaussians, but the "frozen-width" assumption is removed. The width of every individual wave-packet is determined from the instantaneous configuration of the many wave-packet system by equating the zero-point energy of the wave-packets to the Thomas-Fermi kinetic energy in the local-density approximation. As a simple example we study the dynamics of a two wave-packet system which demonstrates the effects of the "Pauli-repulsion". We also find the ground-state of a many-body system. While reproducing the ground-state binding energy and the rms radius of  $^{16}\text{O}$  by adjusting the potential parameters, we find that the average kinetic energy per nucleon in the ground-state is also in close agreement with the experimental value. Thus, the effects of the "zero-point" energy and the "Pauli-repulsion" in the ground-state of the nuclei as well as in the dynamics of the wave-packets are explicitly incorporated in this approach, which can be used for the heavy-ion collision calculations.

## CHAPTER 1

### INTRODUCTION

#### 1.1 HEAVY-ION REACTIONS AS A NUCLEAR PROBE

The atomic nucleus was first discovered in 1911 in experiments conducted by Rutherford and his associates on scattering of  $\alpha$ -particles by atoms. Since then for a long time till seventies, much of the information on the structure and properties of nuclei was obtained by using light projectiles such as e, p, n, d, t,  $^3\text{He}$ ,  $\alpha$ -particles, and pions as probes with the reaction mechanisms such as elastic and inelastic scattering, compound nucleus reactions and direct reactions such as pick-up, break-up, stripping, charge-exchange, few nucleon transfer etc.<sup>1</sup> Only in the early seventies a variety of projectiles with heavier masses and a wide range of energies became available with the advent of heavy-ion accelerators.<sup>2</sup>

The main motivation for carrying out experiments with heavy-ion beams, however, was a desire to produce superheavy-elements.<sup>3</sup> The existence of superheavy-elements was predicted in 1966 by Myers and Swiatecki<sup>4</sup> using a liquid drop mass formula and the empirical shell corrections to the nuclear binding energy. Based on this model it was predicted that significant fission barriers exist for nuclei that lie near the magic numbers,  $Z=114$  and  $N=184$ . It was felt that the best way to produce superheavy-elements would be to try to fuse two heavy nuclei under such conditions that the

fused system would not break apart into pieces. However, all the experimental efforts to search for superheavy-elements in heavy-ion reactions have failed so far.<sup>5</sup>

Though, the discovery of superheavy-elements has still remained elusive, the availability of heavy-ion projectiles has opened up new frontiers in the study of nuclear matter. In heavy-ion collisions, nuclei are now subjected to much more severe perturbations than were earlier possible with the lighter projectiles. Heavy-ion projectiles colliding with light and heavy target nuclei bring along with them high values of charge, mass, kinetic energy and angular momentum, thus opening up channels for new reaction processes involving high charge and mass transfer, deep-inelastic collisions, or formation of a highly excited and rapidly spinning compound nucleus.<sup>6-8</sup>

So far it has not been possible to reach the predicted island of stability around the superheavy-elements in the periodic table. Nevertheless, with the help of various reactions involving heavy ions, some trans-uranium nuclei<sup>9</sup> and a large number of neutron-rich and proton-rich nuclei, far away from the line of beta-stability, have been produced, thus probing the limits of nuclear stability.<sup>10</sup> Involvement of large angular momenta in heavy-ion collisions is helpful in studying the limit of stability of nuclei under fast rotations and strong deformations.<sup>11,12</sup> In heavy-ion collisions at intermediate and high projectile energies, high densities and temperatures of nuclear matter are reached.<sup>13,14</sup> The behaviour of nuclear matter at varying



densities and temperatures can throw some light on the equation-of-state of nuclear matter<sup>13,14</sup> which, besides its intrinsic interest is also essential for the understanding of the properties of the astrophysical objects such as neutron stars. At very high relativistic energies one can form a hot superdense piece of nuclear matter with the possibility of a phase transition of the baryonic matter to a new phase of matter called the Quark-Gluon-Plasma.<sup>15-17</sup>

Thus, with the help of the new tools in the form of heavy ions at disposal, one can now reach those regions of nuclear physics which were not accessible in the past with the lighter projectiles. Apart from the domain of Nuclear Physics, heavy-ion collisions are also being used for studies in the domain of Atomic Physics, and also have important practical applications in ion-implantation techniques, semiconductor doping, radiation biology and therapy etc.<sup>2</sup>

Since heavy-ion systems have only few tens to few hundreds of nucleons depending on the target-projectile combinations, these systems are neither simple few-body systems nor many-body systems in the sense of a gas. Thus, theoretical understanding of the heavy-ion reaction phenomena also presents a challenging task. In section 1.2 we give a classification of heavy-ion reactions. Some of the approaches in studying heavy-ion collisions and motivations for the present study are discussed in section 1.3.

## 1.2 CLASSIFICATION OF HEAVY-ION COLLISIONS

A general physical description and the classification of the many processes occurring in heavy-ion collisions is given below. Overall features of heavy-ion collisions can be described by reference to Figure 1.1.<sup>18</sup>

At collision energies below the Coulomb-barrier the ions do not come in contact and interact only through the Coulomb field, resulting in Rutherford scattering and possibly Coulomb excitation of the target and projectile nuclei. Quantum mechanically some tunneling may take place leading to sub-barrier fusion.<sup>19</sup>

At energies above the Coulomb-barrier the ions can come closer and feel the strong nuclear potential. It then becomes more convenient to discuss the interaction in terms of the impact parameter ( $b$ ) and one can broadly classify different reactions as follows:

(1) If the impact parameter  $b$  is larger than the sum of the radii of the ions one again has only elastic Rutherford scattering and at the most Coulomb excitation processes.

(2) If  $b$  is comparable to the sum of the radii of the ions, a grazing collision takes place and the ions can be elastically or inelastically scattered, or a few nucleons can be transferred from one to the other. Such collisions are collectively referred to as "peripheral collisions".

(3) When  $b$  is reduced still further, the ions begin to interact very strongly, with a rapid loss of their energy and exchange of a

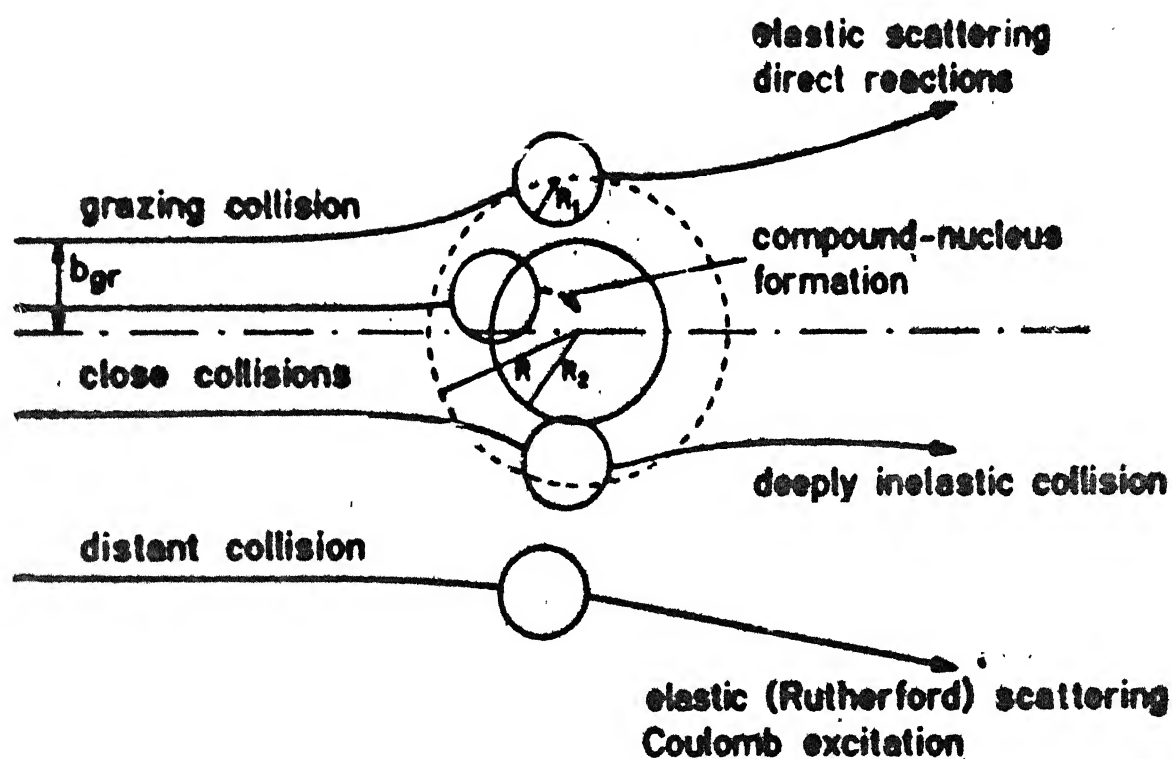


FIGURE 1.1 Schematic diagram showing heavy-ion trajectories at different impact parameters corresponding to different reactions. (Ref. 18)

large number of nucleons between the target and the projectile. Because of the strong damping of energy from the relative motion these processes are called deep-inelastic scattering. Such processes take place during the time intervals characteristic of the direct-reaction processes. In these reactions no fused systems are formed and the final product nuclei resemble the initial ones, but in highly excited states.<sup>20</sup>

(4) At still smaller values of the impact parameters, if  $b$  becomes equal to a critical value ( $b_{cr}$ ) for fusion to occur, then after losing much of their energy in the relative motion the two nuclei form a joint system that rotates like a dumb-bell and further energy is lost in mutual excitations. At impact parameters below this value the two nuclei fuse together, completely losing their relative kinetic energy and their individual identities. The highly excited fused system then loses its energy by particle evaporation and/or by fission processes after a time interval which is much longer compared to the interaction times involved in deep-inelastic scattering or direct reaction processes.<sup>21-23</sup>

At intermediate energies (of the order of 20-200 MeV/nucleon) the reaction processes are deep-inelastic collisions, incomplete fusion and fragmentation of the combined system into various nuclei.<sup>24</sup> In near central collisions ( $b \simeq 0$ ) at these energies; more violent reactions take place characterized by an almost complete disintegration of both the target and projectile nuclei. When the incident energy per nucleon is above the pion mass  $\simeq 140$  MeV, pion production may become increasingly appreciable.<sup>3,24,25</sup>

In very high ultra-relativistic heavy-ion collisions (a few tens of GeV/nucleon) the nuclear densities may rise so much that the nucleons overlap considerably, losing their identity and probably forming a Quark-Gluon-Plasma -experimental searches for which are still continuing.<sup>15-17</sup>

### 1.3 THEORETICAL APPROACHES AND MOTIVATIONS FOR THE PRESENT WORK

The de Broglie wavelength of a heavy-ion is given by

$$\lambda = \left[ \frac{h^2}{2 M E_{\text{lab}}} \right]^{1/2} \quad (1.1)$$

The wavelength of a typical heavy-ion projectile such as  $^{40}\text{Ca}$  at  $E_{\text{lab}} = 115 \text{ MeV}$  -an energy that is just sufficient to overcome the fusion barrier for the  $^{40}\text{Ca} + ^{40}\text{Ca}$  reaction - is about 0.42 fm, whereas the experimental rms radius of  $^{40}\text{Ca}$  is about 3.53 fm. Thus heavy-ions with energies even of the order of a few MeV/nucleon have short de Broglie wavelengths compared to the size of the ions. Therefore, classical approximations are expected to be good at least for the macroscopic features of heavy-ion reactions, such as fusion and deep-inelastic scattering, which dominate at low incident energies and involve large scale transfer of energy from the relative motion to internal excitations of the colliding nuclei.<sup>20-23</sup> Therefore, it has been common to use classical macroscopic approaches to study the collective motions in heavy-ion collisions.<sup>20-23,26-36</sup>

The macroscopic approaches are based on the assumptions of a continuous distribution of nuclear matter. In these calculations, therefore, one has to make a-priori choice of the relevant collective degrees of freedom describing the overall properties of the nuclei, such as separation between the ions, their shapes, neck elongation etc.<sup>20</sup> After choosing the relevant collective degrees of freedom one has to invoke suitable mechanisms, such as friction, for the transfer of energy from the collective degrees to the remaining internal degrees of freedom describing the motion of nucleons.

On the other hand, if one adopts a microscopic approach, which necessarily involves individual particle degrees of freedom, this energy transfer is determined automatically through the solutions of the time-dependent many-body equations; the relevant collective degrees of freedom are determined by the system itself. Exact solution of a quantum-mechanical many-body calculation would, of course, be ideal. But, even the best available approximate solution, such as the Time-Dependent Hartree-Fock (TDHF) calculation<sup>37-41</sup> which is based on the mean-field assumption and a single Slater determinant wave-function, poses an enormous computational problem due to the non-linear integro-differential nature of the equations involved. Practical calculations require further assumptions to be made and several symmetries to be imposed on the system. Furthermore, as the incident energy is increased two-body collisions become increasingly important and the TDHF approximation becomes invalid.

It has been felt necessary to incorporate two-body collisions in TDHF calculations even at relatively low energies<sup>42</sup> - such calculations pose even more computational difficulties. Therefore, classical microscopic approaches have also been considered which require orders of magnitude less computational effort compared to the TDHF calculations and are relatively clear in their interpretations.

There are two types of classical microscopic calculations based on different approaches. One of the classical-microscopic approaches is based on classical kinematics and Monte-Carlo methods.<sup>43-47</sup> In this approach, which is often called **Intranuclear Cascade model**, the nucleons are assumed to follow straight-line trajectories between scatterings. The result of each scattering is determined by Monte-Carlo methods according to the distance of closest approach of the two nucleons and the experimental values of the free N-N scattering cross sections. This approach necessarily requires the conditions of diluteness of the nuclear matter, such that the simultaneous interaction between more than two nucleons is explicitly excluded. The N-N interaction is replaced by the N-N scattering cross sections. Most of such calculations neglect binding energy effects and their application has been restricted to high energy collision calculations only, where two-body collisions become important and the binding energy can be neglected in comparison to the total energy. In similar Monte-Carlo framework, mean-field and Pauli blocking effects have been included recently through

the Vlasov-Uehling-Uhlenbeck approach.<sup>48-53</sup>

The second classical-microscopic approach is similar to the Molecular Dynamics method for the study of classical fluids and solids.<sup>54-59</sup> In this classical-microscopic approach nucleons in the colliding nuclei are considered as classical, spinless, point-particles and the simultaneous interaction between all pairs of nucleons is allowed through suitable two-body forces.<sup>60-77</sup> The effective two-body potential is chosen either to give good free N-N scattering cross sections or to yield reasonable properties for the nuclear ground-states. In a collision calculation, trajectories of the constituent nucleons are computed on the basis of the classical non-relativistic equations of motion and the forces between all the pairs of nucleons. The nucleon trajectories thus computed can be used to study any desired macroscopic properties of the collision.

While in this classical-microscopic (equations-of-motion) approach some of the limitations of the purely hydrodynamic approach<sup>13</sup>, such as, those of a local thermal equilibrium are avoided. At the same time hydrodynamics is automatically included as a limit.<sup>60,61</sup> Further, the diluteness condition assumed in the Monte-Carlo type classical-microscopic approaches is also not required. Since, at higher energies ( $E_{lab} > 100$  MeV/nucleon) the nucleon wavelengths ( $< 1$  fm) are comparable to, or smaller than the force range or the mean inter-particle separation, classical approximations are expected to be even better at such energies. Therefore, this approach has been extensively used in the study of



various aspects related to the formation and decay of the denser nuclear matter in high-energy (of the order of 100-800 MeV/nucleon) heavy-ion collisions.<sup>60-68</sup> Recently, this approach has also been used in the study of formation of composites in the disassembly of "hot-drops" of nuclear matter.<sup>69-71</sup>

Some efforts have been made to use this approach at lower energies ( of the order of a few MeV/nucleon ) also. Since, all the translational degrees of freedom of the constituent nucleons are explicitly included in this approach, there is no need to separate the dynamics of the collective degrees of freedom from the intrinsic degrees, as in the case of classical-macroscopic approaches. Thus, there is no need to make any assumptions about the shape of the nuclear surfaces or the width of the neck formed between the two nuclei at contact. Further, there is no need to make any assumptions about the frictional forces, as all the dissipation and transfer of energy arises due to the nucleon-nucleon collisions and are already built in the calculations.

Ramamurthy and Kataria<sup>72</sup> used this approach for a qualitative study of heavy-ion collisions at lower energy and found that most of the essential features of heavy-ion collisions such as fusion and deep-inelastic scattering are adequately brought out in this approach. Following the calculations of Ramamurthy and Kataria, Dixit et al<sup>73-75</sup> and Mani<sup>76</sup> calculated fusion cross sections for various heavy-ion reactions in this approach. While these calculations qualitatively reproduce the

general features of the experimental fusion excitation functions and give good agreements on the higher energy side, fusion cross sections are overestimated on the lower energy side just above the Coulomb barrier. These deviations are attributed to the possible breakdown of the classical approximations at such low energies. On the other hand even a simple classical one-dimensional static-potential model<sup>22,23,26,27</sup> reproduces fusion cross sections, precisely in this energy region - though such models fail at higher energies due to the increasing importance of dynamical effects which are neglected. Therefore, it is necessary to examine what is the real cause of the discrepancy between the experiments and the earlier classical-microscopic calculations.

The details of the classical-microscopic approach and fusion cross section calculations are given in chapter 2. Taking  $^{16}\text{O} + ^{16}\text{O}$  reaction as an example, we re-examine Dixit et al's calculations in chapter 3 and try to explain the cause of the overestimation of fusion cross sections at lower energies in their calculations. The use of Lennard-Jones potential as an NN interaction by Dixit et al in heavy-ion collision calculations is also critically examined in chapter 3.

Since a two-body potential and the ground-state nuclear properties are the central inputs to the classical-microscopic approach, it is desired to understand clearly how fusion cross sections depend on these inputs. While this approach allows for a systematic study of the repulsive-core of the effective NN potential in high-energy heavy-ion collisions,<sup>66,67</sup> a systematic

study of fusion of heavy-ions at lower energies may provide information about its long-range attractive tail. Therefore, a systematic study of the sensitivity of fusion cross sections on the range of a soft-core gaussian NN potential is carried out in chapter 4. There we calculate fusion cross sections for  $^{16}\text{O}+^{16}\text{O}$  and  $^{40}\text{Ca}+^{40}\text{Ca}$  reactions and compare them with the experimental data. In chapter 4 we also study the behaviour of heavy-ion collisions at higher energies. In particular, we examine the question of the existence of the l-window for fusion which is predicted by the TDHF calculations, and present some calculations which demonstrate the "sideward-flow" or "side-splash" of nuclear matter at even higher energies.

In chapter 5 we try to account for the finite size of nucleons, replacing the point nucleons of the classical-microscopic calculations by the "frozen" gaussian wave-packets. Taking two different values of the rms radius of the nucleons we study the effect of the finite size on the classical NN potential, nuclear density distributions, compressibility coefficient and heavy-ion fusion cross sections.

One of the difficult problems in the classical-microscopic approach is to explicitly incorporate the zero-point motion of nucleons in the nuclei and account for the "Pauli-repulsion" between the nucleons. Because of the classical nature of the approach and the quantum mechanical nature of the problem there does not seem to be any satisfactory solution to this problem within the framework of the classical-microscopic approach.

Therefore, in chapter 6 we finally describe a semiclassical-microscopic approach with gaussian wave-packets which removes the "frozen-width" assumption on the wave-packets made in chapter 5. This approach explicitly incorporates the effects of the zero-point energy and the "Pauli-repulsion" in the ground-state and in the dynamics of the wave-packets. Some simple calculations are also presented in chapter 6.

## REFERENCES

- 1 P.E. Hodgson, *Nuclear reactions and nuclear structure* (Clarendon Press, Oxford, 1971).
- 2 H.A. Grunder and F.B. Selph, *Ann. Rev. Nucl. Sci.* **27**, 353 (1977).
- 3 C.M. Ko, *Lect. notes in physics* (Springer-Verlag, Berlin 1981), Vol **145**, p.798.
- 4 W.D. Myers and W. Swiatecki, *Nucl. Phys.* **81**, 1, (1966).
- 5 G.N. Flerov and G.M. Ter-Akopian. *Treatise on Heavy-ion science*, edited by D.A. Bromley (Plenum, New York 1985), Vol.4, p.333; and references therein.
- 6 J.R. Huizenga, *Proc. deep-inelastic and fusion reactions with heavy-ions, Lect. notes in physics* (Springer-Verlag, Berlin, 1979) Vol.117, p. 1.
- 7 W. Nörenberg and H.A. Weidenmüller, *Introduction to the theory of Heavy-ion collisions*, 2nd edition, *Lecture notes in Physics*, (Springer-Verlag, Berlin, 1980), vol.51.
- 8 P.E. Hodgson, *Nuclear heavy-ion reactions* (Clarendon press, Oxford, 1978).
- 9 G.T. Seaborg and W.D. Loveland, see Ref.5, Vol.4, p. 255; and references therein.
- 10 P.G. Hansen, *Ann. Rev. Nucl. Part. Sci.* **29**, 69 (1979).
- 11 R.M. Diamond and G.J. Wozniak, *Ann. Rev. Nucl. Part. Sci.* **34**, 189 (1984).
- 12 I. Hamamoto, see Ref.5, Vol.3, p.313.
- 13 J.A. Maruhn and W. Greiner, see Ref.5, Vol.4, p. 565
- 14 H. Stöcker and W. Greiner, *Phys. Rep.* **137**, 277 (1986).
- 15 R. Rafelski, *Phys. Rep.* **88**, 331 (1982).
- 16 H. Satz, *Ann. Rev. Nucl. Part. Sci.* **35**, 245 (1985).
- 17 B. Sinha, *Proc. Int. Conf. on Nucl. Phys.*, Bombay, 1984, edited by B.K. Jain and B. Sinha (World Scientific) p 116.
- 18 W. Nörenberg, *J. Phys. (Paris)*, **37**, C5 (1976).

- 19 M. Beckerman, Phys. Rep. 129, 145 (1986).
- 20 W.U. Schröder and J.R. Huizenga, see Ref.5, Vol.2, p.115.
- 21 J.R. Huizenga, Ann. Rev. Nucl. Part. Sci. 33, 265 (1983).
- 22 U. Mosel, see Ref 5, Vol 2, p. 3.
- 23 C. Ngô, IL Nuovo Cimento, 81A, 47 (1984).
- 24 C.K. Gelbke and D.H. Boal, Prog. in Part. and Nucl. Phys. 19, 33 (1987); and references therein.
- 25 S. Das Gupta, see Ref 17, p. 70
- 26 H.H. Gutbrod, W.G. Winn and M. Blann, Nucl. Phys. A213, 267 (1973).
- 27 D. Glas and U. Mosel, Nucl. Phys. A 237, 429 (1973).
- 28 D.H.E. Gross, H. Kalinowski and J.N. De, Prod. Symp. on classical and Quantum Mechanical Aspects of Heavy-Ion Collisions, Lect. Notes in Phys. (Springer-Verlag, Berlin, 1974), Vol 33, p 194.
- 29 R. Bass, Phys. Rev. Lett. 39, 265 (1977).
- 30 D.H.E. Gross and H. Kalinowski, Phys. Lett. 48B, 302 (1974) Phys. Rep. 45, 175 (1978).
- 31 D.H.E. Gross, Nucl. Phys. A240, 472 (1975).
- 32 E. Seglie, I. Sperber and A. Sherman, Phys. Rev. C11, 122 (1975).
- 33 J.P. Bondorf, M.I. Sobel and I. Sperber, Phys. Rep. 15, 8 (1974).
- 34 J. R. Birkelund, L.E. Tubbs, J.R. Huizenga, J.N. De and D.Sperber, Phys. Rep. 56, 107 (1979).
- 35 S. Björnholm and W.J. Swiatecki, Nucl. Phys. A391, 471 (1982).
- 36 K.T.R. Davies, A.J. Sierk and J.R. Nix, Phys. Rev. C13, 238 (1976).
- 37 P. Bonche, S. Koonin and J.W. Negele, Phys. Rev. C13, 122 (1976).
- 38 H. Flocard, S.E. Koonin and M.S. Weiss, Phys. Rev. C17, 168 (1978).

- 39 P. Bonche, B. Grammaticos and S. Koonin, Phys. Rev. C17, 1700 (1978)
- 40 J.W. Negele, Rev. Mod. Phys. 54, 914 (1982); and references therein.
- 41 K.T.R. Davies, K.R.S. Devi, S.E.Koonin and M. Strayer, see Ref.5, vol.3, p.3; and references therein.
- 42 M. Tohyama, Phys. Lett. 160B, 235 (1985); Phys. Rev. C36, 18 (1987).
- 43 Y. Yariv and Z. Fraenkel, Phys. Rev. C20, 2227 (1979).
- 44 J.P. Bondorf, P.J. Siemens, S. Garpman and E.C. Halbert, Z. Phys. A279, 385 (1976).
- 45 J.P. Bondorf, H.T. Feldmeier, S. Garpman and E.C. Halbert, Phys. Lett. 65B, 217 (1976).
- 46 E.C. Halbert, Phys. Rev. C23, 295 (1981).
- 47 J. Cugnon, T. Mizutani, and J. Vandermeulen, Nucl. Phys. A352, 505 (1981).
- 48 G. Bertsch, H. Kruse, and S. Das Gupta, Phys. Rev. C29, 67 (1984).
- 49 H. Kruse, B.V. Jacak and H. Stöcker, Phys. Rev. Lett. 54, 289, (1985).
- 50 J. Aichelin and G. Bertsch, Phys. Rev. C31, 1730 (1985).
- 51 H. Kruse, B.V. Jacak, J.J. Molitoris, G.D. Westfall, and H. Stöcker, Phys. Rev. C31, 1770 (1985).
- 52 C.Gregoire, B. Remaud, F. Sebille, L. Vinet, and Y. Raffray Nucl. Phys. A465, 317 (1987).
- 53 G.E. Beauvais, D.H. Boal, and J.C.K. Wong, Phys. Rev. C35, 54 (1987).
- 54 B.J. Alder, J. Chem. Phys 33, 1439 (1960).
- 55 A. Rahman, Phys. Rev. 136, A404 (1964).
- 56 L. Verlet, Phys. Rev. 159, 98 (1967).
- 57 M. Parrinello and A. Rahman, Phys. Rev. Lett. 45, 1196 (1980).
- 58 J.Q. Broughton, J. Chem. Phys. 75, 5128 (1981).

- 59 W.G. Hoover, Ann. Rev. Phys. Chem. **34**, 103 (1983); and references therein.
- 60 A.R. Bodmer and C.N. Panos, Phys. Rev. **C15**, 1342 (1977); Nucl. Phys. **A356**, 517 (1981).
- 61 A.R. Bodmer, C.N. Panos and A.D. MacKellar, Phys. Rev. **C22**, 1025 (1980).
- 62 L. Wilets, E.M. Henley, M. Kraft and A.D. MacKellar, Nucl. Phys. **A282**, 341 (1977).
- 63 L. Wilets, Y. Yariv and R. Chestnut, Nucl. Phys. **A301**, 359 (1978).
- 64 D.J.E. Callaway, L. Wilets and Y. Yariv, Nucl. Phys. **A327**, 250 (1979).
- 65 Y. Kitazoe, K. Yamamoto, and M. Sano, Lett. Nuovo Cimento **32**, 337 (1987).
- 66 J.J. Molitoris, J.B. Hoffer, H. Kruse, and H. Stöcker, Phys. Rev. Lett. **53**, 899 (1984).
- 67 S.M. Kiselev and Y.E. Pokrovski, Yad. Fiz. **38**, 82 (1983) [Sov. J. Nucl. Phys. **38**, 46 (1983)].
- 68 S.M. Kiselev, Phys. Lett. **154B**, 247 (1985).
- 69 V.R. Pandharipande, A. Vicentini and G. Jacucci, see Ref.17,p.1
- 70 A. Vicentini, G. Jacucci, and V.R. Pandharipande, Phys. Rev. **C31**, 1783 (1985).
- 71 R.J. Lenk and V.R. Pandharipande, Phys. Rev. **C34**, 177 (1986).
- 72 V.S. Ramamurthy and S.K.Kataria, Pramana, **11**, 457 (1978).
- 73 A.N. Dixit, V.S. Ramamurthy and Y.R. Waghmare, Pramana **20**, 523 (1983).
- 74 A.N. Dixit, T.K. Mani and Y.R. Waghmare, Proc. Natl. Acad. Sci, India, Sect A **55**, 76 (1985).
- 75 A.N. Dixit, Ph.D. Thesis, Kanpur University (1982).
- 76 T.K. Mani, Ph.D. Thesis, Indian Institute of Technology, Kanpur (1984).
- 77 R.C. Misra, Ph.D. Thesis, Kanpur University (1988).



## CHAPTER 2

## CALCULATIONAL DETAILS OF THE CLASSICAL-MICROSCOPIC APPROACH

## 2.1 INTRODUCTION

In classical-microscopic approach, nucleons are considered as point particles, which interact with each other via two-body forces. Appropriate charges are assigned to the particles. However, nucleons are assumed to be without any spin degree of freedom in the classical-microscopic approach. The motion of each nucleon is governed by the coupled Newton's equations of motion :

$$m \frac{d^2 \vec{r}_i}{dt^2} = -\vec{\nabla}_i \left( \sum_{j \neq i} v_{ij} \right) \quad (2.1)$$

where,  $m$  is the mass of a nucleon which is assumed to have the same value for protons and neutrons; and  $v_{ij}$  is the two-body potential which is chosen to yield reasonable ground-state properties of the nuclei.

The different steps involved in the simulation of a heavy-ion reaction ( $A_1 + A_2$ ) in this approach are

- i) Choosing a suitable two-body interaction potential.
- ii) Construction of the nuclei in their ground-state as initial configurations for the collision calculations.

- iii) Specifying the initial conditions for collisions.
- iv) Finding the trajectories of all the  $A = A_1 + A_2$  nucleons for the above initial conditions; and
- v) Analysis of the trajectory data to calculate reaction properties.

In this chapter we describe in detail the above steps involved in the calculation of fusion cross sections. Computational details are similar to those in the earlier calculations in Ref.1-5.

Procedures for determining the ground-state configurations of the nuclei are described in section 2.2. The necessary features of the two-body potentials in the present approach are discussed in section 2.3. Specification of the initial conditions for collisions and the calculations of the nucleon trajectories are described in section 2.4. Definition of fusion reactions and the details of fusion cross section calculations are given in section 2.5.

## 2.2 CONSTRUCTION OF THE NUCLEI IN THE GROUND-STATES

The individual nuclei used in the collision calculations are obtained by generating a random distribution of all the nucleon positions in a sphere of radius  $R$ , where  $R$  is approximately the radius of the corresponding nucleus. However, this random distribution of nucleon positions is generally very "hot", i.e., energetically very unstable, since, in particular nucleons may be sufficiently close to each other for the short-range repulsion to be very large. Further, such configurations in general may not have density distributions that correspond to nuclear saturation densities. Therefore, to obtain a configuration of the nucleon positions corresponding to an equilibrium ground-state with the correct two-body correlations, this "hot" distribution may be "cooled" by one of the following two methods called the "DYNAMIC" method and the "STATIC" method, respectively.

### 2.2.1 Algorithms

#### (a) "DYNAMIC" Cooling Procedure :

An obvious method of cooling a hot system is to put it in a "heat bath". Particles of the system collide with the "imaginary" particles of the bath and in the process lose their kinetic energy to these particles, while at the same time interact with other particles of the system. Practical steps involved in the calculations are as follows:

- (1) Velocities of all the particles in the system are initially

set equal to zero.

- (2) The "hot" distribution described above is then allowed to dynamically evolve following the classical equations of motion (eq. 2.1) with the chosen two-body potential  $v_{ij}$  between the pairs of particles.
- (3) After a small time interval (usually  $\leq 0.02 \times 10^{-22}$  sec.) the particle velocities are again set equal to zero. This process removes the kinetic energy from the system and cools it; it also provides subsequent initial conditions for further evolution - the initial velocities are zero for the succeeding interval of the evolution.
- (4) At each predetermined time step various gross properties of the assembly of particles such as the total potential energy, and root mean square (r.m.s.) radius are monitored. The total potential energy is given by

$$V = \sum_i \sum_{j>i} v_{ij}(|r_i - r_j|) \quad (2.2)$$

where the sum is taken over all the pairs. The r.m.s radius is given by

$$\langle r^2 \rangle^{1/2} = \left[ \frac{\sum_{i=1}^A (\vec{r}_i - \vec{R}_0)^2}{A} \right]^{1/2} \quad (2.3)$$

where  $A$  is the total number of particles and  $\vec{r}_i$  and  $\vec{R}_0$  are the position vectors of the  $i^{\text{th}}$  particle and the centre of mass, respectively, with respect to the origin.

(5) The steps (1) through (4) are followed till all these macroscopic quantities settle down to their equilibrium values. Total potential energy  $V$  also acquires its minimum value at this stage.

#### (b) "STATIC" method

Another method to find a ground state configuration is to cyclically minimize the total energy of the configuration with respect to small displacements of single coordinates of different nucleons taken one at a time. We call this method "STATIC" because of the static displacements of nucleons. This method is similar to the static solution of the Hartree-Fock (HF) equations by the variational approach; in the present case wave functions being delta functions. Details of the algorithm are as follows:

(1) The initial potential energy ( $U_i^0$ ) of an arbitrarily chosen  $i^{\text{th}}$  particle is calculated

$$U_i^0 = \sum_{j \neq i} v_{ij} (|\vec{r}_i^0 - \vec{r}_j^0|) \quad (2.4)$$

and it is displaced from its initial position ( $\vec{r}_i^0$ ) through a small step of size  $\delta$  along the x-axis, while keeping the positions of all the other particles fixed.

Since all the other particle positions remain fixed, the total potential energy of interaction among these particles, viz ( $V - U_i^0$ ) also remains unchanged.

(2) The potential energy of the  $i^{\text{th}}$  particle in its new location

$(\vec{r}_i^+)$  is calculated

$$U_i^+ = \sum_{j \neq i} v_{ij} (|\vec{r}_i^+ - \vec{r}_j^0|) \quad (2.5)$$

and compared with the potential energy ( $U_i^0$ ) before it was displaced. If  $U_i^+ \leq U_i^0$ , then the above displacement is allowed.

(3) But if  $U_i^+ > U_i^0$ , then the particle is displaced along the x-axis by a step equal to  $2\delta$  in the opposite direction. The potential energy of the  $i^{\text{th}}$  particle in this new location ( $\vec{r}_i^-$ ) is calculated

$$U_i^- = \sum_{j \neq i} v_{ij} (|\vec{r}_i^- - \vec{r}_j^0|) \quad (2.6)$$

and compared with  $U_i^0$ .

(4) The new position is allowed if  $U_i^- \leq U_i^0$ , else the particle is restored to its original position ( $\vec{r}_i^0$ ). Thus the particle is moved along a direction of decreasing potential energy.

(5) The  $i^{\text{th}}$  particle is then moved along the y-axis from the final position of the above procedure and steps 1 through 4 are repeated for the y-coordinate of the  $i^{\text{th}}$  particle; then similarly the steps 1 through 4 are repeated for the z-coordinate of the  $i^{\text{th}}$  particle.

(6) After the x,y, and z-coordinate searches have been made for the  $i^{\text{th}}$  particle the above procedure (steps 1 through 5) is repeated for the next particle.

(7) This process is continued till all the 3A coordinate-searches fail in displacing any particle to a new location. At this stage the macroscopic properties of the cluster, like the total potential energy (eq. 2.2) and the rms radius (eq. 2.3) are

calculated and compared with the previous values.

(8) The step length  $\delta$  is then reduced (usually by half the previous value) and steps 1 through 7 are repeated till the total potential energy converges to a minimum value.

Since the "STATIC" method involves computations and comparisons of potentials only, it is found that when  $A$  is not very large, this method is much faster than the "DYNAMIC" method, which involves calculations of gradients of the potentials and numerical integration of eq. 2.1. A dynamical evolution of the final configuration obtained by the "STATIC" method confirms the dynamical stability of the configuration. Depending upon the final step size used in the "STATIC" method, only a small amount of total kinetic energy is found in the dynamical evolution which can be further removed by the use of the "DYNAMIC" cooling method, requiring only small lengths of time.

It may be pointed out here that while for  $A=2$ , 3, and 4 one can find unique minimum-energy configurations, viz. an equilateral triangle, and a tetrahedron configurations for  $A=3$  and 4 respectively, for  $A \geq 5$  a number of static isomeric configurations may exist. There is no practical method of determining whether a given minimum obtained numerically is in fact absolute or nearly local in character.<sup>6</sup> The only way out here, as is also done in HF calculations of the ground-state, is to take a large number of randomly generated different initial configurations and choose a final equilibrium configuration that has the minimum potential

energy among them.

### 2.2.2 Frozen ground-states :

The minimum potential energy configurations obtained through either of the methods in section 2.2.1 correspond to a frozen system at zero temperature when the particles are arranged approximately in a lattice with zero velocities.

The frequently used technique of thermal excitation of the nuclei to simulate zero-point motion by arbitrarily assigning finite kinetic energies to the nucleons or even using a Fermi distribution of velocities results in an unavoidable premature evaporation of nucleons.<sup>7-12</sup> In Molecular Dynamics calculations,<sup>13</sup> a standard practice to avoid the problem of evaporations is to impose periodic boundary conditions on the system so that a particle leaving the system from one end reappears from the opposite end. However, such boundary conditions cannot be imposed on the nuclei because of their finite size.

While the time scale for such evaporations is large compared to the collision times involved in high-energy collisions, this time scale is clearly small compared to the time scales involved in low-energy collisions. In a low-energy collision process, therefore, premature evaporation of even a few nucleons would amount to extra dissipation of the relative kinetic energy of the colliding residual nuclei which seriously affects fusion cross sections. Therefore, no arbitrary assignment of kinetic energies



to the nucleons is made in the ground state nuclei. Thus the zero-point energy arising from the uncertainty principle and the Pauli exclusion principle is neglected explicitly in the calculations presented in this chapter.

### 2.3 TWO-BODY POTENTIALS

Due to the lack of the Fermi-gas zero-point motion as discussed in section 2.2.2, the internal kinetic energy in the ground state of a nucleus is zero and the binding energy is equal to the total potential energy. Therefore, the use of a free nucleon-nucleon (NN) potential would lead to particle clusters having very large binding energies per nucleon and also very large nucleon densities in their ground-states. Therefore, we use a purely phenomenological form for the NN potential and demand that it reproduce the main gross characteristics of the nuclei, such as the ground state binding energy and the rms radius etc. This is easily done by suitably choosing the constants of the effective NN potential such that the equilibrium macroscopic properties of the particle clusters in their ground state are close to those of the corresponding nuclei.

The usual Coulomb potential between the charged particles (protons) given by

$$V_C(\vec{r}_i - \vec{r}_j) = \frac{1.44}{|\vec{r}_i - \vec{r}_j|} \quad (\text{MeV}) \quad (2.7)$$

is also added to the effective two-body potential. Further, the

differences in the effective strengths of the nuclear interaction between like and unlike particles is taken into account by taking the NN potential between the like particles to be about 20% weaker than that between the unlike particles.<sup>14</sup> Different forms of the NN potentials are considered in the following chapters.

## 2.4 COLLISION CALCULATIONS

### 2.4.1 Initial conditions

We compute all the trajectories in the centre-of-mass reference frame. For practical considerations, it is assumed in all heavy-ion collision simulations that initially (at time  $t = 0$ ) the two colliding clusters are separated by a finite distance ( $R_{CM}$ ), such that the short range strong nuclear interaction between the two nuclei is negligible and the Coulomb interaction is also small, so that the dynamical deformation and the internal excitation of the ions is initially negligible and not yet introduced by the forces. A relatively large centre-of-mass separation ( $R_{CM}$ ) of about 20 fm is found suitable for both the  $^{16}O+^{16}O$  and  $^{40}Ca+^{40}Ca$  reactions considered in this thesis.

For times  $t < 0$ , i.e. before the actual calculations are started, the two ions are considered as point particles with given charges, masses, centre of mass kinetic energy ( $E_{CM}$ ) and impact parameter ( $b$ ), and are assumed to be moving along the classical Coulomb trajectories they would have followed from far in the past ( $t \ll 0$ ). Figure 2.1 depicts the specification of the

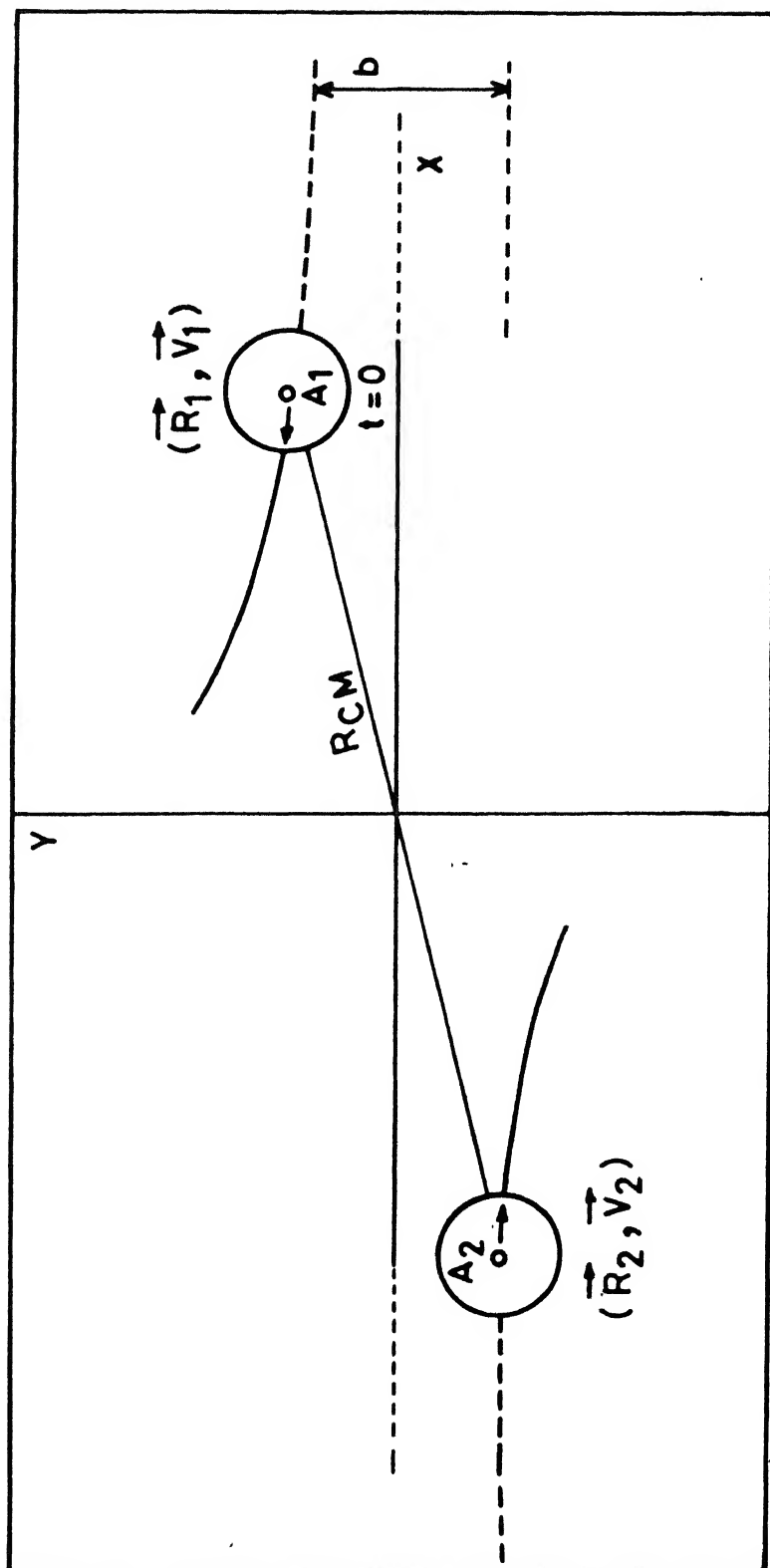


FIGURE 2.1 Schematic diagram depicting specification of the initial conditions for heavy-ion collision calculations in the centre-of-mass frame.

initial conditions at  $t = 0$ . The positions ( $\vec{R}_1, \vec{R}_2$ ) and velocities ( $\vec{V}_1, \vec{V}_2$ ) of the respective centre of masses of the two ions with a given centre of mass separation  $R_{CM}$  at  $t = 0$  are obtained according to the Coulomb trajectory calculations described in the Appendix A.

At  $t=0$  the two particle clusters in their ground state are placed at  $\vec{R}_1$  and  $\vec{R}_2$  respectively and all the nucleons are boosted by uniform velocities corresponding to the respective centre of mass velocities  $\vec{V}_1$  and  $\vec{V}_2$  (see Figure 2.1).

#### 2.4.2 Trajectory Calculations

With the above initial conditions the trajectories of all the nucleons are obtained by numerical integration of A coupled Newton's equations of motion (eq. 2.1), as the two nuclei approach each other.

For numerical solutions of the equations of motion (eq.2.1), each second order differential equation is split into two first-order differential equations and integrated using the Fourth-order Runge-Kutta method.<sup>15</sup> Small integration time steps ( $\delta t$ ) are required to ensure adequate conservation of linear momentum, angular momentum, and the total energy, while at the same time keeping to reasonable computing times. For  $\delta t = 0.02 \times 10^{-22} - 0.04 \times 10^{-22}$  sec. the total energy is conserved to better than 1% and for  $\delta t = 0.1 \times 10^{-22}$  sec. it is about 8%.

## 2.5 FUSION CROSS SECTION CALCULATIONS

### 2.5.1 Definition of Fusion

Since fusion is commonly understood as a reaction that leads to a complete amalgamation of the two nuclei forming a compound system which is equilibrated in all its intrinsic degrees of freedom, it is necessary to understand clearly what is the experimental fusion cross section.

When two heavy-ions "fuse" together, they usually form a compound nucleus or a complex which is similar to it, with some excitation energy and angular momentum. Consequently, it de-excites by emitting light particles and  $\gamma$ -rays leading to a residual nucleus called "evaporation residue", and, if the fission barrier is small or reduced sufficiently by angular momentum, it fissions. In some cases the angular momentum of the fused nucleus is larger than the value for which the fission barrier of the compound-nucleus vanishes. In this case a compound nucleus is not formed but a kind of equilibrated two-centre system is formed which fissions into two fragments. Such a process is called "fast-fission".

The experimental fusion cross section ( $\sigma_{\text{fusion}}$ ) is defined as<sup>16</sup>

$$\sigma_{\text{fusion}} = \sigma_{\text{ER}} + \sigma_{\text{fission}} \quad (2.8)$$

where,  $\sigma_{\text{ER}}$  is the evaporation residue cross section and it

corresponds to nuclei with a mass close to one of the compound nucleus, and  $\sigma_{\text{fission}}$  is the fission or the "fast-fission" cross section, which corresponds to products which have a symmetric mass distribution around a mean value which is about half the compound-nucleus mass.

In eq. 2.8,  $\sigma_{\text{ER}}$  dominates when light compound nuclei are formed in the reactions, whereas  $\sigma_{\text{fission}}$  dominates when heavy compound nuclei are formed. When very heavy target-projectile combinations are involved, with the product  $Z_1 Z_2$  larger than about 2500 to 3000, fusion cross sections go to zero. At projectile energies larger than about 10 MeV/nucleon fusion is incomplete and fast light projectiles can be emitted in the very beginning of the reaction and the two remaining fragments can subsequently fuse together forming a compound nucleus with a mass smaller than the mass of the total initial system.

In theoretical calculations, when the aim is to calculate only the fusion cross section ( $\sigma_{\text{fusion}}$ ) and the decomposition of  $\sigma_{\text{fusion}}$  into the different channels arising from the fused system is not required, it is sufficient to calculate the cross section for the formation of the compound or compound-like fused system and follow its evolution for times longer than the times sufficient for deep-inelastic scattering to occur.

Therefore, we operationally define fusion as a process in which a combined nucleus-nucleus system evolves for a sufficiently long period of time ( $\geq 30 \times 10^{-22}$  sec), without undergoing prompt

fission. This definition is similar to that adopted in TDHF calculations.<sup>17,18</sup> It is also similar to that adopted in the macroscopic calculations where fusion predictions refer to whether the system will be caught behind a barrier in the internuclear potential or not, without any consideration of the question of the subsequent evolution of the long-lived trapped system.<sup>19</sup>

Figures 2.2, 2.3, and 2.4 illustrate the behaviour of a heavy-ion collision at different impact parameters for a given collision energy. The Figure 2.2 shows the C.M. trajectories of one of the  $^{16}\text{O}$  ion in the  $^{16}\text{O}+^{16}\text{O}$  reaction at  $E_{\text{CM}} = 67 \text{ MeV}$  and impact parameters equal to 0, 4, 6, and 8 fm. Figure 2.3 shows the time evolution of the C.M. separation ( $R_{\text{CM}}$ ) and Figure 2.4 shows the energy in the relative motion as a function of time for the same reactions. At  $b = 8 \text{ fm}$  there is negligible loss of the energy from the relative motion and the scattering is elastic with the C.M. trajectories being unbound. At  $b = 6 \text{ fm}$ , a large amount of energy from the relative motion is lost into the internal excitations. But the energy loss is not sufficient to keep the two nuclei together for long time and the two nuclei eventually re-separate leading to deep-inelastic scattering. At  $b = 4 \text{ fm}$ , very large amount of energy from the relative motion is dissipated and the two nuclei fuse together. In this case the nuclei stick to each other and revolve around a common axis,  $R_{\text{CM}}$  is bound with small oscillations. For a head-on collision ( $b = 0 \text{ fm}$ ), almost entire energy in the relative motion is lost, the two nuclei stop each other and fuse.

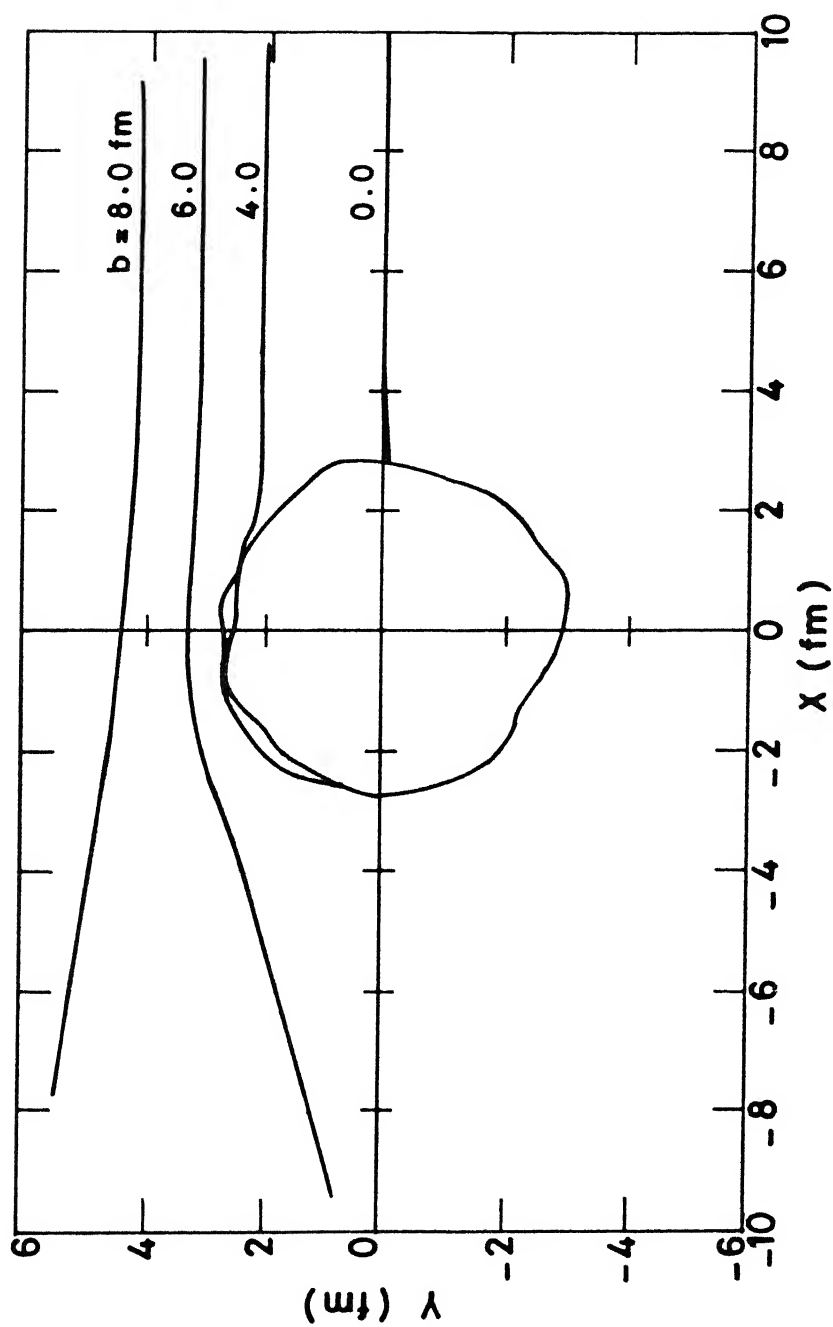


FIGURE 2.2 C.M. trajectories of one of the  $^{16}\text{O}$  nuclei in the  $^{16}\text{O}+^{16}\text{O}$  reaction (with the potential P3 referred in Chapter 4) at  $E_{\text{CM}} = 66.8$  MeV and different impact parameters.



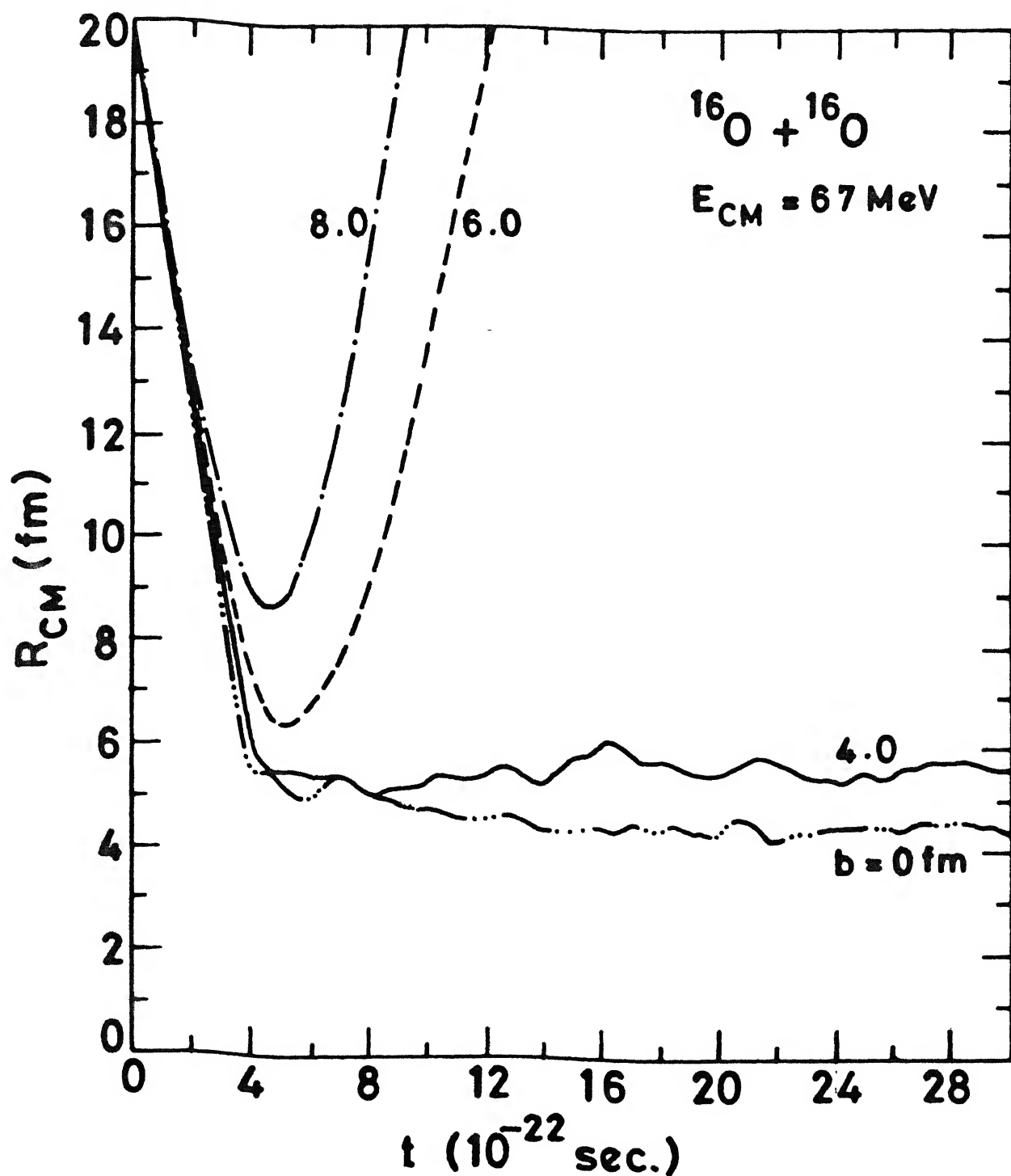


FIGURE 2.3

Relative distance ( $R_{CM}$ ) between the centres-of-mass of two ions as a function of time for the  $^{16}\text{O} + ^{16}\text{O}$  reaction at  $E_{CM} = 66.8 \text{ MeV}$  and different impact parameters.

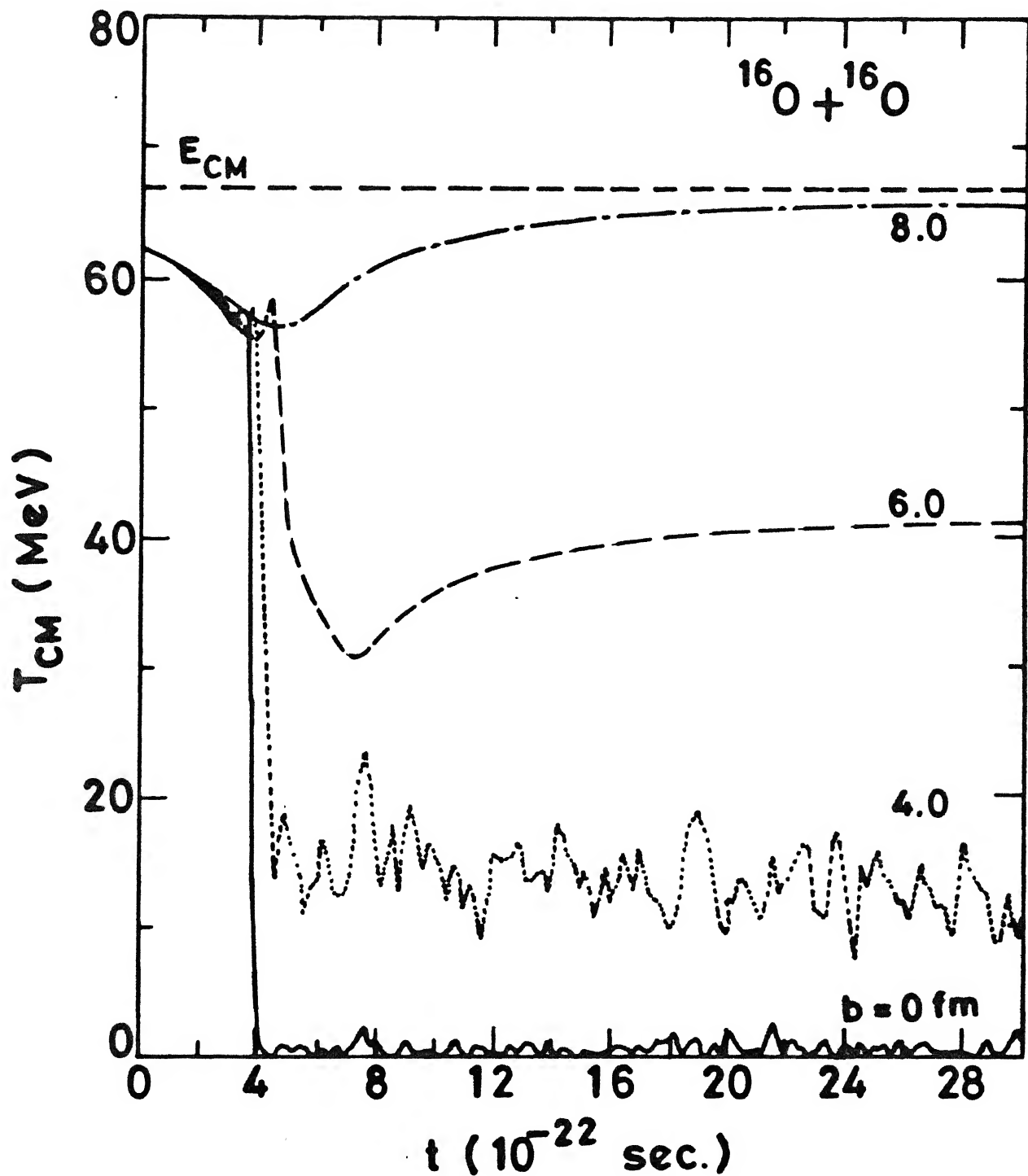


FIGURE 2.4

Time evolution of the kinetic energy in the relative motion ( $T_{CM}$ ) for the  $^{16}\text{O} + ^{16}\text{O}$  reaction at  $E_{CM} = 66.8$  MeV and different impact parameters.

### 2.5.2 Expressions for fusion cross sections

Heavy-ion fusion cross sections are given by<sup>20</sup>

$$\sigma_{\text{fusion}} = \pi \lambda^2 \sum_{\ell=0}^{\infty} (2\ell+1) T_{\ell} \quad (2.9)$$

where  $T_{\ell}$  is the transmission coefficient for the  $\ell$ th partial wave and  $\lambda$  is the reduced wave number. For simplicity we calculate fusion cross sections in the Sharp-Cutoff model. In this approximation it is assumed that for a given  $E_{\text{CM}}$  there is a critical value of the angular momentum ( $\ell_{\text{cr}}$ ), above which no fusion takes place, viz.,

$$T_{\ell} = \begin{cases} 1 & \text{for } \ell \leq \ell_{\text{cr}} \\ 0 & \text{for } \ell > \ell_{\text{cr}} \end{cases}$$

where  $\ell_{\text{cr}}$  is the highest partial wave to fuse. Thus, for a given  $E_{\text{CM}}$  fusion takes place for angular momenta between zero and  $\ell_{\text{cr}}$  only and the fusion cross is given by

$$\sigma_{\text{fusion}} = \pi \lambda^2 \sum_{\ell=0}^{\ell_{\text{cr}}} (2\ell + 1)$$

Summing the series, we get

$$\begin{aligned} \sigma_{\text{fusion}} &= \pi \lambda^2 (\ell_{\text{cr}} + 1)^2 \\ &\approx \pi \lambda^2 \ell_{\text{cr}} (\ell_{\text{cr}} + 1) \end{aligned} \quad (2.10)$$

Therefore, an expression for classical fusion cross sections is given by

$$\sigma_{\text{fusion}} = \pi b_{\text{cr}}^2 \quad (2.11)$$

where  $b_{\text{cr}}$  is the critical impact parameter given by

$$b_{\text{cr}} = \lambda \sqrt{\ell_{\text{cr}}(\ell_{\text{cr}}+1)} \quad (2.12)$$

### 2.5.3 Initial relative random orientations and Statistical averaging

It is not possible to find a spherically symmetric particle distribution for a cluster with a finite number of particles. Figure 2.5 shows projections of nucleon positions in a randomly oriented ground state clusters of  $^{16}\text{O}$  and  $^{40}\text{Ca}$ . It is clear from the Figure 2.5 that the distribution of the nucleons in the cluster is not spherically symmetric. This fact can also be noted by finding the principal moments of inertia<sup>21</sup> of the cluster. For the  $^{16}\text{O}$  cluster shown in the Figure 2.5, principal moments of inertia are in the ratio 1.00 : 1.35 : 1.49. Therefore, the cluster is not completely spherically symmetric. Therefore, it becomes necessary to find an average of  $b_{\text{cr}}$  in eq. 2.11 over different trajectory calculations in which initially (at  $t=0$ ) the two clusters placed at  $\vec{R}_1$  and  $\vec{R}_2$  respectively, are randomly oriented with respect to each other. The changes in the initial relative orientations do not alter the relative positions of the nucleons within the same clusters and the initial ground-state configurations remain invariant. Generation of pseudo-random numbers and a rigid rotation transformation matrix<sup>21</sup> are used to give random orientations to

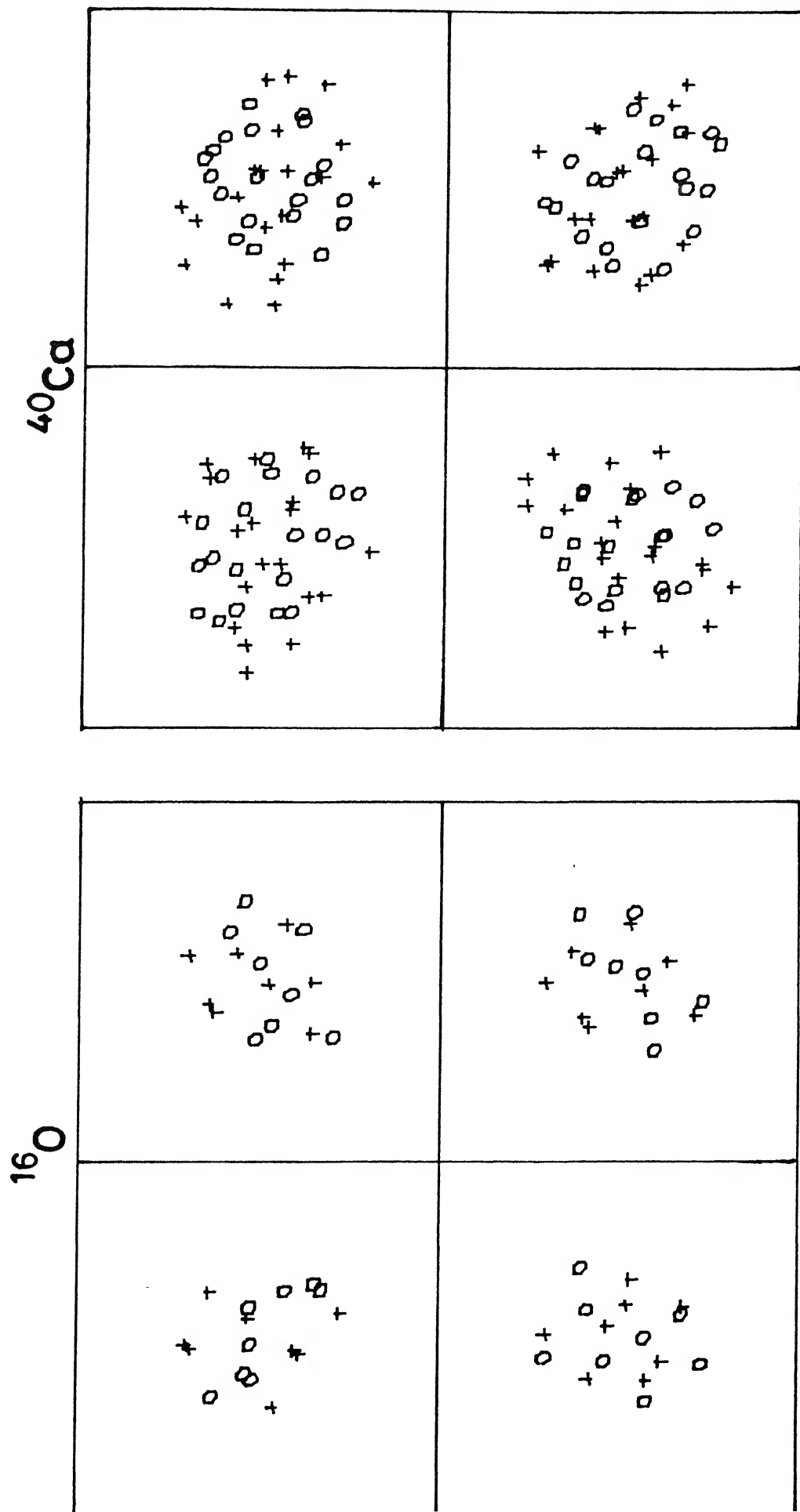


FIGURE 2.5 The nucleon coordinate projection of  $^{16}\text{O}$  and  $^{40}\text{Ca}$  nuclei in various orientations (with the Potential P3 referred in Chapter 4).

each clusters.

For  $^{16}\text{O}+^{16}\text{O}$  system ( $A_1+A_2 = 32$ ),  $b_{\text{cr}}$  in eq. 2.11 is averaged over 12 initial random orientations. Since  $^{40}\text{Ca}+^{40}\text{Ca}$  system has ( $A_1+A_2 = 80$ ) more number of particles, effectively there is considerable averaging even for each orientation. Therefore, it requires proportionately less number of orientations for averaging  $b_{\text{cr}}$ . Therefore, only six orientations are considered in fusion cross section calculations for the  $^{40}\text{Ca}+^{40}\text{Ca}$  reaction in Chapter 4. Calculations with twice as many orientations for both the reactions result in less than 2% differences in the respective average fusion cross sections. Each critical impact parameter ( $b_{\text{cr}}$ ) is determined to an accuracy of about 0.2 fm.

## REFERENCES

- 1 V.S. Ramamurthy and S.K.Kataria, *Pramana*, **11**, 457 (1978).
- 2 A.N. Dixit, V.S. Ramamurthy and Y.R. Waghmare, *Pramana* **20**, 523 (1983).
- 3 A.N. Dixit, T.K. Mani and Y.R. Waghmare, *Proc. Natl. Acad. Sci, India, Sect A* **55**, 76 (1985).
- 4 A.N. Dixit, Ph.D. Thesis, Kanpur University (1982).
- 5 T.K. Mani, Ph.D. Thesis, Indian Institute of Technology, Kanpur (1984).
- 6 M.R. Hoare and P. Pal, *Adv. Phys.* **20**, 161 (1971).
- 7 A.R. Bodmer and C.N. Panos, *Phys. Rev.* **C15**, 1342 (1977); *Nucl. Phys.* **A356**, 517 (1981).
- 8 A.R. Bodmer, C.N. Panos and A.D. MacKellar, *Phys. Rev.* **C22**, 1025 (1980).
- 9 Y. Kitazoe, K. Yamamoto, and M. Sano, *Lett. Nuovo Cimento* **32**, 337 (1987).
- 10 J.J. Molitoris, J.B. Hoffer, H. Kruse, and H. Stöcker, *Phys. Rev. Lett.* **53**, 899 (1984).
- 11 S.M. Kiselev and Y.E. Pokrovski, *Yad. Fiz.* **38**, 82 (1983) [*Sov. J. Nucl. Phys.* **38**, 46 (1983)].
- 12 S.M. Kiselev, *Phys. Lett.* **154B**, 247 (1985).
- 13 W.G. Hoover, *Ann. Rev. Phys. Chem.* **34**, 103 (1983); and references therein.
- 14 W.D. Myers and W.J. Swiatecki, *Ann. Phys. (N.Y.)* **55**, 395 (1969).
- 15 J.B. Scarborough, *Numerical Mathematical Analysis*, sixth edition (The Johns Hopkins Press, Baltimore, 1966; and Oxford IBH Pub. Co., Delhi), ch. 13, Art. 116.
- 16 C. Ngô, *IL Nuovo Cimento*, **81A**, 47 (1984).
- 17 P. Bonche, B. Grammaticos and S. Koonin, *Phys. Rev.* **C17**, 1700 (1978)
- 18 J.W. Negele, *Rev. Mod. Phys.* **54**, 914 (1982); and references therein.
- 19 J. R. Birkelund, L.E. Tubbs, J.R. Huizenga, J.N. De and D.Sperber, *Phys. Rep.* **56**, 107 (1979).

- 20 U. Mosel, *Treatise on Heavy-ion science*, edited by D.A. Bromley (Plenum, New York 1985), Vol.2, p.3; and references therein.
- 21 H. Goldstein, *Classical Mechanics* (Addison Wesley, 1950).



## CHAPTER 3

CLASSICAL-MICROSCOPIC CALCULATION OF FUSION CROSS SECTIONS FOR THE  $^{16}\text{O}+^{16}\text{O}$  REACTION WITH THE LENNARD-JONES FORM OF NN POTENTIAL

## 3.1 INTRODUCTION

In an application of the classical-microscopic approach to heavy-ion collision calculations at low projectile energies, Ramamurthy and Kataria<sup>1</sup> chose a Lennard-Jones form of the two-body potential for the interaction between the nucleons and studied  $^{16}\text{O}+^{16}\text{O}$  reaction at  $E_{\text{lab}} = 128$  MeV. Their calculations showed that most of the essential features of heavy-ion collisions at low energies, such as fusion, deep-inelastic scattering and particle-exchanges are adequately brought out in the classical-microscopic approach.

Following the calculations of Ramamurthy and Kataria, Dixit et al<sup>2-4</sup> also used a Lennard-Jones form for the NN potential given by

$$v(r_{ij}) = 4\epsilon \left[ (\sigma/r_{ij})^{12} - (\sigma/r_{ij})^6 \right] \quad (3.1)$$

and calculated fusion cross sections for  $^{16}\text{O}+^{16}\text{O}$  (Ref.2); and  $^{16}\text{O}+^{40}\text{Ca}$  and  $^{40}\text{Ca}+^{40}\text{Ca}$  (Ref.3) reactions at various energies. In a similar approach Mani calculated fusion cross sections for  $^{16}\text{O}+^{16}\text{O}$  and  $^{12}\text{C}+^{14}\text{N}$  reactions, albeit with a different form of

the NN interaction potential (Ref.5). These calculations qualitatively reproduce the shapes of the respective fusion excitation functions for all the above mentioned reactions and give good agreement on the higher energy side of the respective fusion excitation functions. However, it is observed that the calculated fusion cross sections for all the above reactions are systematically overestimated on the lower energy side of the fusion excitation functions, just above the respective Coulomb barriers.

These deviations from the experimental data at lower energies have been attributed to the possible breakdown of the classical approximations.<sup>2,3</sup> On the other hand, even a simple classical one-dimensional static-potential model reproduces fusion cross sections, precisely in this energy region -though such models fail at higher energies due to the increasing importance of the dynamical effects which are neglected. Therefore, it is necessary to examine the real cause of the discrepancy between the experiments and the earlier classical-microscopic calculations.

In this chapter we re-examine Dixit et al's calculations taking the  $^{16}\text{O}+^{16}\text{O}$  reaction as an example and try to explain the cause of the discrepancy in classical fusion cross sections at low energies. The use of Lennard-Jones potential as an NN interaction in heavy-ion collision calculations is also critically examined.

### 3.2 IMPORTANCE OF THE CORRECT INITIAL CONDITIONS

It is noticed that in all the above mentioned calculations, initially at time  $t=0$  for collisions the centres of mass of the colliding nuclei, placed at a relatively large separation of about 20 fm are, however, assumed to be moving along unperturbed straight line trajectories ( see Figure 3 of Ref.2 ) instead of the Coulomb trajectories followed from far in the past as described in section 2.4.1 and Appendix A. Initial velocities at  $t=0$  correspond to a given initial collision energy ( $E_{CM}$ ) and a given impact parameter ( $b$ ). Thus, in all the above calculations the important effect of the repulsion due to the Coulomb interaction between the two ions is neglected for  $t < 0$  at large separations.

The Coulomb potential between two ions of charges  $Z_1$  and  $Z_2$ , separated by a distance  $R$  is given by

$$V_C(R) = \frac{1.44 Z_1 Z_2}{R} \quad (\text{MeV}) \quad (3.2)$$

The Coulomb potential between two  $^{16}\text{O}$  ions separated by 20 fm is about 4.6 MeV. This Coulomb potential, though small compared to the highest energy ( $E_{CM} = 67$  MeV) for which Dixit et al<sup>2</sup> calculated fusion cross sections for the  $^{16}\text{O} + ^{16}\text{O}$  reaction, can not be neglected at lower energies ( e.g. at  $E_{CM} = 16.7$  MeV).

Figure 3.1 shows the centre-of-mass (C.M.) trajectories of one of the  $^{16}\text{O}$  ions in the  $^{16}\text{O}+^{16}\text{O}$  reaction at  $E_{\text{CM}}=16.7$  MeV and  $b=5.6$  fm, with

(A) the correct initial conditions as described in section 2.4.1; and

(A') with the neglect of the Coulomb repulsion between the two ions for  $t < 0$ , as in Ref.2.

The two cases, marked by A and A' respectively, show remarkable differences in the C.M. trajectories. For a given energy and an impact parameter, while the correct specification of the initial conditions lead to scattering of the ions (A), the neglect of the Coulomb repulsion in the specification of the initial conditions leads to a case of fusion (A'). Thus, it is due to the neglect of the Coulomb repulsion for  $t < 0$  that, in Ref.2, the trajectories with even higher impact parameters could lead to the fusion of the colliding nuclei for a given collision energy, giving rise to the higher values of the critical impact parameters ( $b_{\text{cr}}$ ). Since fusion cross sections are given by eq. 2.11, the higher values of  $b_{\text{cr}}$  result in very high values of the fusion cross sections for the  $^{16}\text{O}+^{16}\text{O}$  reaction at low energies. This effect is even more pronounced in the reactions that involve heavier ions, as in Ref.3,4.

Therefore, to illustrate the above effect, we re-calculate fusion cross sections for the  $^{16}\text{O}+^{16}\text{O}$  reaction, choosing the same form of the two-body Lennard-Jones potential for the interaction between the nucleons and the same values of the parameters  $\epsilon$  and  $\sigma$

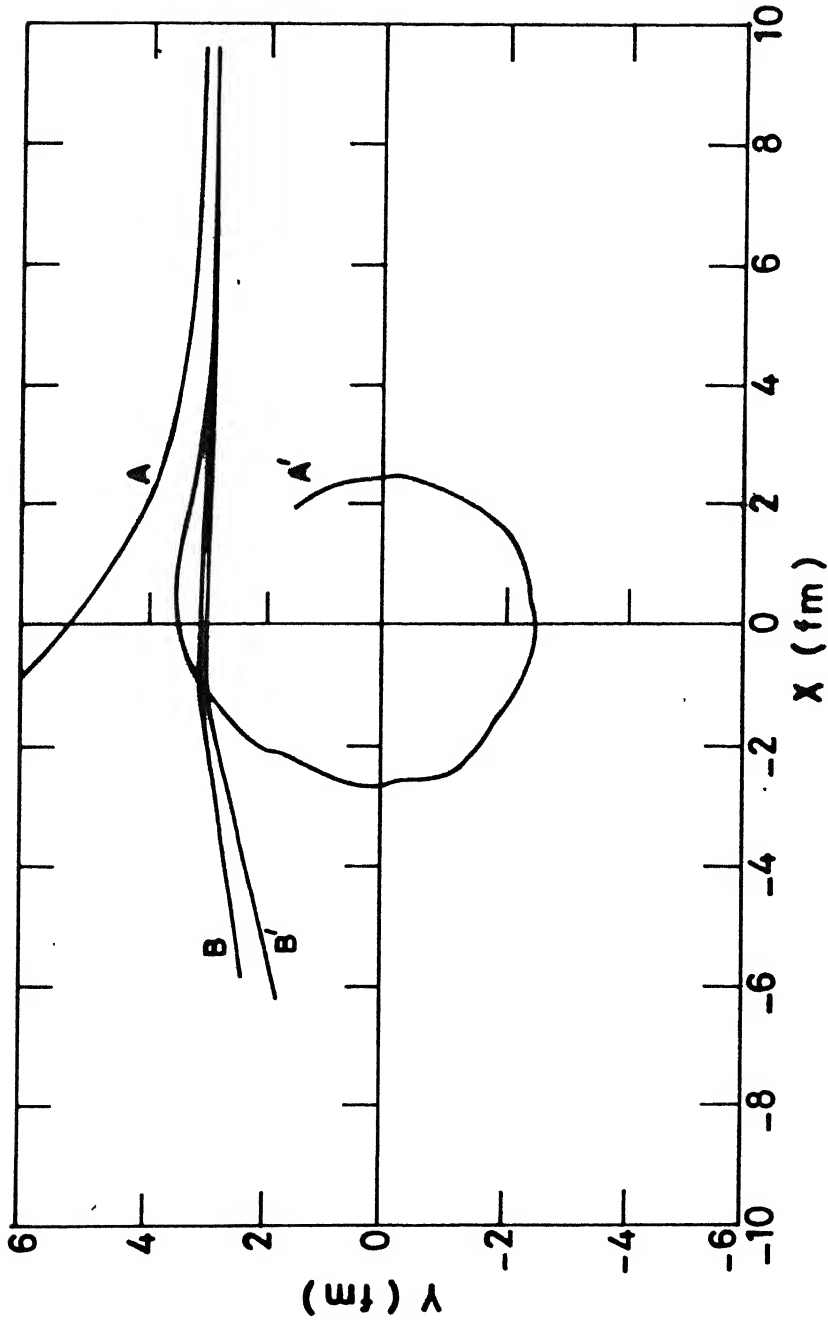


FIGURE 3.1 Centre-of-mass trajectories of one of the  $^{16}\text{O}$  ions in the  $^{16}\text{O}+^{16}\text{O}$  reaction with the initially correct Coulomb trajectories at (A)  $E_{\text{CM}} = 16.7 \text{ MeV}$ ; and (B)  $E_{\text{CM}} = 66.8 \text{ MeV}$ . (A') and (B') are the initially straight line trajectories for the two energies respectively.

taken from Ref.2. The calculated fusion cross sections for  $E_{CM}=16.7, 37.6, \text{ and } 66.8 \text{ MeV}$  are shown in Figure 3.2 for both the cases. Fusion cross sections calculated with the correct initial conditions as described in section 2.4.1 are denoted by L1 in the Figure 3.2 and the fusion cross sections calculated by neglecting the Coulomb interaction for  $t < 0$ , as in Ref.2, are shown denoted by L1'. It is clear from Figure 3.2 that the fusion cross section with the initially correct classical Coulomb trajectories (L1) is considerably reduced at a lower energy ( $E_{CM}=16.7 \text{ MeV}$ ) compared to that with the initially undeflected straight line trajectories (L1').

At higher energies the effect of the Coulomb repulsion at large ion-ion separations is considerably reduced and, as shown in the Figure 3.1, the ions initially move along nearly straight line trajectories for  $E_{CM}=66.8 \text{ MeV}$  in both the cases (denoted by B and B'). Further, the difference between the trajectories in the two cases at this energy is also very small. Therefore, the assumption of an initially straight line trajectory in the earlier calculations is good only at higher incident energies and fusion cross sections in both the cases (L1 and L1') do not show any appreciable differences at  $E_{CM}=66.8 \text{ MeV}$  (see Figure 3.2).

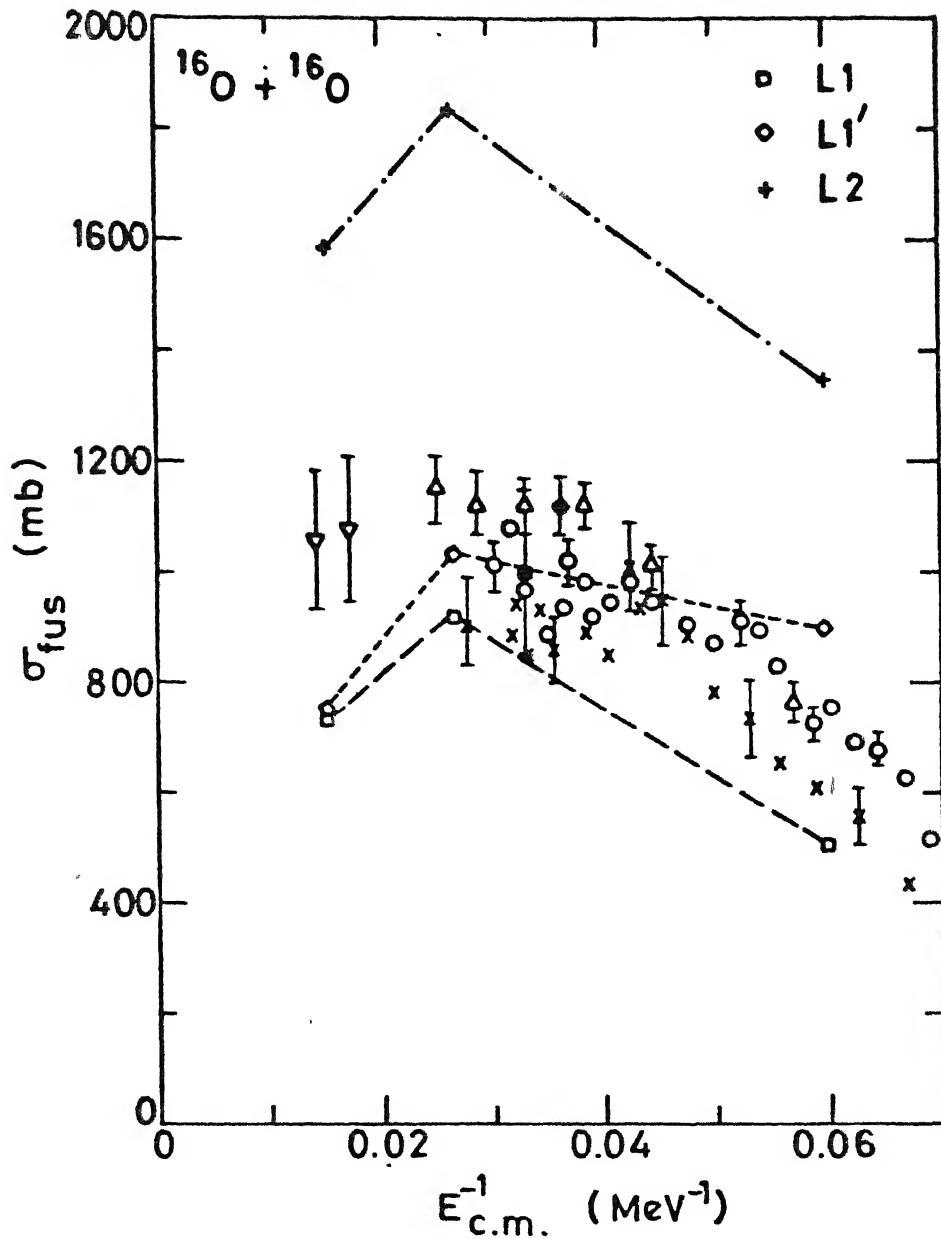


FIGURE 3.2

Calculated fusion cross sections for the  $^{16}\text{O}+^{16}\text{O}$  reaction:  
 $\square$  - potential L1 and initially Coulomb trajectories;  $\diamond$  - potential L1 and initially straight line trajectories (L1');  $+$  - potential L2, which reproduces ground-state properties of  $^{16}\text{O}$ . Calculated points with different potentials and initial conditions are connected to guide the eye. Experimental data are shown by  $\circ$  (Ref. 6),  $\times$  (Ref.7),  $\Delta$  (Ref.8),  $\blacklozenge$  (Ref.9),  $\blacksquare$  (Ref.10), and  $\nabla$  (Ref.11).

### 3.3 DEPENDENCE OF FUSION CROSS SECTIONS ON THE GROUND-STATE NUCLEAR PROPERTIES

The parameters  $\epsilon$  and  $\sigma$  of the Lennard-Jones potential (eq. 3.1) from Ref.2 are also given table 3.1 under the set called L1, along with the calculated binding energy and the rms radius of  $^{16}\text{O}$ . The rms radius of  $^{16}\text{O}$  obtained in the present calculations is slightly smaller than the value obtained in the Ref.2 for the same set of parameters (see table 3.1). Therefore, due to a slightly smaller size of the ions in the present calculations fusion cross sections with the initially straight line trajectories (L1') are also slightly smaller compared to the corresponding fusion cross sections calculated by Dixit et al in Ref.2.

The rms radius obtained in the present calculation, as well as in Ref.2 are, however, about 20% smaller compared to the experimental rms radius of  $^{16}\text{O}$ . Consequently, we find that fusion cross sections for  $^{16}\text{O}+^{16}\text{O}$  reaction with the potential L1 and with the correct initial conditions are also underestimated compared to the experimental data.<sup>6-11</sup> Thus, fusion cross sections depend on the ground-state properties of the nuclei (see also Ref.12 ). Therefore, we readjust the parameters  $\epsilon$  and  $\sigma$  such that the experimental binding energy and the rms radius of  $^{16}\text{O}$  are reproduced correctly. The new set of parameters (called L2) are given in Table 3.1. The potential L2 is plotted in Figure 3.3 and compared with the potential L1. The corresponding fusion cross sections with the potential L2 are shown in the Figure 3.2



TABLE 3.1

Parameters of the Lennard-Jones potential (eq. 3.1) and the calculated binding energies and rms Radii of  $^{16}\text{O}$  for different calculations.

	Dixit et al <sup>2</sup>	L1	L2	Experiment
$\epsilon$ (MeV)	2.20	2.20	2.72	
$\sigma$ (fm)	1.80	1.80	2.36	
Binding Energy (MeV)	-90.0	-96.8	-127.6	-127.6
rms radius (fm)	2.24	2.12	2.73	2.73

106281

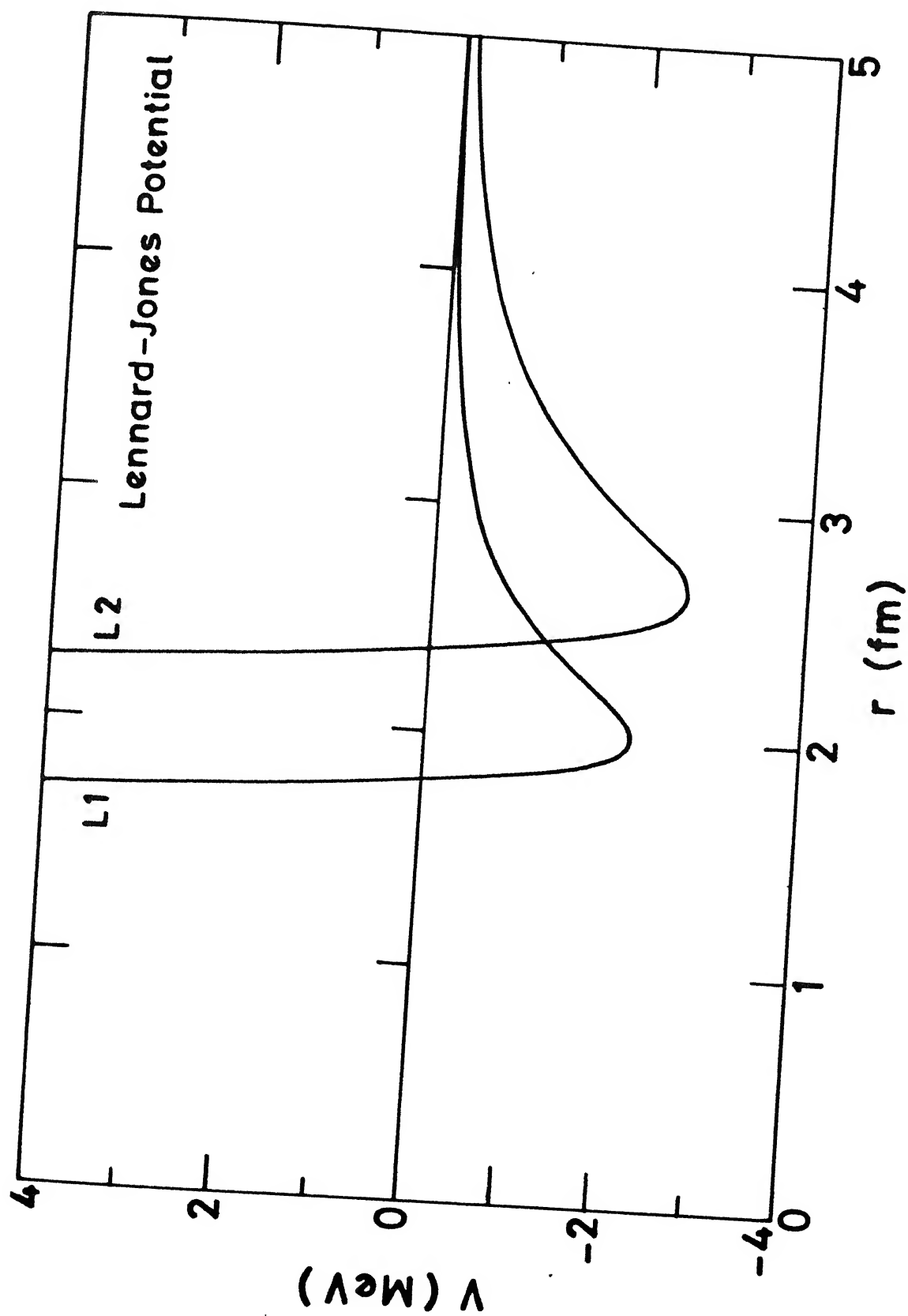


FIGURE 3.3 Plots of Lennard-Jones potential for the parameter sets L1 and L2 given in Table 3.1.

(denoted by L2). It is seen from the Figure 3.2 that at all the energies considered, fusion cross sections with this potential (L2) have very large values compared to those with the potential L1, as well as to the experimental data.<sup>6-11</sup>

### 3.4 SUMMARY AND DISCUSSIONS

To recapitulate, Dixit et al obtained an overestimation of fusion cross sections for the  $^{16}\text{O}+^{16}\text{O}$  reaction at lower energies and speculated that this may be due to the possible breakdown of the classical approximations at low energies. It is however, shown above that this overestimation of fusion cross sections is rather due to the neglect of the Coulomb repulsion in the initial stages and incorrect specification of the initial conditions. With the correct initial conditions, on the contrary, we get an underestimation of fusion cross sections when the same set of parameters for the Lennard-Jones potential are used. This underestimation is due to the smaller size of the  $^{16}\text{O}$  nucleus generated by this set of parameters (L1). Adjustment of the potential parameters to get the correct ground-state properties, however, results in an even larger overestimation of the fusion cross sections; notably at all collision energies.

Calculated fusion cross sections with the potential L2 are almost uniformly overestimated over a wide range of collision energies (Figure 3.2). Since it is expected that the classical approximations become increasingly good as the projectile energy

is increased, it is difficult to make any definite conclusion about the extent of the invalidity of the classical approximations only on the basis of the above disagreement of the calculated fusion cross sections with the experiments. On the other hand, it is also to be noted that the Lennard-Jones potential (eq. 3.1) has a very long-range attractive tail which goes like  $4 \epsilon r_{ij}^{-6}$  at large  $r_{ij}$ , falling-off much slowly compared to a more conventional gaussian or an exponential form of attractive tail used in Nuclear Physics studies (Ref. 13). This long-range attractive tail of the Lennard-Jones potential tends to increase the attractive part of the ion-ion potential and the radius of the fusion barrier ( $R_B$ ), and decreases its height ( $V_B$ ). Thus, according to the simple one-dimensional potential model (see Ref.14 and chapter 4, eq. 4.2), an increase in  $R_B$  and a decrease in  $V_B$  lead to an increase in the fusion cross section for a given collision energy. Therefore, the above overestimation of the fusion cross sections for a Lennard-Jones potential (L2), which correctly reproduces ground-state properties of a nucleus, is mainly due to its long-range attractive tail. This indicates that fusion cross sections are not only sensitive to the ground-state properties of the nuclei alone, but also to the details of the two-body NN potentials; in particular to the range of the NN interaction.

A systematic study of the sensitivity of fusion cross sections on the long-range part of the interaction would require a two-body potential whose range can be adjusted without significantly affecting the ground-state properties of the nuclei.

Since the Lennard-Jones potential has only two parameters ( $\epsilon$  and  $\sigma$ ), which essentially determine the position ( $r_{\min}$ ) and the depth ( $V_{\min}$ ) of the minimum of the NN potential, it does not allow one to make such a systematic study. Hence, the Lennard-Jones potential which is extensively used in the molecular-dynamic simulations of classical fluids, does not seem to be a suitable two-body potential for use in the study of heavy-ion reactions in the present approach. A systematic study of the sensitivity of fusion cross sections on the long-range attractive tail of an NN potential is presented in chapter 4, choosing a different form of the two-body potential.

## REFERENCES

- 1 V.S. Ramamurthy and S.K.Kataria, *Pramana*, **11**, 457 (1978).
- 2 A.N. Dixit, V.S. Ramamurthy and Y.R. Waghmare, *Pramana* **20**, 523 (1983).
- 3 A.N. Dixit, T.K. Mani and Y.R. Waghmare, *Proc. Natl. Acad. Sci, India, Sect A* **55**, 76 (1985).
- 4 A.N. Dixit, Ph.D. Thesis, Kanpur University (1982).
- 5 T.K. Mani, Ph.D. Thesis, Indian Institute of Technology, Kanpur (1984).
- 6 I. Tserruya, Y. Eisen, D. Pelte, A. Gavron, H. Oeschler, D. Berndt and H.L. Harney, *Phys. Rev.* **C18**, 1688 (1978).
- 7 D.G. Kovar, D.F. Greesman, T.H. Braid, Y. Eisen, W. Henning, T.R. Ophel, M. Paul, K.E. Rehm, S.J. Sanders, P. Sperr, J.P. Schiffer, S.L. Tabor, S. Vigdor, B. Zeidman and F.W. Prosser, Jr., *Phys. Rev. C* **20**, 1305 (1979).
- 8 B. Fernandez, C. Gaarde, J.S. Larsen, S. Pontoppidan, and F. Videbaek, *Nucl. Phys.* **A306**, 259 (1978).
- 9 A.J. Cole, N. Longequeue, J. Menet, J.J. Lucas, R. Ost and J.B. Viano, *Nucl. Phys.* **A341**, 284 (1980).
- 10 A. Weidinger, F. Busch, G. Gaul, W. Trautmann and W. Zipper, *Nucl. Phys.* **A263**, 511 (1976).
- 11 F. Saint-Laurent, M. Conjeaud, S. Harar, J.M. Loiseaux, J. Menet and J.B. Viano, *Nucl. Phys.* **A327**, 517 (1979).
- 12 J. R. Birkelund, L.E. Tubbs, J.R. Huizenga, J.N. De and D.Sperber, *Phys. Rep.* **56**, 107 (1979).
- 13 P. Ring and P. Schuck, *The Nuclear Many-Body Problem* (Springer-Verlag, Berlin, 1980), chapter 4.
- 14 U. Mosel, *Treatise on Heavy-ion science*, edited by D.A. Bromley (Plenum, New York, 1985), Vol.2, p.3; and references therein.

## CHAPTER 4

CLASSICAL-MICROSCOPIC CALCULATIONS FOR  $^{16}\text{O}+^{16}\text{O}$  AND  $^{40}\text{Ca}+^{40}\text{Ca}$   
 REACTIONS WITH A SOFT-CORE GAUSSIAN FORM OF THE NN POTENTIAL

## 4.1 INTRODUCTION

The central input to the classical-microscopic approach which is described in chapter 2, is a two-body nucleon-nucleon (NN) potential. It is, therefore, desired to understand clearly how heavy-ion fusion cross sections depend on this input. While, this approach allows for a systematic study of the repulsive core of the effective NN potential in high-energy heavy-ion collisions,<sup>1,2</sup> a systematic study of the fusion of heavy ions at low energies may provide information about its long range attractive tail.

In chapter 3, it is shown that the use of the Lennard-Jones potential as an NN potential results in overestimation of fusion cross sections due to its very long-range attractive tail. The Lennard-Jones potential has only two parameters which essentially determine the position and the depth of the minimum of the potential and thus determine the binding energy and the rms radius of a nucleus. Lack of an adjustable range in the Lennard-Jones potential does not permit a systematic study of fusion cross sections on the detailed nature of an NN potential. Therefore,

for this systematic study a more sophisticated form of the NN potential is required, keeping the number of essential parameters to a minimum.

In nuclear structure studies it has been common to choose an exponential or a Yukawa or a gaussian form for the attractive tail of the NN potential and a suitable form factor for the hard or soft repulsive core.<sup>3</sup> For the present study we choose a soft-core gaussian potential given by<sup>4</sup>

$$v_{ij}(r_{ij}) = -V_0 (1 - C/r_{ij}) \exp (-r_{ij}^2/r_0^2) \quad (4.1)$$

where  $V_0$ ,  $C$ , and  $r_0$  are the depth parameter, repulsive core radius and range parameter respectively. For a given value of  $r_0$ , the parameters  $V_0$  and  $C$  are determined by the nuclear ground state properties. The range of the NN potential can be varied by suitably adjusting the range parameter  $r_0$ . Keeping in mind the large overestimation of fusion cross sections with a long-range Lennard-Jones potential, a gaussian form of the tail is more appropriate as it goes to zero much faster than the Lennard-Jones, an exponential or the Yukawa forms of the potential. The shape of the repulsive core is not expected to play any significant role in the determination of the fusion excitation functions because of the relatively low projectile energies involved in the fusion of heavy-ions.<sup>5</sup>



A systematic study of the sensitivity of fusion cross sections on the range of the NN potential given by eq. 4.1 is carried out in section 4.2.1. For this systematic study, we calculate fusion cross sections for the  $^{16}\text{O}+^{16}\text{O}$  reaction with the different values of the range parameter  $r_0$ . Fusion cross sections for a heavier system,  $^{40}\text{Ca}+^{40}\text{Ca}$ , are also calculated and compared with the experiments in section 4.2.2. Several features of the results and the effective NN potentials are discussed in section 4.2.3.

In this chapter we also study some behaviour of heavy-ion collisions at higher incident energies. In particular, in section 4.3.1 we examine the question of the existence of the  $\ell$ -window for fusion, which is predicted by the TDHF calculations above a certain threshold energy. In section 4.3.2 we present a  $^{40}\text{Ca}+^{40}\text{Ca}$  collision calculation at  $E_{\text{CM}} = 418$  MeV/nucleon which shows the "sideward-flow" or the "side-splash" of the nuclear matter which has been observed experimentally. Finally, the conclusions are given in section 4.4.

## 4.2 FUSION CROSS SECTION CALCULATIONS

### 4.2.1 The $^{16}\text{O}+^{16}\text{O}$ Reaction.

#### Systematic Study Of The Dependence Of Fusion Cross Sections On The Range Of The NN Potential:

To study the sensitivity of fusion cross sections on the range of the NN potential (eq. 4.1) we calculate fusion cross sections for the  $^{16}\text{O}+^{16}\text{O}$  reaction with different values of the range parameter  $r_0$ . Three different values of  $r_0$  (1.8, 1.4 and 1.2 fm) are chosen. Parameters  $V_0$  and  $C$  are adjusted for each value of  $r_0$ , such that the ground-state configurations in each case reproduce the experimental binding energy and rms radius for  $^{16}\text{O}$  nucleus. For  $r_0 = 1.8, 1.4$  and  $1.2$  fm, the set of parameters are called potentials P1, P2 and P3, respectively, and are given in Table 4.1 alongwith the calculated ground-state properties for  $^{16}\text{O}$ .

The ground-state configurations for  $^{16}\text{O}$  obtained by the methods described in chapter 2 and potentials P1, P2, and P3 all have the same value of the binding energy and the rms radius. Ratios of the principal moments of inertia for these configurations are given in Table 4.2. The nearly same ratios of the principal moments of inertia indicate that these configurations have similar mass distributions and shapes. Figure 4.1 shows the pair-distribution functions  $n(r_{ij})$ ,<sup>6</sup> i.e. the number

TABLE 4.1

Parameters of the effective NN Potential (eq. 4.1) and the calculated binding energy and rms radius of  $^{16}_0$  in the ground-states with different potentials.

	P1	P2	P3	Experiment
$r_0$ (fm)	1.8	1.4	1.2	
$V_0$ (MeV)	142.0	730.0	3360.0	
$C$ (fm)	2.19	2.28	2.35	
Binding energy (MeV)	-127.6	-127.6	-127.6	-127.6
rms radius (fm)	2.73	2.73	2.73	2.73

TABLE 4.2

Ratios of the Principal Moments of Inertia in the ground-states of  $^{16}\text{O}$  with different potentials.

Potential	$I_1$	:	$I_2$	:	$I_3$
P1	1.00	:	1.34	:	1.44
P2	1.00	:	1.35	:	1.49
P3	1.00	:	1.35	:	1.49

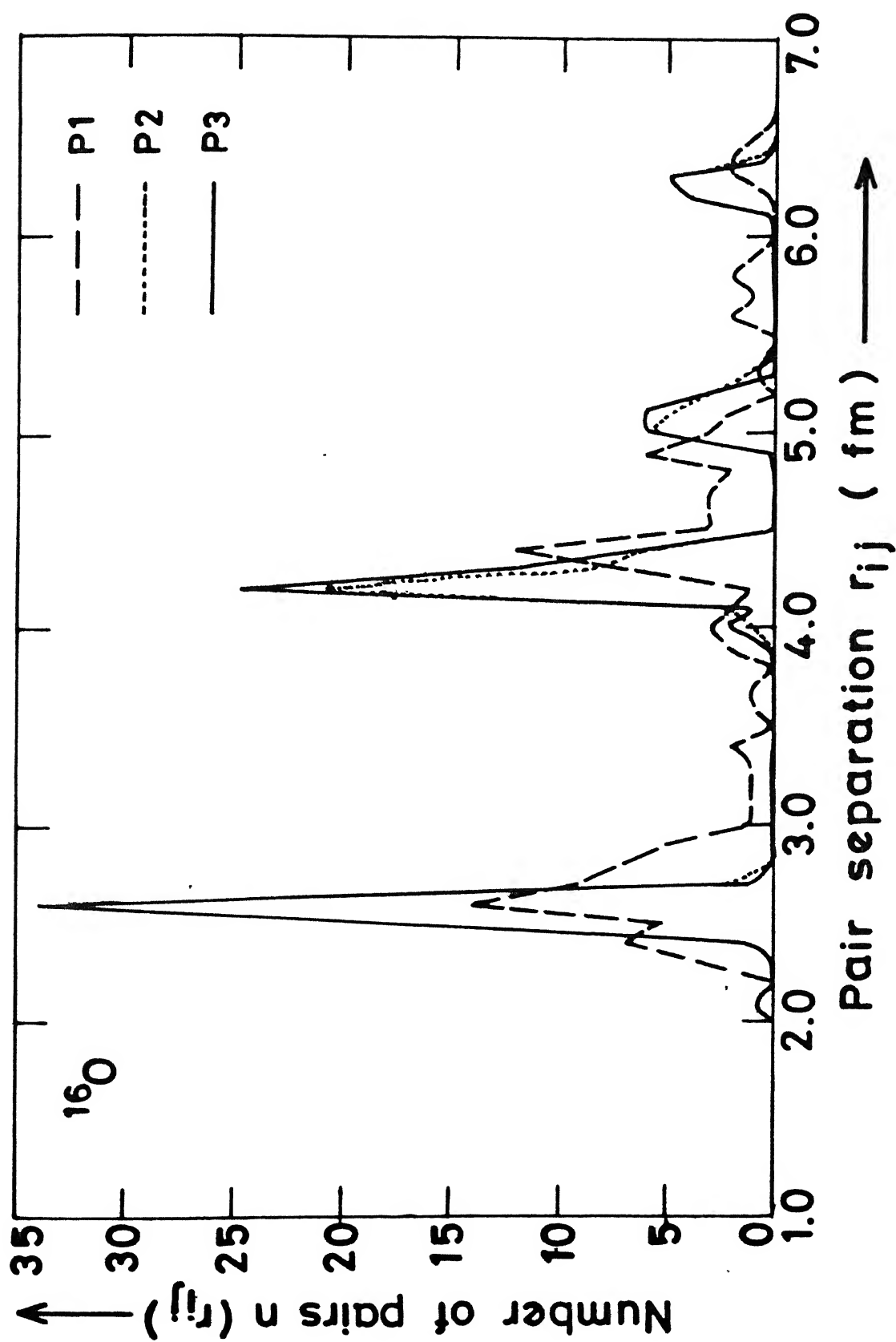


FIGURE 4.1 Pair-distribution in the ground-state configurations of  $^{16}\text{O}$  with the potentials P1, P2 and P3.

of pairs  $n(r_{ij})$  for a given pair separation distance  $(r_{ij})$ , for these configurations. Pair-distributions for the  $^{16}\text{O}$  configuration with the potentials P2 and P3 are quite identical and that with the potential P1 also has peaks similar to those for P2 and P3.

Thus, all the above ground-state configurations have nearly identical structural properties. The two-body potentials P1, P2, and P3 are plotted in Figure 4.2. These potentials have nearly identical depths (-2.9 MeV), and positions of minima (2.6 fm). These NN potentials mainly differ in their long-range attractive tails - potentials with larger values of  $r_0$  have longer tails. Nearly identical minima of the two-body potentials give rise to the identical properties of their corresponding ground-state configurations.

From the above discussion it is clear that any differences in the calculated fusion cross sections for the  $^{16}\text{O}+^{16}\text{O}$  reactions with the above potentials should then be due to the differences in the potentials in the tail region only. Fusion cross sections for the  $^{16}\text{O} + ^{16}\text{O}$  reaction with the potentials P1 and P2 are calculated for  $E_{\text{CM}} = 16.7, 37.6$  and  $66.8$  MeV, and with the potential P3 for  $E_{\text{CM}} = 13.5, 16.7, 20.2, 24.1, 28.3, 32.8, 37.6, 48.3, 66.8$  and  $104.5$  MeV (corresponding to  $v_{\text{CM}} = 0.9, 1.0, 1.1, 1.2, 1.3, 1.4, 1.5, 1.7, 2.0$  and  $2.5$  fm per  $10^{-22}$  sec. respectively). The calculated fusion cross sections are shown in Figure 4.3 as a function of  $E_{\text{CM}}^{-1}$ . Comparison of the fusion cross sections

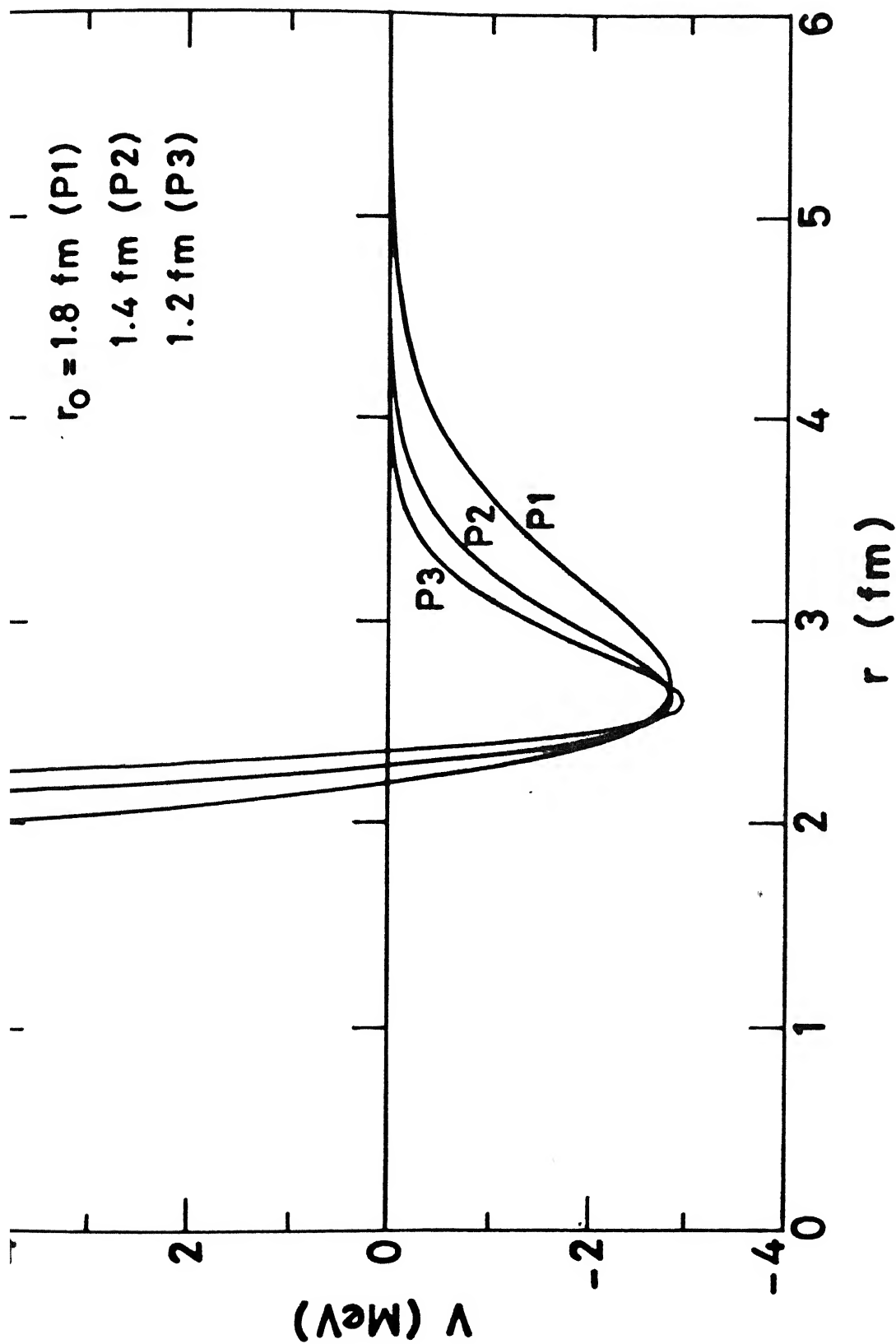


FIGURE 4.2 The effective NN potential (eq. 4.1) with the different values of  $r_0$  and the other parameters

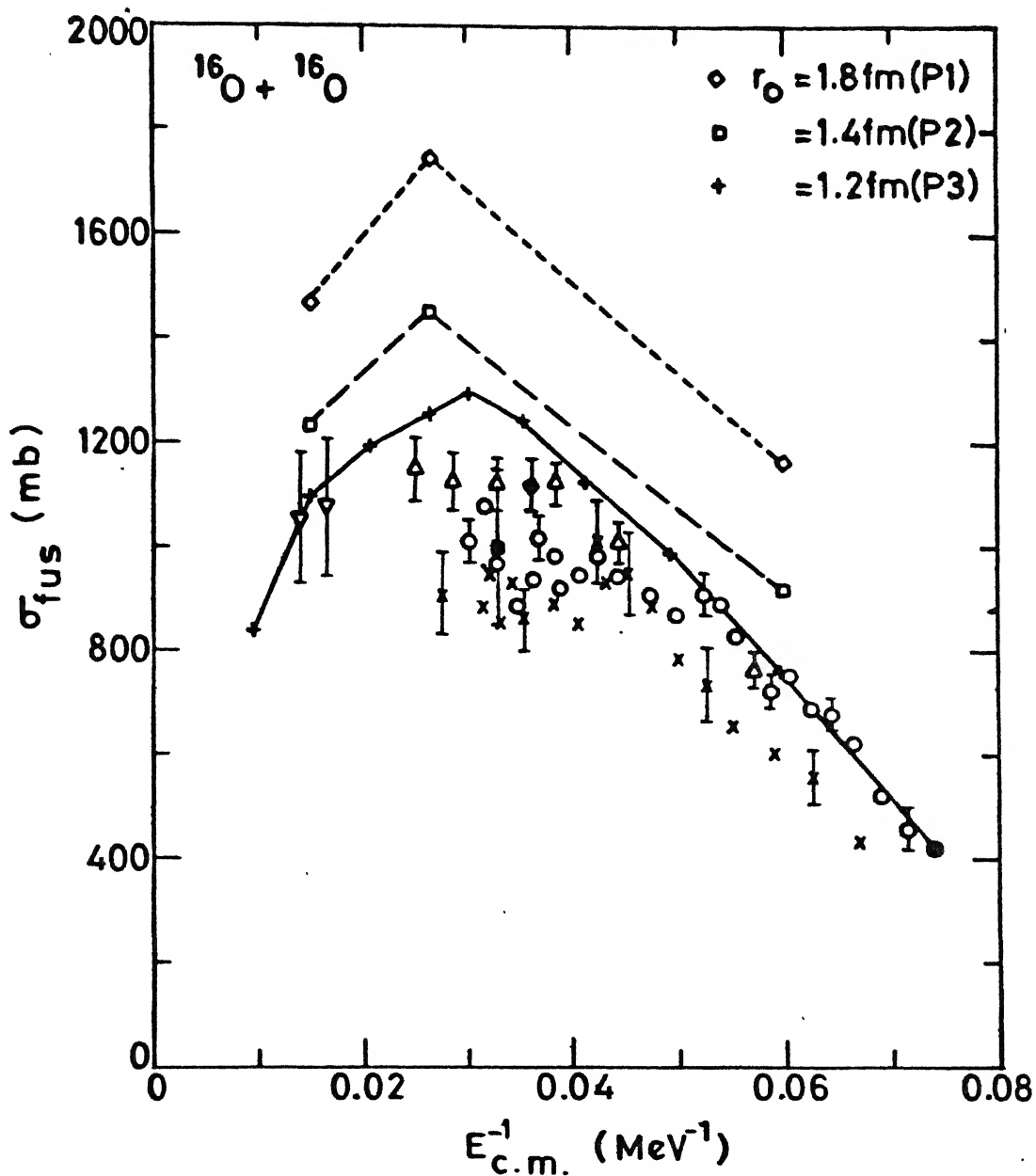


FIGURE 4.3

Fusion cross section Vs.  $E_{CM}^{-1}$  for the  $^{16}\text{O} + ^{16}\text{O}$  reaction with the potentials P1, P2 and P3. For a given potential the calculated points at different values of  $E_{CM}^{-1}$  are connected with straight lines to guide the eye. Experimental data are shown by  $\circ$  (Ref. 8),  $\times$  (Ref. 9),  $\Delta$  (Ref. 10),  $\blacklozenge$  (Ref. 11),  $\blacksquare$  (Ref. 12) and  $\nabla$  (Ref. 13).



calculated with the different potentials clearly shows the sensitivity of the fusion cross sections on the range of the NN potential. Potentials with a longer range give higher values of fusion cross sections, and as the range  $r_0$  decreases, fusion cross sections decrease for all the energies.

To understand the above results, we consider the static one-dimensional potential model, according to which fusion cross sections are given by<sup>7</sup>

$$\sigma_{\text{fusion}} = \pi R_B^2(\ell=0) \left[ 1 - \frac{V_B(\ell=0)}{E_{\text{CM}}} \right] \quad (4.2)$$

where  $R_B(\ell = 0)$  is the barrier radius and  $V_B(\ell = 0)$  is the barrier height for a head-on collision (i.e.  $\ell$  or  $b = 0$ ). This model gives a reasonably good description of fusion excitation functions on the lower energy side, just above the fusion barrier. The model, however, does not give good agreement on the higher energy side due to the increasing importance of the dynamical effects. Even so, the expression 4.2 is useful in understanding the sensitivity of fusion cross sections on the range  $r_0$ .

Therefore, we find the barrier parameters  $V_B(b = 0)$  and  $R_B(b = 0)$  for the  $^{16}\text{O} + ^{16}\text{O}$  reaction with the different potentials in the sudden-approximation. In the sudden-approximation, the ion-ion potential is calculated as a function of the centre-of-mass separation ( $R_{\text{CM}}$ ), keeping the configurations of the two nuclei frozen. Figure 4.4 shows the static ion-ion potential for the

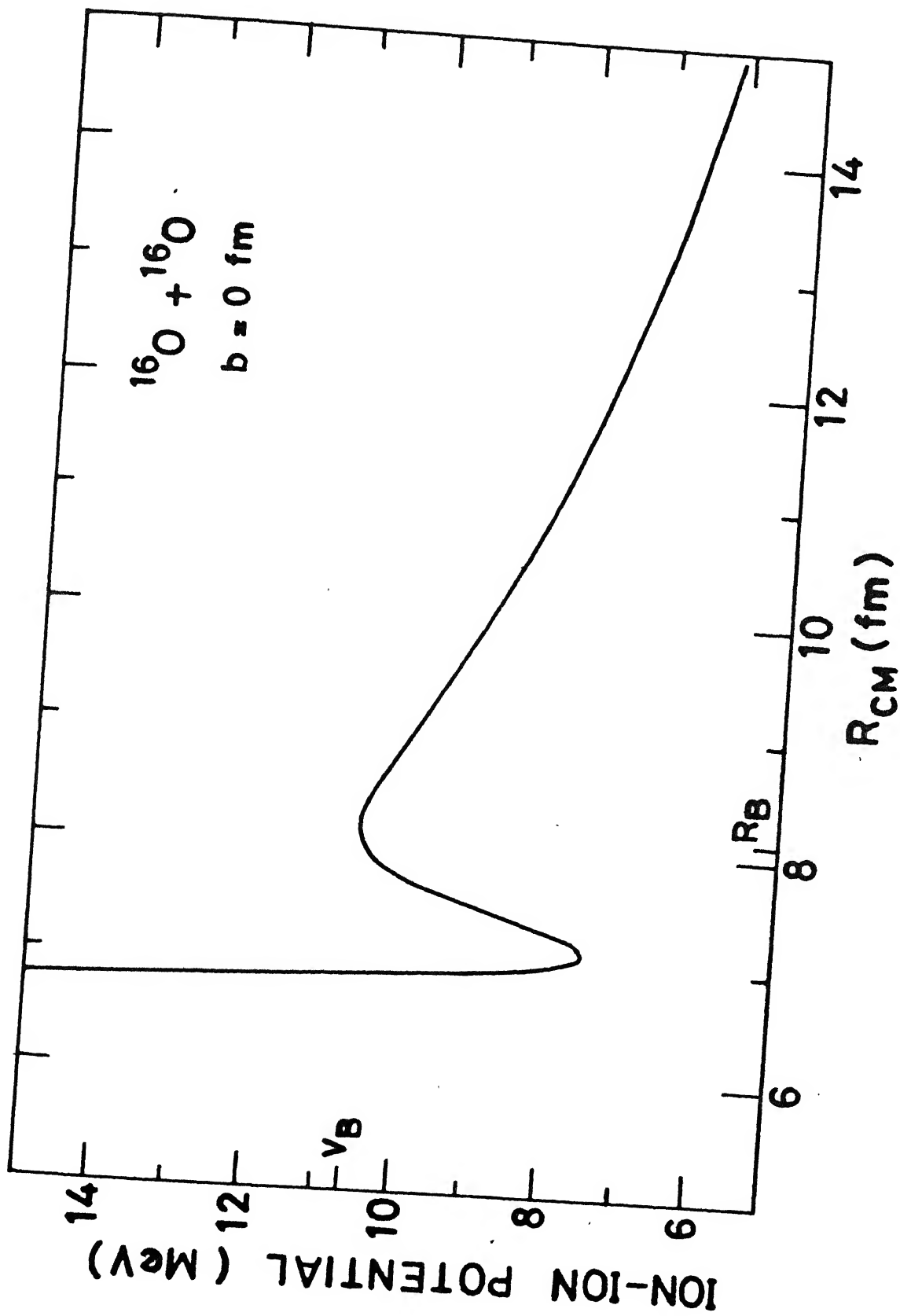


FIGURE 4.4 Static fusion barrier for the  $^{16}\text{O} + ^{16}\text{O}$  reaction with the potential P3.

$^{16}\text{O}+^{16}\text{O}$  system with the potential P3 for one of the initial-relative-orientation at  $b=0$ . The barrier parameters, averaged over 12 initial orientations for the different potentials P1, P2, and P3, are given in Table 4.3. As the value of  $r_0$  decreases, the NN potential (eq. 4.1) becomes less attractive in the tail region (see Figure 4.2). Thus the attractive part in the ion-ion potential decreases with the decreasing value of  $r_0$ , and therefore, the height of the fusion barrier ( $V_B$ ) increases and the radius ( $R_B$ ) decreases. Therefore, according to eq. 4.2 fusion cross sections decrease with decreasing values of  $r_0$  for a given value of  $E_{\text{CM}}$ . This qualitatively explains the sensitivity of fusion cross sections to the range of the NN potential.

In Figure 4.5, we plot fusion cross sections with the potential P3, calculated with eq.4.2 and the barrier parameters given in Table 4.3. Comparison of this result with the results of the dynamical-calculations with the same potential, shows that fusion cross section agree reasonably well in the two cases in the lower energy region. At higher energies, however, the one-dimensional potential model fails to reproduce the observed trend for fusion cross sections as a function of  $E_{\text{CM}}^{-1}$ . This is because of the increasing importance of the dynamical effects at higher energies which are neglected in the derivation of eq. 4.2 due to the sudden-approximation. It is remarkable that the dynamical calculation of fusion cross sections in the classical-microscopic approach satisfactorily reproduces the

TABLE 4.3

Average values of the static-barrier parameters for the  $^{16}\text{O}+^{16}\text{O}$  system ( $b=0$ ) with different potentials

Potential	$r_o$ (fm)	$V_B$ (MeV)	$R_B$ (fm)
P1	1.8	9.29	9.43
P2	1.4	10.41	8.47
P3	1.2	10.80	8.32

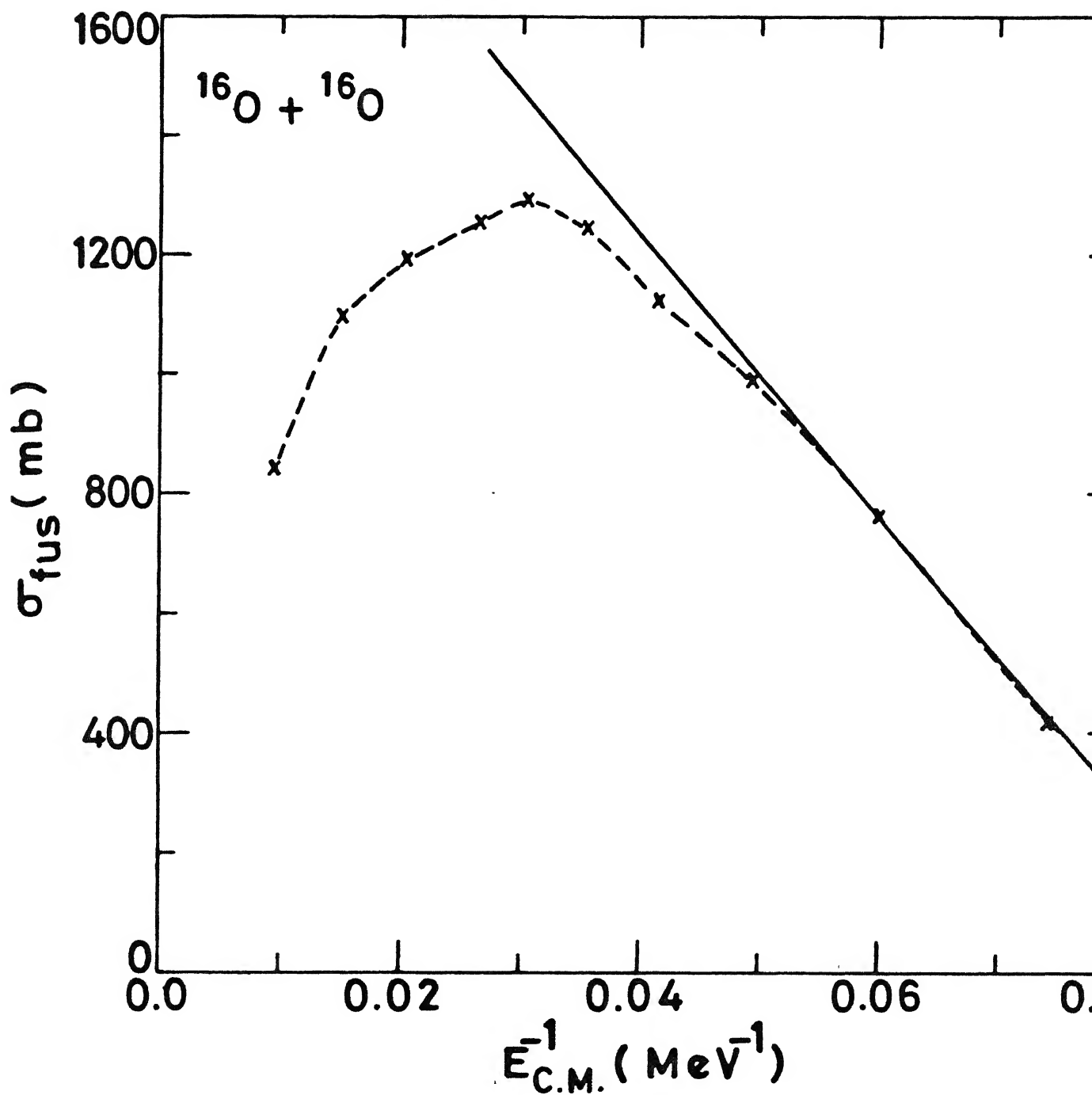


FIGURE 4.5

Fusion cross section Vs.  $E_{\text{CM}}^{-1}$  for the  $^{16}\text{O}+^{16}\text{O}$  reaction. The solid line is the prediction of the static 1-dimensional potential model (eq. 4.2) with the barrier parameters for the reaction given in Table 4.3 for the potential P3. Dashed curve shows the prediction of the dynamical calculations.

experimentally observed trend for fusion cross sections.

In the Figure 4.3 fusion cross sections for the  $^{16}\text{O}+^{16}\text{O}$  reaction, calculated in the classical-microscopic approach, are also compared with the experimental data.<sup>8-13</sup> Fusion cross sections with  $r_0 = 1.8$  fm (P1) and 1.4 fm (P2) are overestimated compared to the experimental data; while fusion cross sections for the  $^{16}\text{O}+^{16}\text{O}$  reaction with  $r_0 = 1.2$  fm (P3) show good agreement with the experiments.

#### 4.2.2 The $^{40}\text{Ca}+^{40}\text{Ca}$ Reaction

Since fusion cross sections for the  $^{16}\text{O}+^{16}\text{O}$  reaction, calculated with the potential P3 ( $r_0 = 1.2$  fm), agree well with the experiments, we use the same potential for the study of a heavier system. Fusion cross sections for the  $^{40}\text{Ca}+^{40}\text{Ca}$  reaction are calculated using the potential P3. Calculated fusion cross sections for  $E_{\text{CM}} = 60, 82$  and  $94$  MeV are plotted in Figure 4.6 and compared with the experimental determination of the fusion cross section.<sup>14-16</sup>

The ground-state properties of  $^{40}\text{Ca}$  generated with the potential P3 are given Table 4.4. The parameters of the potential P3 give about 5% less binding energy and a 12% larger value of the rms radius of  $^{40}\text{Ca}$  compared to the experimental values. As shown in chapter 3, section 3.3, fusion cross sections depend also on the ground-state properties of the colliding partners. The bigger

TABLE 4.4

Parameters of the potential (eq. 4.1) and the calculated binding energy and rms radius of  $^{40}\text{Ca}$  in THE ground-states with different potentials

	P3	P4	Experiments
$r_0$ (fm)	1.2	1.2	
$V_0$ (MeV)	3360.0	1155.0	
$C$ (fm)	2.35	2.07	
Binding energy (MeV)	-326.0	-342.1	-342.1
rms radius (fm)	3.96	3.53	3.53

size of ions tends to enhance the probability for fusion due to the increased overlap between the ions. Therefore, in Figure 4.6 we find that fusion cross sections for the  $^{40}\text{Ca}+^{40}\text{Ca}$  reaction calculated with the potential P3 are also overestimated compared to the experimental data.<sup>14-16</sup>

The inability of this classical-microscopic model in simultaneously reproducing the correct ground-state properties for both the  $^{16}\text{O}$  and  $^{40}\text{Ca}$  nuclei with the same set of the potential parameters may be due to the neglect of quantum mechanical effects which might be playing an important role in the structure of these doubly magic nuclei. Nevertheless, a deviation of about 12% in the rms radius from the experimental value does not seem to be too bad for a purely classical model with a very simple form of the two-body NN potential (eq. 4.1). It may be pointed out that a similar situation also arises for the ground-state properties in the Hartree-Fock calculations which use a simple density independent interaction.<sup>17</sup>

The above situation then requires that the potential parameters be slightly adjusted to obtain correct ground-state properties of the colliding ions. This becomes necessary in view of the dependence of fusion cross sections on the ground-state nuclear properties. Therefore, the parameters  $V_0$  and  $C$  of the NN potential are readjusted, keeping  $r_0 = 1.2$  fm, such that the experimental ground-state binding energy and the rms radius of  $^{40}\text{Ca}$  are reproduced correctly. Parameters of this potential,



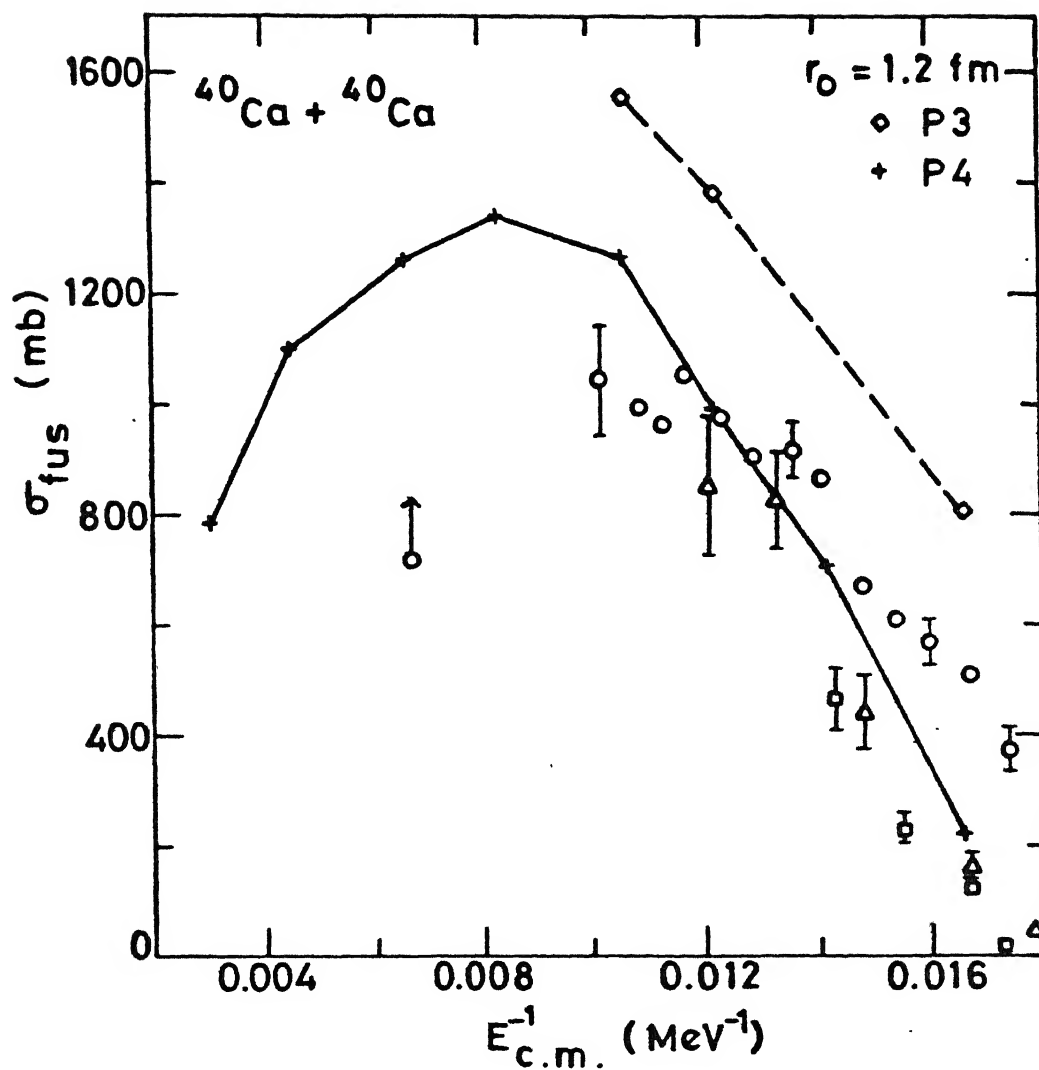


FIGURE 4.6

Fusion cross section Vs.  $E_{CM}^{-1}$  for the  $^{40}\text{Ca} + ^{40}\text{Ca}$  reaction with the potentials P3 and P4. Experimental data are shown by o (Ref. 14),  $\Delta$  (Ref. 15) and  $\square$  (Ref. 16).

called potential P4, are given in Table 4.4.

The potential P4 is plotted in Figure 4.7 and compared with the potential P3. Since both the potentials reproduce the binding energy of  $^{40}\text{Ca}$  to within a difference of 5%, they have nearly the same depth. But the potential P4 has a smaller radius of the minimum compared to that for the potential P3, because the parameters of the potential P4 have been adjusted to reproduce a smaller rms radius of  $^{40}\text{Ca}$  compared to the rms radius generated by the potential P3.

Figure 4.8 shows the pair-distributions  $n(r_{ij})$  for the  $^{40}\text{Ca}$  configurations with both the potentials P3 and P4. In both the cases the pair-distributions have similar peaks, but the peaks for the  $^{40}\text{Ca}$  configuration with the potential P4 are shifted towards smaller pair-separation distances ( $r_{ij}$ ) compared to the peaks of the pair-distribution for the configuration with the potential P3. Thus, both the configurations have similar internal structure, but the configuration with the potential P4 is compressed compared to that with the potential P3. The pair-distribution of  $^{16}\text{O}$  with the potential P3 is also shown in the Figure 4.7. It is interesting to note that the first few peaks for the  $^{16}\text{O}$  and  $^{40}\text{Ca}$  ground-state configurations with the same potential P3 have nearly identical peak-positions.

The calculated fusion cross sections for the  $^{40}\text{Ca}+^{40}\text{Ca}$  reaction with the potential P4 for  $E_{\text{CM}} = 60, 71, 82, 94, 121, 151$ ,

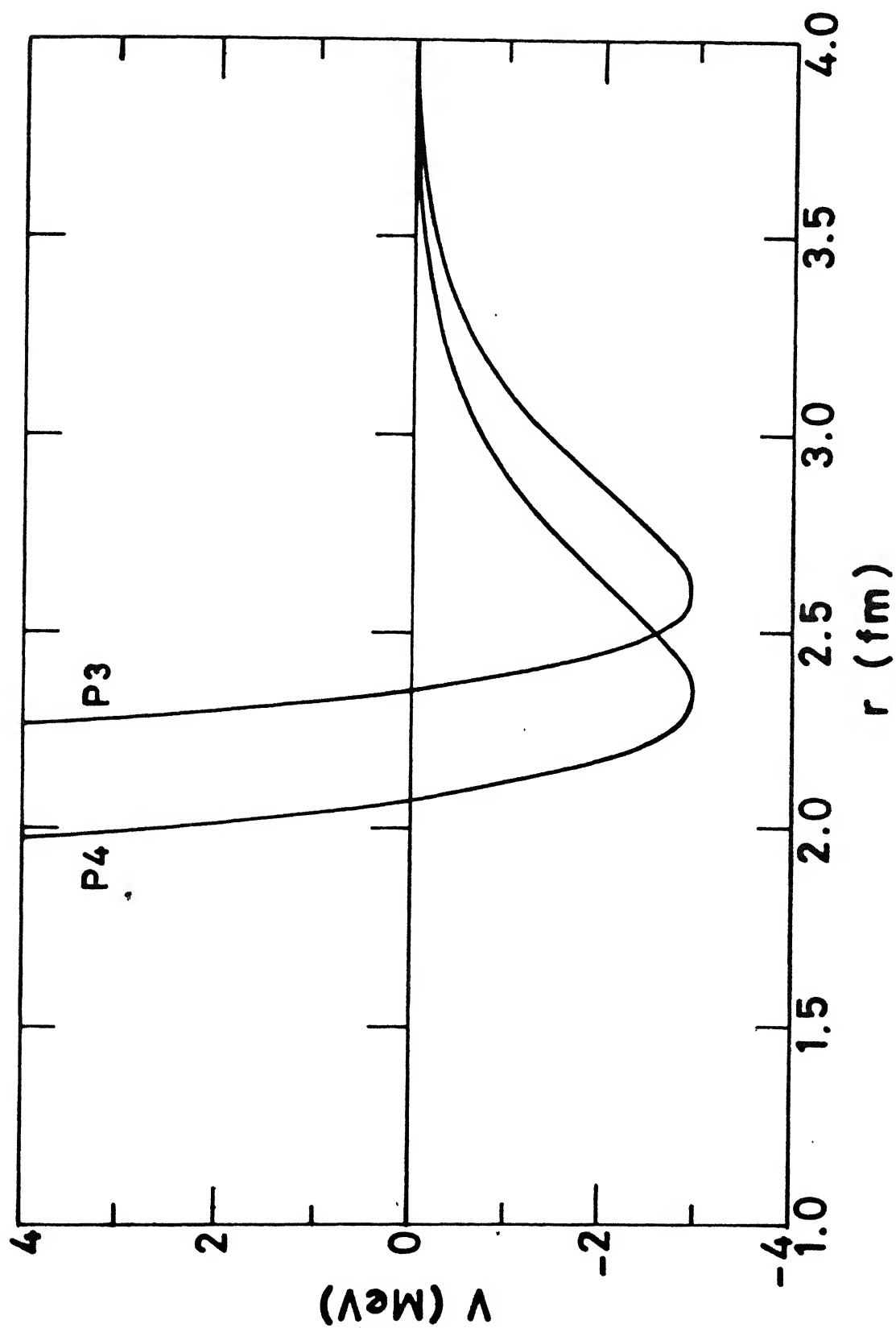


FIGURE 4.7 Plot of the effective NN potentials P3 and P4.

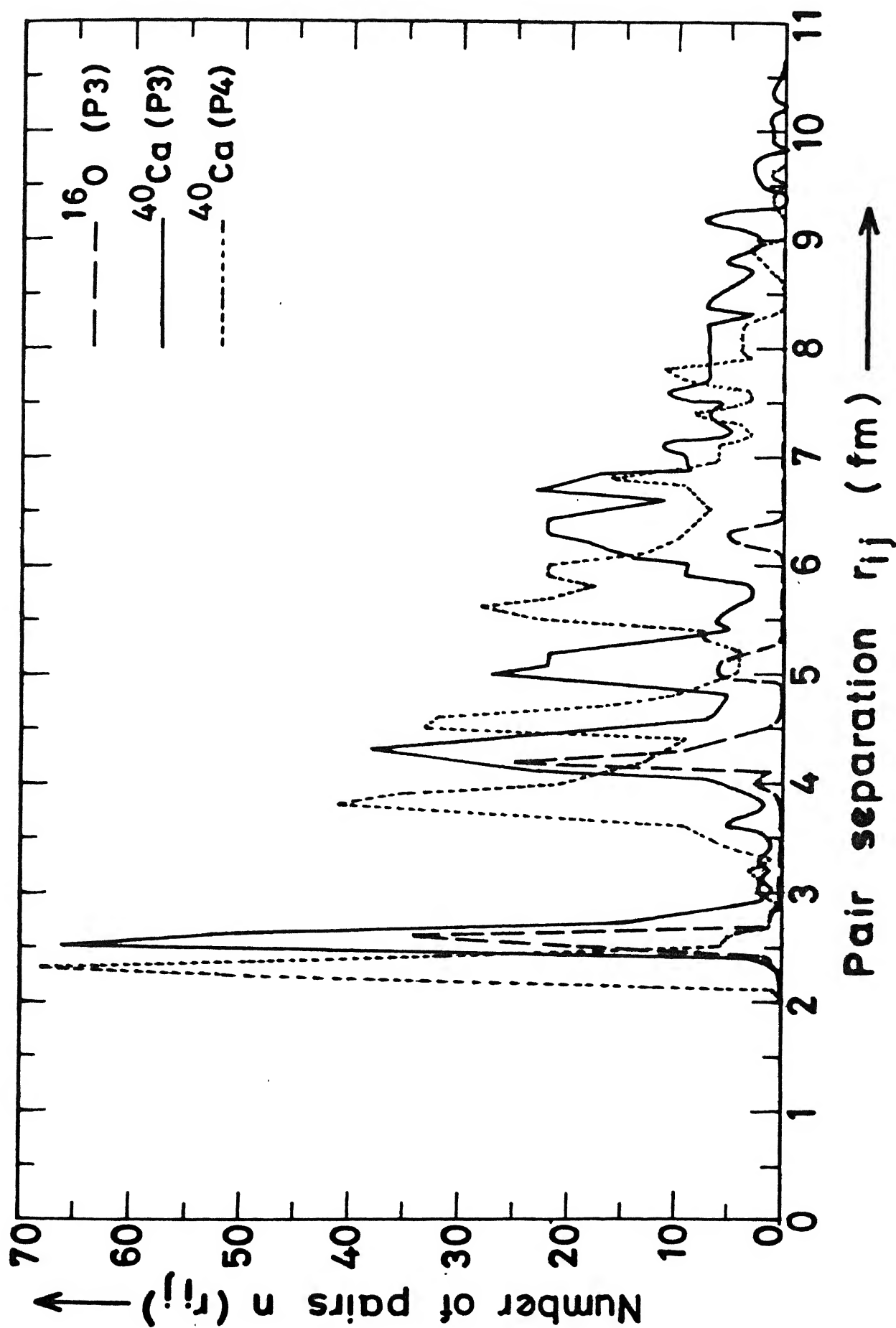


FIGURE 4.8 Comparison of the pair-distributions in the ground-state of  $^{40}\text{Ca}$  with the potential P3 and P4. Pair-distribution of  $^{16}\text{O}$  with the potential P3 is also shown.

221 and 328 MeV (corresponding to  $v_{CM} = 1.2, 1.3, 1.4, 1.5, 1.7, 1.9, 2.3$  and  $2.8$  fm per  $10^{-22}$  sec, respectively) are also shown in the Figure 4.6. Fusion cross sections with the potential  $P_1$  are lower than those with the potential  $P_3$ , and a reasonably good agreement with experimental fusion cross sections is obtained with the potential  $P_4$  in the lower energy region.

The data point of Doubre et al.<sup>14</sup> for  $E_{CM} = 150$  MeV is shown in the Figure 4.6 as a lower limit to the fusion cross section of the  $^{40}\text{Ca}+^{40}\text{Ca}$  reaction, because no measurements have been made of the cross sections for fission following the fusion. For  $E_{CM} > 100$  MeV, no other measurements have been reported. Therefore, a comparison of the calculated results with experiments is not possible at higher energies. Calculated fusion cross sections (Figure 4.6), however, do show the generally observed experimental trend<sup>18</sup> of decreasing fusion cross sections with increasing energy at high energies. Classical macroscopic calculations with the proximity forces,<sup>19</sup> and a classical mean-field calculation<sup>20</sup> also show similar behaviour for the  $^{40}\text{Ca}+^{40}\text{Ca}$  reaction and considerably higher fusion cross sections at  $E_{CM} = 150$  MeV, compared to the data of Doubre et al. Thus, careful determination of the experimental fusion cross sections for the  $^{40}\text{Ca}+^{40}\text{Ca}$  reaction at higher energies, where fission cross section may contribute significantly to the fusion cross section in addition to the evaporation residue cross sections, is needed.

### 4.2.3 Discussions

As discussed in the chapter 2, section 2.2.1, the nuclei in the present calculations do not have any internal motion in their ground-state and the Fermi-gas motion of nucleons or the zero-point energy arising from the uncertainty principle and the Pauli exclusion principle is explicitly neglected. The explicit neglect of the zero-point energy in the nuclei is then directly reflected in the effective NN potential used in order to obtain correct gross nuclear properties.

For normal nuclear densities ( $\rho = 0.165$  nucleon/fm<sup>3</sup>) the average separation between the nucleons is about 2.4 fm. Therefore, the minima of the NN potentials are also located near this value (2.6 fm), with a correspondingly large repulsive core (2.0 - 2.4 fm) (see Figure 4.2) which gives correct rms radius in the ground states of a frozen configuration of point nucleons. Since the kinetic energy in the ground state is equal to zero in the present approach, the total binding energy is equal to the potential energy. Therefore, only a shallow depth of about 2-3 MeV is required for the effective NN potential to obtain correct binding energies. Thus, we find that the effective NN potentials in the model calculations have large repulsive cores and shallow depths.

A large repulsive core of the NN potential creates an excluded volume effect around a nucleon and prevents close

collisions between a large number of nucleons of the two nuclei. The net result of this effect is then somewhat similar to that of the Pauli exclusion principle which does not allow the nucleons to come close together.<sup>21</sup> However, the saturation properties of nuclei are due to a much more complicated balance between the attractive nuclear forces and the repulsion created by the exclusion principle. The inability of the model to simultaneously reproduce the nuclear properties in different nuclei with the same potential parameters may also be due to the inclusion of the Pauli repulsion only in a very approximate way by choosing a larger repulsive core.

The close collisions between a large number of nucleons of the two nuclei are prevented at lower energies due to the large repulsive core. Hence, we find that at energies just above the Coulomb barrier and at the critical impact parameter ( $b_{cr}$ ) the two nuclei just stick to each other like mud balls and keep revolving around a common axis (see Figure 4.9), with a very few nucleons transferred between them. Therefore, in the present calculations, internal excitations and the resulting shape deformation is the predominant mechanism for dissipation of the energy from the relative motion. Some energy also goes in the rotational motion of the combined system at non-zero impact parameters.

Apart from the dissipation of the relative kinetic energy, fusion of two heavy ions also depends upon a critical balance of

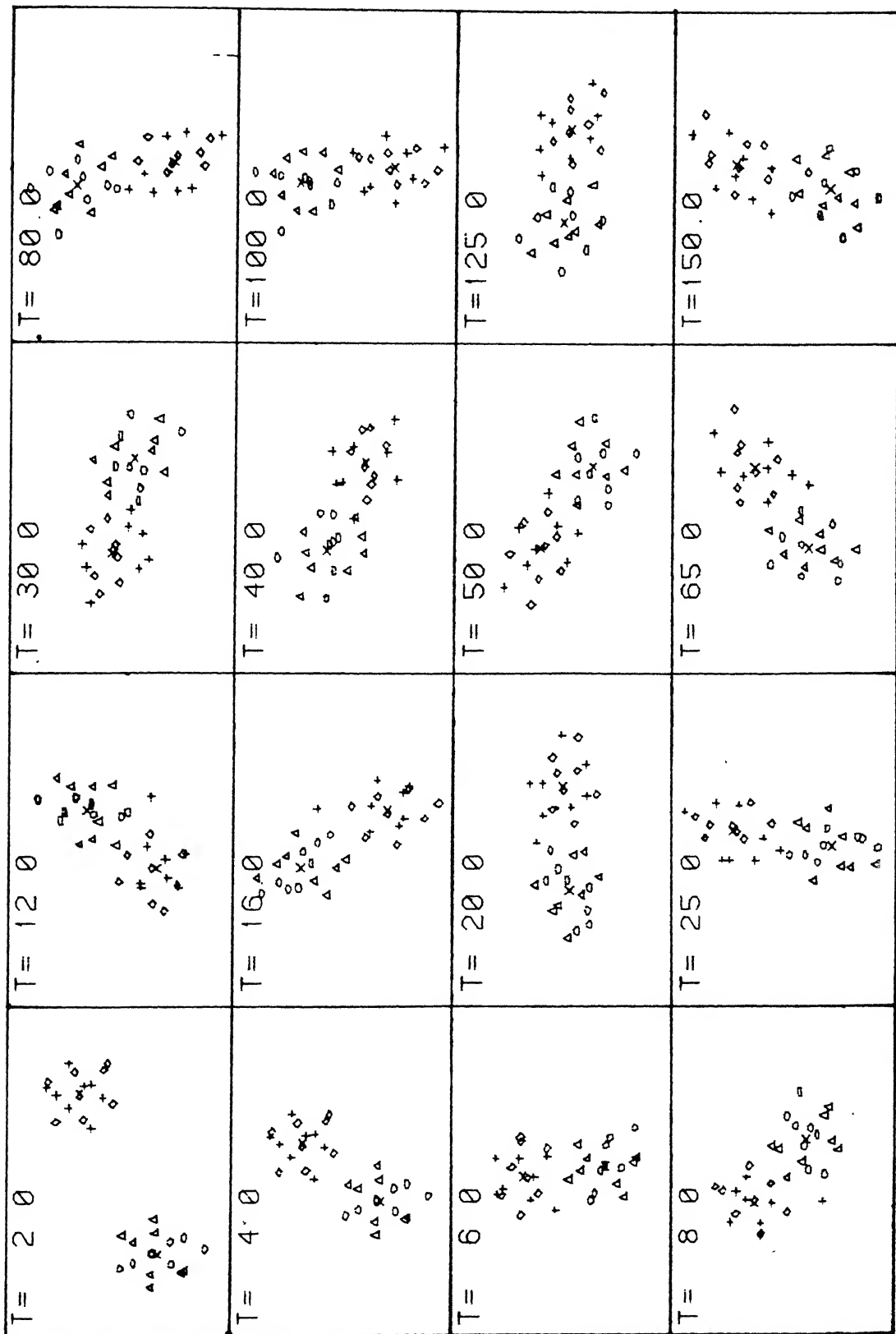


FIGURE 4.9 The coordinate-projections of the  $^{16}\text{O}+^{16}\text{O}$  collision

at  $E_{\text{CM}} = 66.8 \text{ MeV}$  and  $b = 5.4 \text{ fm}$ . The time  $T$  in each



the attractive and repulsive forces in the system. Since the effective NN potentials in the present calculations have large core radii, a short-range attractive tail is required to satisfactorily reproduce the experimental fusion cross sections. Thus, we find that an effective NN potential that correctly reproduces the gross nuclear properties and at the same time gives a reasonably good agreement with the experimental fusion cross sections is required to be quite a narrow potential with the range parameter  $r_0 = 1.2$  fm (potentials P3 and P4).

The compressibility coefficient (K) for infinite nuclear matter is given by

$$K = k^2 \frac{\partial^2 E/A}{\partial k^2} \bigg|_{k = k_F} \quad (4.3)$$

where  $k_F$  is the Fermi-momentum. For a finite nucleus, K is given by

$$K = R^2 \frac{\partial^2 E/A}{\partial R^2} \bigg|_{R = R_0} \quad (4.4)$$

We calculate the compressibility coefficient (K) for  $^{16}_8\text{O}$  with the potentials P1, P2, and P3. We calculate the compressibility coefficients by small radial expansions and contractions of the corresponding nuclei around their ground-state configurations and calculating the binding energies of the compressed or expanded

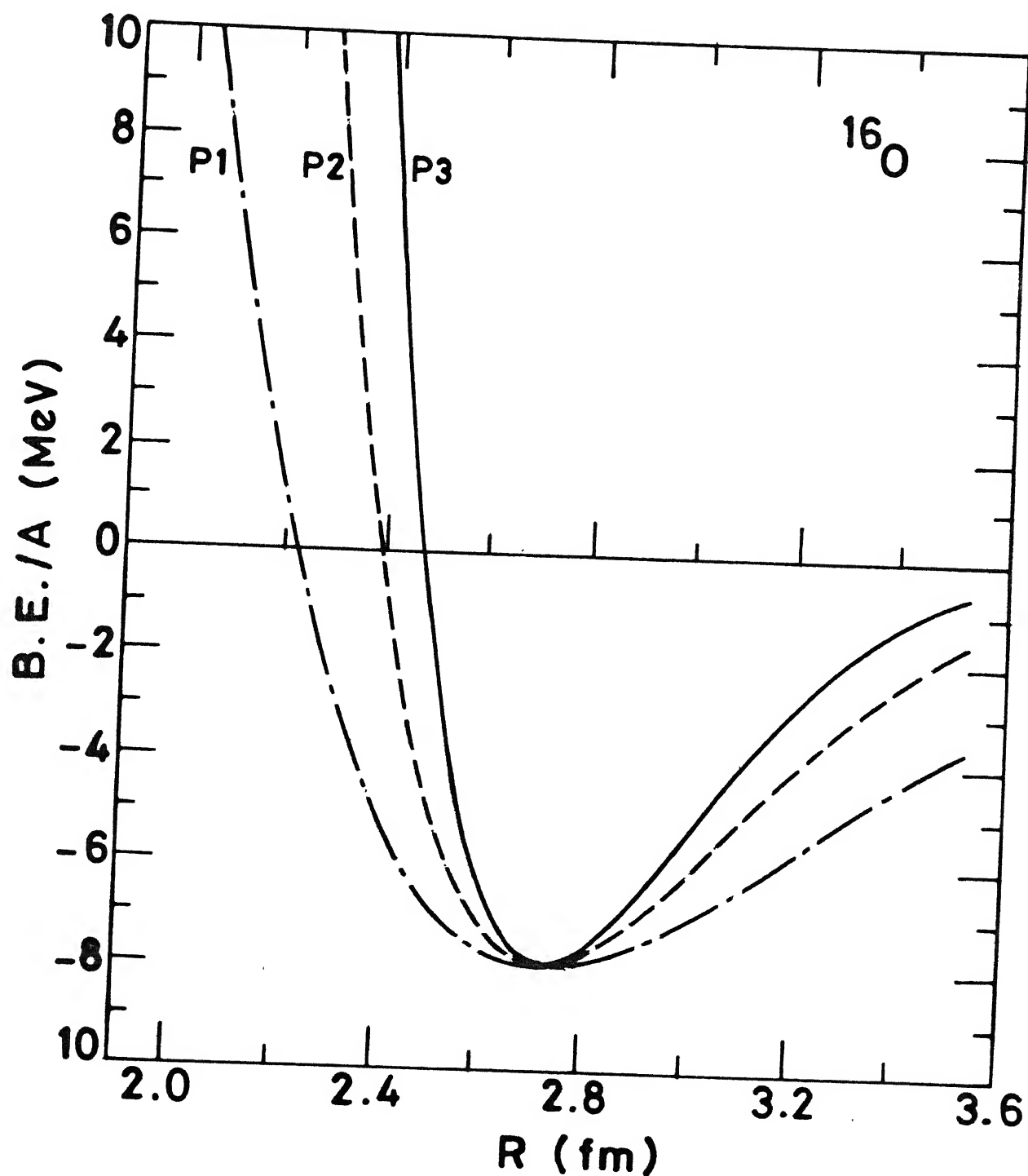


FIGURE 4.10

The binding energy  $\frac{\text{per nucleon}}{\text{Vs.}}$  the rms radius of the compressed or the expanded configurations of  $^{16}\text{O}$  with the potentials P1, P2 and P3.

### 4.3 HEAVY-ION COLLISIONS AT HIGH ENERGIES

#### 4.3.1 $\ell$ -Window For Fusion

An unexpected outcome of the TDHF theory is the prediction of the existence of an angular momentum window ( $\ell$ -window) for fusion at high bombarding energies above a certain threshold value, above which fusion of heavy-ions takes place only between a lower limit ( $\ell_c$ ) and an upper limit ( $\ell_u$ ).<sup>23-26</sup> The fall of the fusion cross sections at high energies in the TDHF calculations is then not due to a limitation in the angular momentum ( $\ell_{cr}$ ) or the impact parameter ( $b_{cr}$ ) but instead due to the opening of this low  $\ell$ -window. Several experiments<sup>27-31</sup> have been performed to check this prediction, but so far no conclusive experimental evidence has been found for the existence of the  $\ell$ -window for fusion.

In a pseudo-particle simulation of the TDHF calculation,<sup>32</sup> it is shown that the non-fusion of heavy-ions at high incident energies and low impact-parameters follows a coherent flow through motion of nucleons of one nucleus past the surface of the other nucleus. The TDHF calculations on some asymmetric systems, such as  $^{16}\text{O} + ^{24}\text{Mg}$  (Ref. 26), also clearly show such transparency effects of passing of one nucleus through the other. This result is, therefore, mainly due to the long mean-free-path of nucleons in the nuclei and the suppression of the two-body collisions in the mean-field calculations which give rise to the increased transparency of the nuclei in near central collisions above a

threshold energy.

On the other hand, two-body collisions are naturally built-in the classical-microscopic approach through the two-body potentials. The mean-free-path of nucleons is also very short in such calculations (zero in the frozen ground-states). Therefore, classical-microscopic approach does not show any such transparency effects. The TDHF calculations<sup>23</sup> predict opening of an  $\ell$ -window for the  $^{16}\text{O}+^{16}\text{O}$  reaction at a threshold energy of  $E_{\text{CM}} = 27$  MeV. The present classical-microscopic calculation of the  $^{16}\text{O}+^{16}\text{O}$  reaction with the potential P3 does not show any  $\ell$ -window even upto  $E_{\text{CM}} = 150$  MeV. Figure 4.11 shows a head-on ( $b = 0$ ) collision of  $^{16}\text{O}+^{16}\text{O}$  at  $E_{\text{CM}} = 150$  MeV which leads to fusion of the two nuclei. For  $E_{\text{CM}} \leq 150$  MeV the two nuclei fuse at all the impact parameters from zero to  $b_{\text{cr}}$ . Figures 4.12(a-c) show the  $^{16}\text{O}+^{16}\text{O}$  reaction at  $E_{\text{CM}} = 200$  MeV and different impact parameters. For  $E_{\text{CM}} > 150$  MeV, and at low impact parameters a number of nucleons evaporate prematurely from the highly excited combined system, leaving behind a residual nucleus which breaks up in a relatively short period of time. Such events lead to what is called "incomplete fusion". The number of nucleons evaporating prematurely decreases as the impact parameter is increased, but the two nuclei reseparate leading to deep-inelastic scattering (Figure 4.12c). As the incident energy is further increased we find that more and more nucleons evaporate in the near central collisions. Therefore, we conclude that there is no  $\ell$ -window for fusion in the

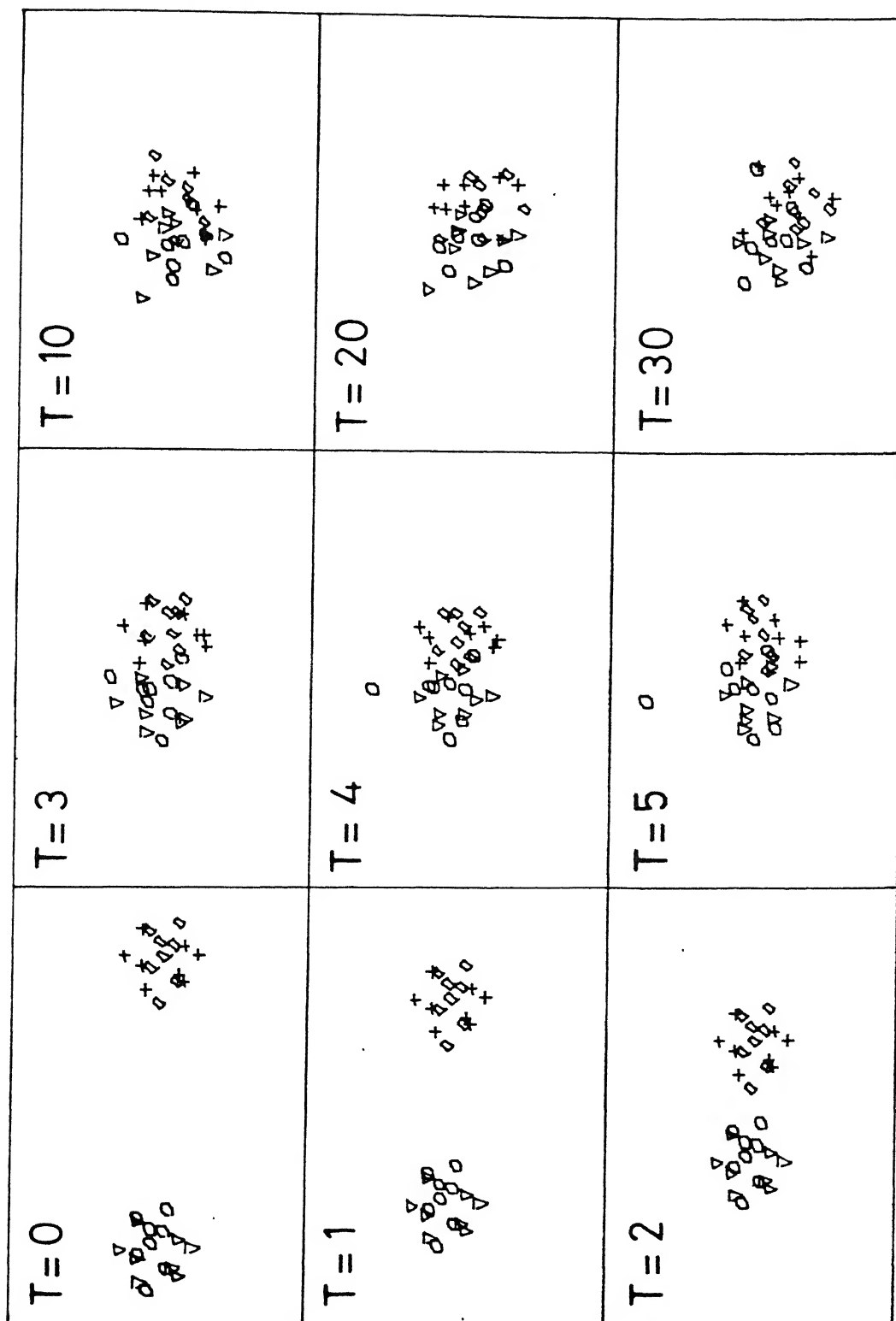


FIGURE 4.11 Same as in Figure 4.9 but for  $E_{CM} = 150$  MeV and  $b = 0.0$  fm.  
Size of each frame is  $30\text{ fm} \times 20\text{ fm}$ .

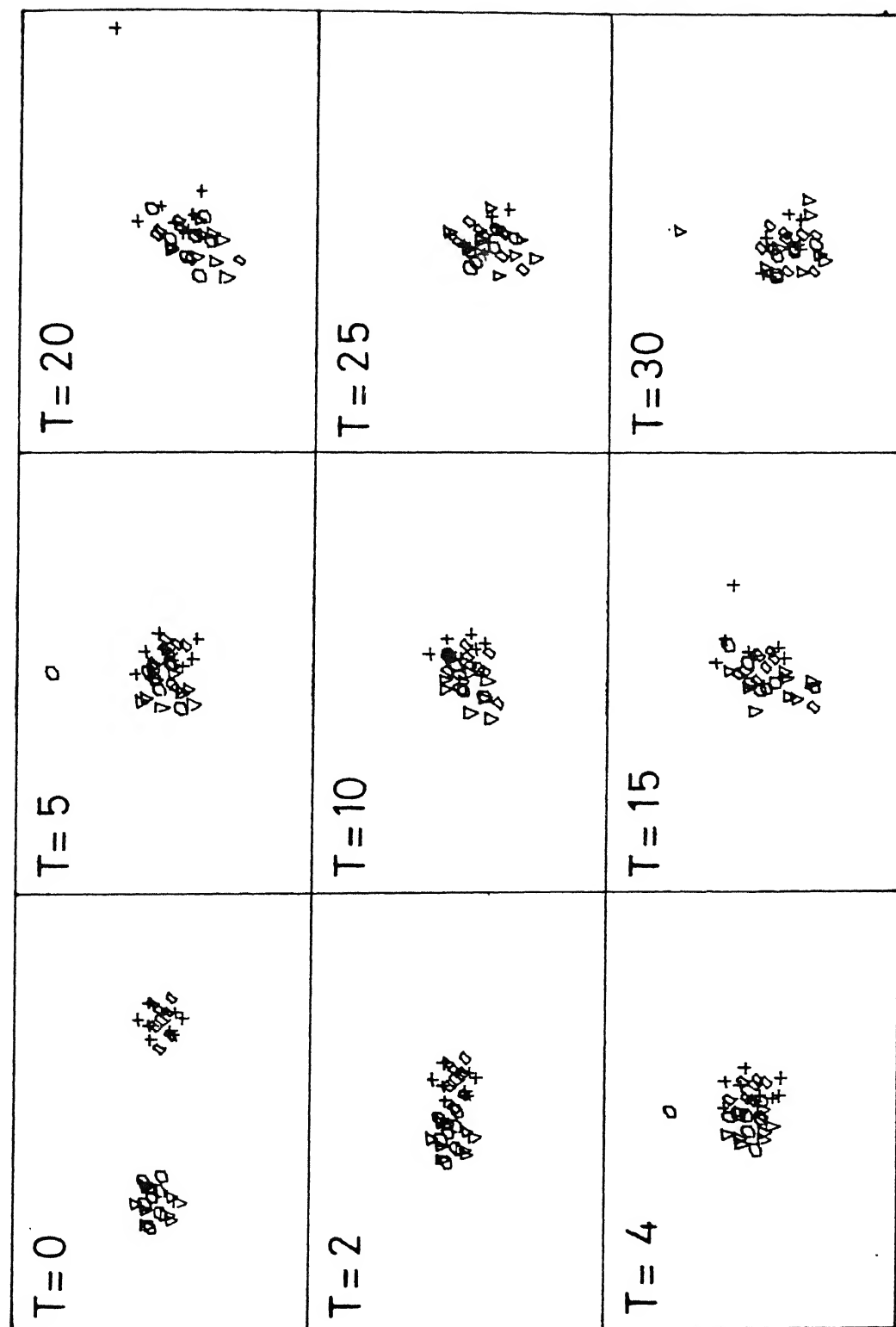


FIGURE 4.12 (a) Same as in Figure 4.9 but for  $E_{CM} = 200$  MeV and  $b=0.0$  fm, Size of each frame is  $48\text{ fm} \times 32\text{ fm}$ .

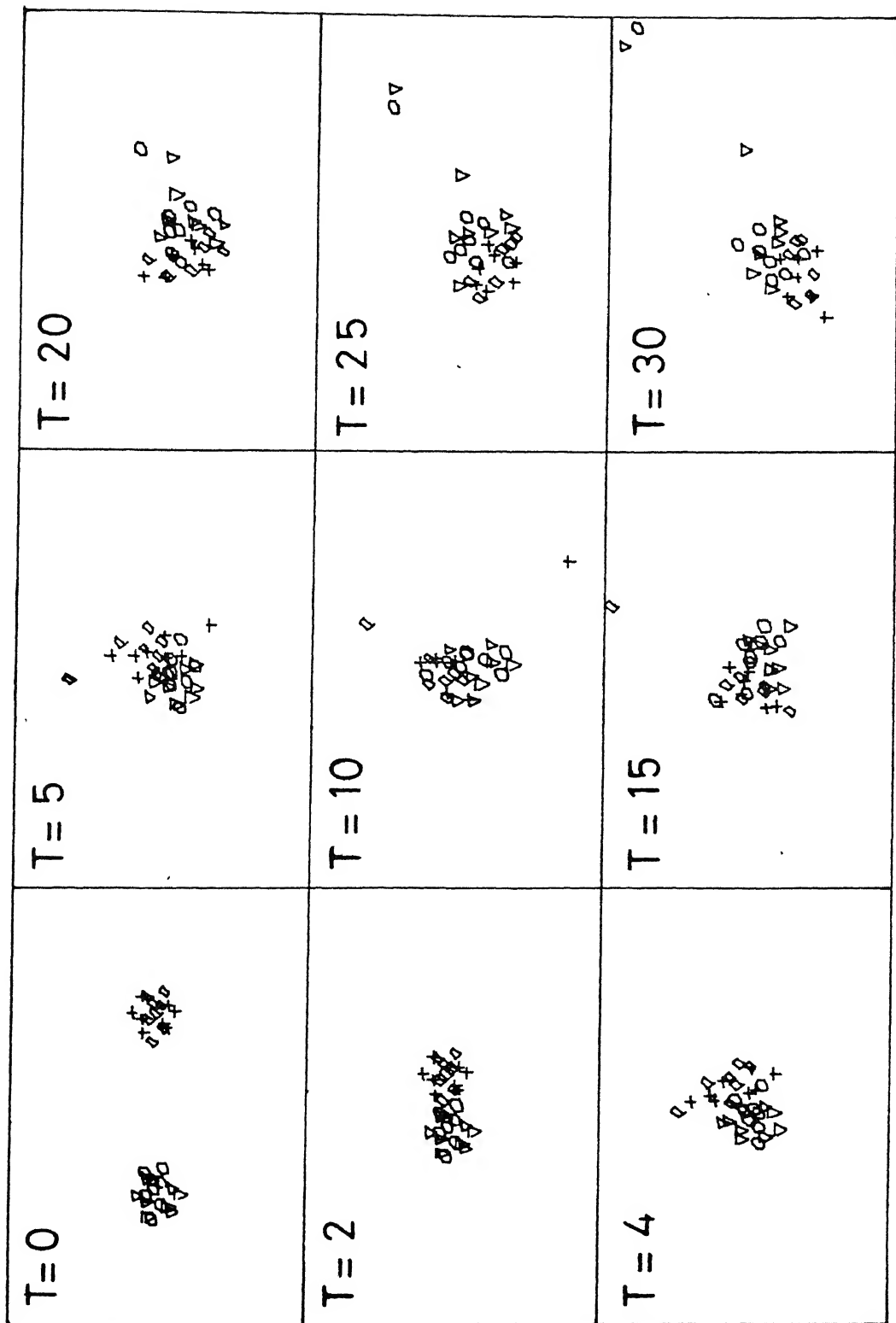


FIGURE 4.12 (b) Same as in Figure 4.12 (a) but for  $b = 1.0$  fm.

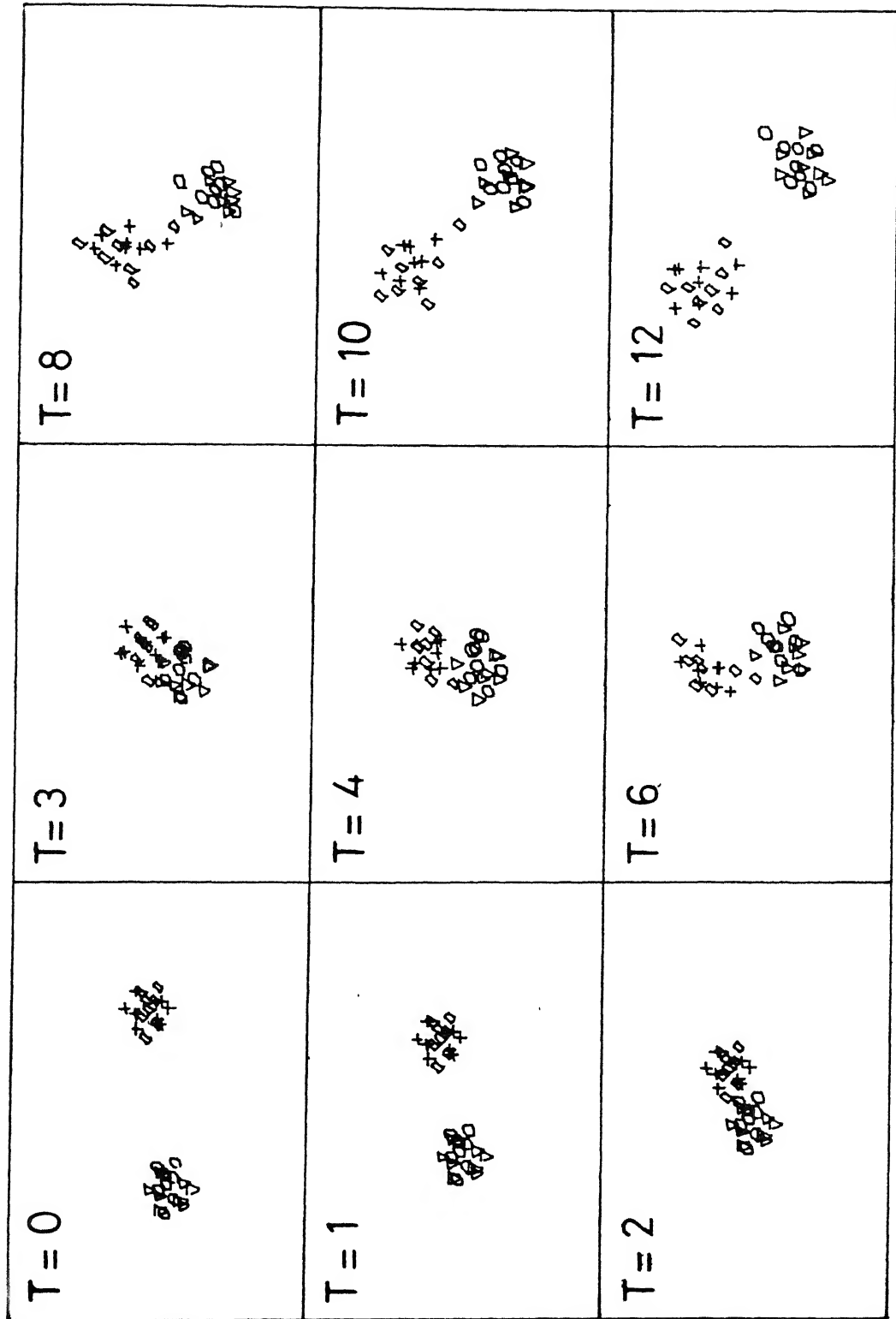


FIGURE 4.12 (c) Same as in Figure 4.12 (a) but for  $b = 3.0$  fm.



classical microscopic approach. In an earlier calculation also it was concluded by Mani<sup>5</sup> that there is no  $\ell$ -window in the classical microscopic approach.

It is interesting to note that in some recent calculations also,<sup>34-37</sup> it has been observed that the inclusion of the two-body collision terms in the mean-field TDHF theory brings about additional damping of the relative motion. The  $\ell$ -window for fusion disappears in such calculations with reasonable relaxation times for the two-body collisions. Some other calculations<sup>38</sup> have also reported the disappearance of the  $\ell$ -window when the two-body collisions are incorporated into their calculations.

#### 4.3.2 Sideward-Flow Of Nuclear Matter

Another interesting aspect of heavy-ion collisions at high incident energies is the experimental observation<sup>39-42</sup> of the collective flow of nuclear matter at finite angles in the transverse directions. The flow angle ( $\theta_F$ ) increases smoothly from  $0^\circ$  in the peripheral collisions to  $90^\circ$  in the central collisions ( $b=0$ ).

Classical-Microscopic calculations also show the "sideward-flow" or the "side-splash" of nuclear matter in the high-energy heavy-ion collisions. Figure 4.13 shows the time evolution of a head-on collision ( $b=0$ ) in the  $^{40}\text{Ca}+^{40}\text{Ca}$  reaction with the potential P4 at  $E_{\text{CM}} = 418$  MeV/nucleon. Figure 4.14 shows

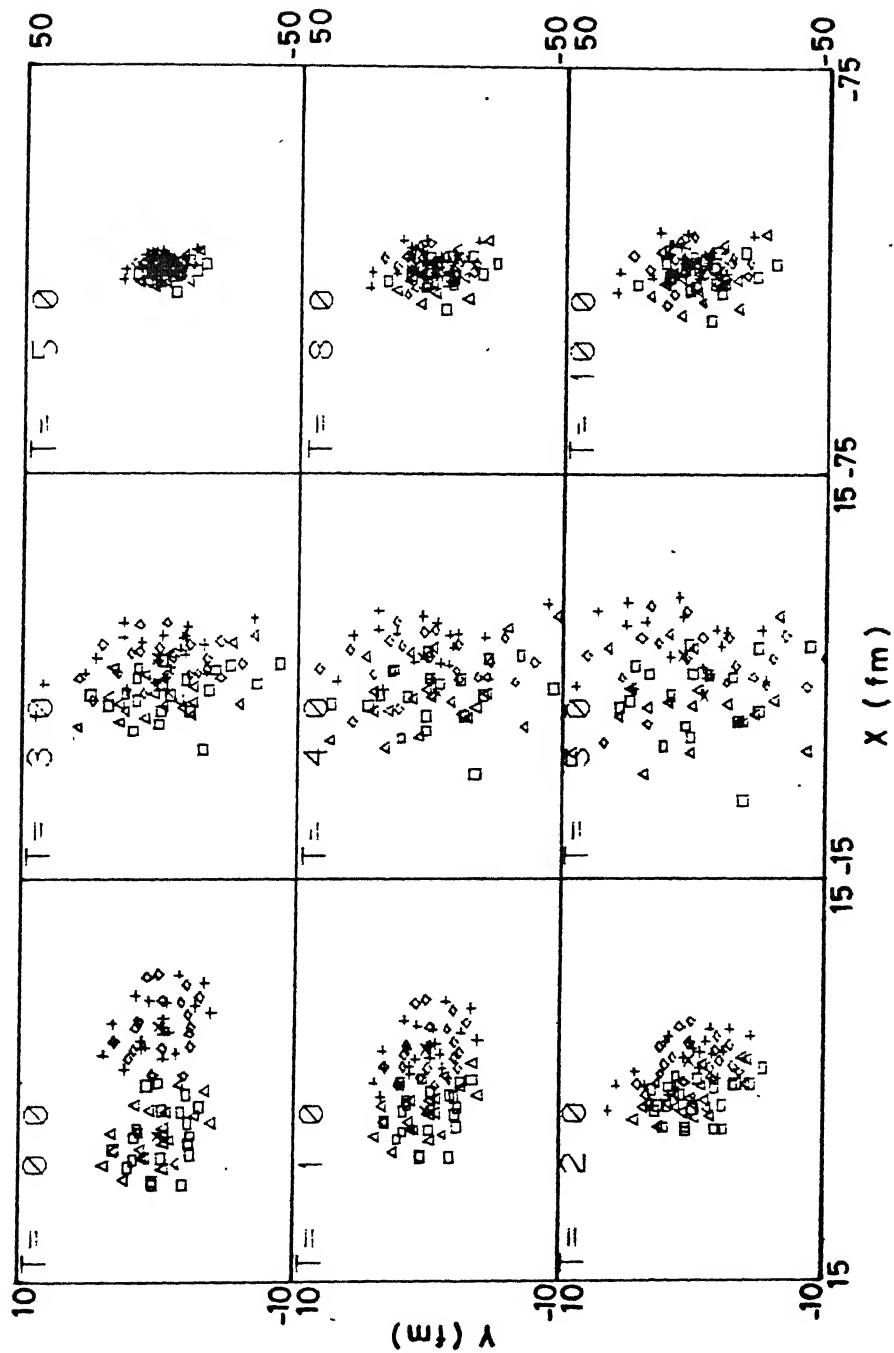


FIGURE 4.13

The coordinate-projections of the  $^{40}\text{Ca}+^{40}\text{Ca}$  collision at  $E_{\text{CM}} = 418$  MeV/nucleon and  $b = 0.0$  fm. The time  $t$  is in the unit of  $10^{-22}$  sec.

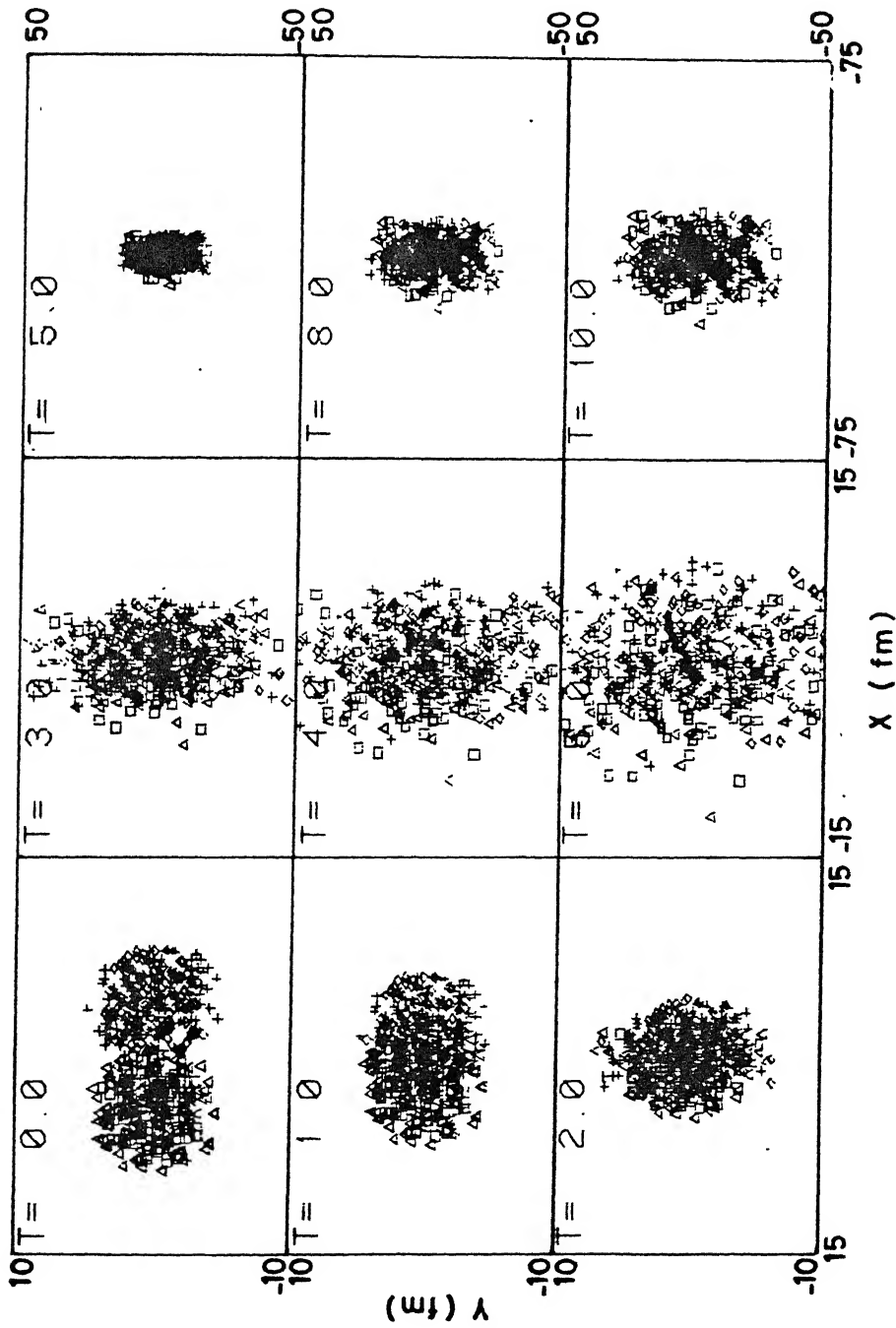


FIGURE 4.14

Same as in Figure 4.13 but the Figure shows a superposition of the coordinate-projections of the reaction for six initial-orientations of the colliding nuclei.

the effect of averaging over different initial orientations by superposing the  $b=0$  event for six different initial orientations on the same plot. The sideward-flow of nuclear matter in the direction nearly perpendicular to the beam axis is clearly seen in the Figures 4.13 and 4.14. At higher impact parameters the angle of the collective flow decreases from  $90^\circ$ . Figure 4.15 shows an event at  $b = 4.5$  fm.

Here, we are interested in only showing qualitatively the observation of the collective flow in the present calculations. The flow angle ( $\theta_F$ ) can be computed from a sphericity analysis of the kinetic energy flow tensor<sup>43</sup> or from a transverse momentum analysis<sup>44</sup>.

The distribution of flow angles calculated by Molitorius et al.<sup>1</sup> for the Nb+Nb reaction in a similar classical-microscopic model shows good agreement with the experiments. Flow angle distributions in nuclear hydrodynamics calculations<sup>45</sup> also agree well with the experimental data. However, due to the transparency effects as discussed in section 4.3.1, the mean field calculations such as TDHF do not show any collective flow in the transverse direction<sup>46</sup>. Cascade calculations<sup>47,48</sup> also do not show this effect. A detailed study of the collective flow of nuclear matter can be useful for the determination of the equation-of-state of nuclear matter<sup>49</sup>.

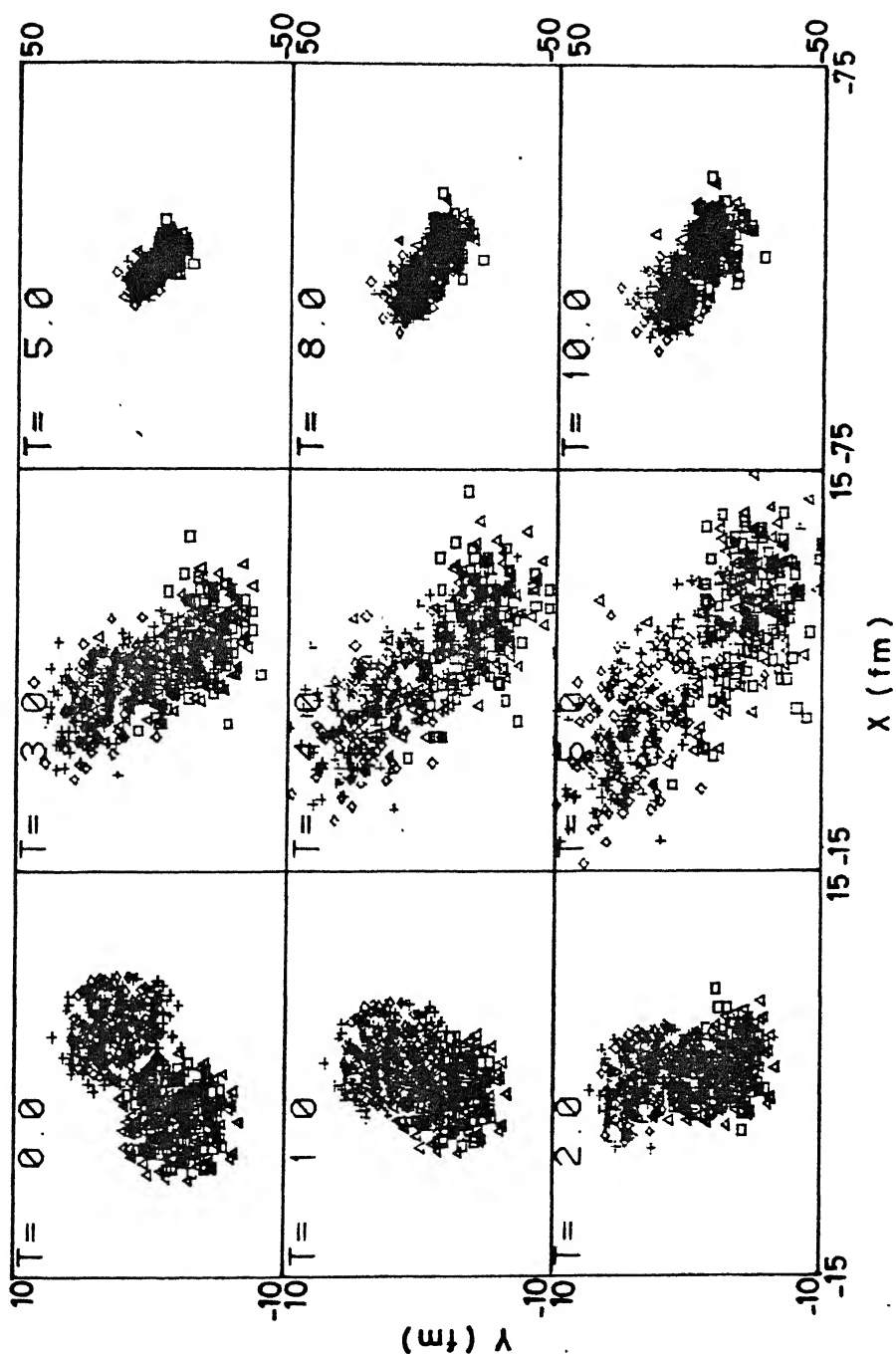


FIGURE 4.15

Same as in Figure 4.14 but for  $b = 4.5$  fm.

#### 4.4 SUMMARY AND CONCLUSIONS

In this chapter, we have presented some studies of  $^{16}\text{O}+^{16}\text{O}$  and  $^{40}\text{Ca}+^{40}\text{Ca}$  reactions in the classical-microscopic approach. We choose a soft-core gaussian form of the NN potential, which allows us to suitably vary the range of the NN potential. With this potential a systematic study of the dependence of fusion cross sections on the range of the effective NN potential is carried out for the  $^{16}\text{O}+^{16}\text{O}$  reaction. This study shows that the calculated fusion cross sections are sensitive to the long-range attractive tail of the effective NN potential. In TDHF calculations also, it is found that the use of the different Skyrme interactions gives rise to large differences in the fusion cross sections.<sup>23-25</sup> In the present case, potentials with a longer range cause increased attraction between heavy-ions and give higher values of fusion cross sections. With a proper choice of the parameters of the effective NN potential, we find that the calculated fusion cross sections for the  $^{16}\text{O}+^{16}\text{O}$  and  $^{40}\text{Ca}+^{40}\text{Ca}$  reactions agree reasonably well with the corresponding experimental fusion cross sections.

A qualitative difference shown by the classical-microscopic calculations with the predictions of the TDHF theory is the absence of any  $\ell$ -window for fusion, which is predicted by TDHF calculations. So far there is no experimental evidence also for the existence of any  $\ell$ -window. Recent calculations which incorporate two-body collisions in the TDHF calculations also support the absence of any  $\ell$ -window. This indicates that two-body

collisions are important in heavy-ion collisions even at incident energies of the order of a few MeV/nucleons. Classical-microscopic calculations also show the experimentally observed "sideward-flow" of nuclear matter in high energy collisions. The sideward-flow of nuclear matter in the heavy-ion collisions arises due to the strong transverse coupling between the nucleons with the short mean-free-paths - an effect that is completely absent in the TDHF calculations due to the neglect of two-body collisions.

Thus, we find that the classical-microscopic approach not only gives a good description of heavy-ion collisions at high energies, where the validity of the classical approximations may be obvious, but even at relatively low energies it provides an adequate description of the macroscopic features of heavy-ion reactions such as fusion. Classical-microscopic calculations do not require any additional assumptions such as those of frictional forces or shape parametrizations - assumptions which are often required to be made in the classical-macroscopic approaches to account for the dissipation of the angular momentum and the kinetic energy from the relative motion.

However, the lack of internal kinetic energy in the ground-state of the nuclei in the present calculations is reflected in the shape and strength of the effective two-body potentials for the point-like nucleons. Due to the explicit neglect of this zero-point energy we find that the effective NN

potentials have a large repulsive-core and a shallow depth in order to reproduce the ground-state properties of the nuclei. The range of the NN potential is also small, if it also reproduces the heavy-ion fusion cross sections. Due to the narrow width of the NN potential the nuclear compressibility coefficient has higher values. The problem of the finite size of nucleons and that of the zero-point energy are further addressed in the following chapters.



## REFERENCES

- 1 J.J. Molitoris, J.B. Hoffer, H. Kruse, and H. Stöcker, Phys. Rev. Lett. **53**, 899 (1984).
- 2 S.M. Kiselev and Y.E. Pokrovski, Yad. Fiz. **38**, 82 (1983) [Sov. J. Nucl. Phys. **38**, 46 (1983)].
- 3 P. Ring and P. Schuck, *The Nuclear Many-Body Problem* (Springer-Verlag, Berlin, 1980), chapter 4.
- 4 Y.R. Waghmare, Phys. Rev. **136**, B1261 (1964); H.S. Kohler and Y.R. Waghmare, Nucl. Phys. **66**, 261 (1965).
- 5 T.K. Mani, Ph.D. Thesis, Indian Institute of Technology, Kanpur (1984).
- 6 A. Rahman, Phys. Rev. **136**, A404 (1964).
- 7 U. Mosel, *Treatise on Heavy-ion science*, edited by D.A. Bromley (Plenum, New York 1985), Vol.2, p.3; and references therein.
- 8 I. Tserruya, Y. Eisen, D. Pelte, A. Gavron, H. Oeschler, D. Berndt and H.L. Harney, Phys. Rev. **C18**, 1688 (1978).
- 9 D.G. Kovar, D.F. Greesman, T.H. Braid, Y. Eisen, W. Henning, T.R. Ophel, M. Paul, K.E. Rehm, S.J. Sanders, P. Sperr, J.P. Schiffer, S.L. Tabor, S. Vigdor, B. Zeidman and F.W. Prosser, Jr., Phys. Rev. **C 20**, 1305 (1979).
- 10 B. Fernandez, C. Gaarde, J.S. Larsen, S. Pontoppidan, and F. Videbaek, Nucl. Phys. **A306**, 259 (1978).
- 11 A.J. Cole, N. Longequeue, J. Menet, J.J. Lucas, R. Ost and J.B. Viano, Nucl. Phys. **A341**, 284 (1980).
- 12 A. Weidinger, F. Busch, G. Gaul, W. Trautmann and W. Zipper, Nucl. Phys. **A263**, 511 (1976).
- 13 F. Saint-Laurent, M. Conjeaud, S. Harar, J.M. Loiseaux, J. Menet and J.B. Viano, Nucl. Phys. **A327**, 517 (1979).
- 14 H. Doubre, A. Gamp, J.C. Jacmart, N. Poffe, J.C. Roynette and J. Wilczynski, Phys. Lett. **73B**, 135 (1978).
- 15 E. Tomasi, D. Ardouin, J. Barreto, V. Bernard, B. Gauvin, C. Magnago, C. Mazur, C. Ngo, E. Piasecki and M. Ribrag, Nucl. Phys. **A373**, 341 (1982).

- 16 J. Barreto, G. Auger, M. Langevin and E. Plagnol, Phys. Rev. C **27**, 1335 (1983).
- 17 See Chapter 5 in Ref. 3.
- 18 C. Ngô, IL Nuovo Cimento, **81A**, 47 (1984).
- 19 J. R. Birkelund, L.E. Tubbs, J.R. Huizenga, J.N. De and D.Sperber, Phys. Rep. **56**, 107 (1979).
- 20 A. Bonasera, Nucl. Phys. **A439**, 353 (1985).
- 21 A. deShalit, *Theoretical Nuclear Physics* (Jhon Wiley and Sons, 1974)
- 22 J.P. Blaizot, D. Gogny, and B. Grammaticos, Nucl. Phys. **A265**, 315 (1976).
- 23 P. Bonche, B. Grammaticos and S. Koonin, Phys. Rev. C **17**, 1700 (1978)
- 24 J.W. Negele, Rev. Mod. Phys. **54**, 914 (1982); and references therein.
- 25 K.T.R. Davies, K.R.S. Devi, S.E.Koonin and M. Strayer, see Ref.5, vol.3, p.3; and references therein.
- 26 K.R.S. Devi, A.K. Dhar, M.R. Strayer, Phys. Rev. C **23**, 2062 (1981).
- 27 A. Lazzarini et al, Phys. Rev. C **24**, 309 (1981).
- 28 G. Rosner et al, Nucl. Phys. **A385**, 174 (1982).
- 29 H. Ikezoe et al, Nucl. Phys. **A456**, 298 (1986).
- 30 S. Kox, A. J. Cole, and R. Ost, Phys. Rev. Lett. **44**, 1204 (1980).
- 31 A. Sazanto de Toledo et al, Phys. Rev. **47**, 1881 (1981).
- 32 C.Y. Wong, Phys. C **25**, 1460, (1982).
- 33 P.E. Hodgson, *Nuclear Heavy-Ion Reactions* (Clarendon press, Oxford, 1978).
- 34 M. Tohyama, Phys. Lett. **160B**, 235 (1982).
- 35 M. Tohyama, Phys. Lett. **163B**, 14 (1985).
- 36 M. Tohyama, Nucl. Phys. **A437**, (1985).

- 37 M. Tohyama, Phys. REv. C36, 187 (1987).
- 38 C. Gregoire, D. Jaquet, M. Pi, B. Remaud, F. Sebille, E. Suraud, P. Schuck, and L. Vinet, preprint ISN 87-39 (1987).
- 39 H. A. Gustafsson et al, Phys. Rev. Lett. 52, 1590 (1984).
- 40 R. E. Renford et al, Phys. Rev. Lett. 53, 763 (1984).
- 41 H. G. Ritter et al, Nucl. Phys. A447, 3C (1985).
- 42 K. G. R. Doss et al, Phys. Rev. Lett. 57, 302 (1986).
- 43 M. Gyulassy, K. Frenkel, and H. Stöcker, Phys. Lett. 110B, 185 (1982).
- 44 P. Danielewicz and G. Odyniec, Phys. Lett. 157B, 146 (1985).
- 45 G. Buchwald et al, Phys. Rev. Lett. 52, 1594 (1984).
- 46 J. Aichelin and G. Bertsch, Phys. Rev. C31, 1730 (1985).
- 47 Y. Yariv and Z. Fraenkel, Phys. Rev. C20, 2227 (1979).
- 48 J. Cugnon, T. Mizutani, and J. Vandermeulen, Nucl. Phys. A352, 505 (1981).
- 49 H. Stöcker and W. Greiner, Phys. Rep. 137, 277 (1986).

## CHAPTER 5

THE EFFECTS OF THE FINITE SIZE OF NUCLEONS  
("FROZEN" WAVE- PACKET CALCULATIONS)

## 5.1 INTRODUCTION

The calculations presented in the previous chapters show that the classical microscopic approach gives a good description of the macroscopic features of heavy-ion reactions over a wide range of energies. In this approach, however, nucleons are considered as point particles. With a point particle description of a nucleus we find that the density of nuclear matter in the nuclei is not continuous. It is also difficult to introduce the zero-point motion in the ground state of nuclei due to premature evaporation of nucleons from the nuclei. The NN potentials which reproduce correct ground state properties of a nucleus in Chapter 4 have large repulsive core radii and shallow depths; the range is also small if it also reproduces the experimental fusion cross sections for the heavy-ion reactions. These features of the NN potential result in a narrow width of the potential and very high values of the compressibility coefficients for the nuclei.

On the other hand, we know from the experiments that nucleons do have finite size. Charge rms radius of protons is experimentally estimated to be about 0.8 - 0.9 fm.<sup>1</sup> Thus, the size of a nucleon is not negligible compared to the average internucleon separation in the ground state which is about 2.4 fm.

Therefore, to study what effects does the finite size of nucleons have on the classical NN potential, compressibility coefficients, nuclear density distributions, and heavy-ion fusion cross sections we consider nucleons as extended objects in the configuration space. While it may be relatively easier to consider nucleons as simply sharp spheres of given radii for this purpose, in the present calculations we, however, choose gaussian density distributions to describe a nucleon. An advantage of using the gaussian functions is its direct analogy with the minimum uncertainty wave packets which are also gaussians. In fact, a semi-classical wave-packet description is developed in the next chapter in which the zero-point motion of nucleons is explicitly included in the ground state and the width of the wave packets <sup>are</sup> ~~is~~ also allowed to evolve. In the present chapter, in order to study the effects of the finite size and for the sake of simplicity we assume, however, that the width of the wave packets remains constant in time, that is, we assume that the wave packets are "frozen".

Further assumptions and calculational details are given in section 5.2. In section 5.3 we choose two different size of the gaussian wave packets and study its effect on the NN potential, nuclear compressibility coefficient, nuclear density distribution for  $^{16}\text{O}$  and fusion cross sections for the  $^{16}\text{O}+^{16}\text{O}$  reaction. Finally, summary and conclusions are given in section 5.4.

## 5.2 CALCULATIONAL DETAILS

### 5.2.1 Description of a nucleon

We consider each nucleon as an extended object in the configuration space and describe it by a spherically symmetric gaussian density distribution given by

$$\rho(r) = \frac{1}{(2\pi\sigma^2)^{3/2}} \exp \left( - \frac{(\vec{r} - \langle \vec{r} \rangle)^2}{2\sigma^2} \right) \quad (5.1)$$

The above distribution is normalized with

$$\int \rho(r) d^3r = 1 \quad (5.2)$$

We chose the above gaussian density distribution (eq. 5.1) for a nucleon because of its analogy with the minimum uncertainty wave packets which are given by<sup>2</sup>

$$\phi_i(\vec{r}) = \frac{1}{(2\pi\sigma_i^2)^{3/4}} \exp \left[ \frac{-(\vec{r}_i - \langle \vec{r}_i \rangle)^2}{4\sigma_i^2} + \frac{i}{\hbar} \langle \vec{p}_i \rangle \cdot (\vec{r}_i - \langle \vec{r}_i \rangle) \right] \quad (5.3)$$

where  $\langle \vec{r}_i \rangle$  is the centroid of the  $i^{\text{th}}$  wave packet given by

$$\begin{aligned} \langle \vec{r}_i \rangle &= \int \phi_i^*(r_i) \vec{r}_i \phi_i(r_i) d^3r_i \\ &= \int \vec{r}_i \rho(r_i) d^3r_i \end{aligned} \quad (5.4)$$

The gaussian density distribution (eq. 5.1) is obtained by the relation

$$\rho_i(r) = |\phi_i^* \phi_i| \quad (5.5)$$

The rms radius ( $r_N$ ) of a nucleon described by eq. 5.1 or eq. 5.2 is given by

$$r_N = [\langle r^2 \rangle - \langle r \rangle^2]^{1/2} \quad (5.6)$$

where  $\langle r \rangle$  is given by eq. 5.4 and  $\langle r^2 \rangle$  is given by

$$\langle r^2 \rangle = \int r^2 \rho(r) d^3r \quad (5.7)$$

For the distribution given by (eq. 5.1),  $r_N$  is given by

$$r_N = (3\sigma^2)^{1/2} \quad (5.8)$$

### 5.2.2 Assumptions

Since in the present chapter we are interested only in the study of the effects of the finite size of nucleons on the NN potential, we make the following simplifying assumptions:

(1) Since a generalised wave packet in 3-dimension is given by

$$\rho(x, y, z) = \rho(x) \rho(y) \rho(z) \quad (5.9)$$

with

$$\rho(x) = \frac{1}{(2\pi\sigma_x^2)^{1/2}} \exp \left[ -\frac{(x - \langle x \rangle)^2}{2\sigma_x^2} \right]$$

and similarly for  $\rho(y)$  and  $\rho(z)$ , we have already assumed in the equation 5.1 that the density distribution is spherically symmetric with

$$\sigma_x = \sigma_y = \sigma_z = \sigma \quad (5.10)$$

(2) We assume that all the nucleons in a nucleus have the same value of the rms radius ( $r_N$ ), irrespective of their location in the nucleus and that it has the same value for both the protons and the neutrons. Therefore, we set

$$\sigma_i = \sigma_j = \sigma \quad (5.11)$$

(3) We choose  $\sigma$  such that the rms radius ( $r_N$ ) of each nucleon is approximately equal to the experimental rms charge radius of the protons. We choose a value of 0.8 fm for  $r_N$ . We consider the case of a higher value of  $r_N$  also.

(4) Finally, we assume that the width of each wave packet remains constant in time, i.e.

$$\sigma(t) = \text{constant} = \sigma \quad (5.12)$$

The above assumption leads to the "frozen" wave packet approximation in which we picture nucleons as simply extended objects, which do not change their shape or size in time



### 5.2.3 Equations Of Motion

According to the Ehrenfest theorem the equations of motion of the mean value of the wave packets  $\langle \vec{r}_i \rangle$  are formally identical to the classical equations of motion,

$$m \frac{d^2 \vec{r}_i}{dt^2} = - \vec{\nabla}_i \left( \sum_{j \neq i} V_{ij} (\vec{r}_i - \vec{r}_j) \right) \quad (5.13)$$

except that the quantities which occur on both the sides of this equation are replaced by their average (expectation) values.<sup>3</sup> Therefore, for the motion of the centroids  $\langle \vec{r}_i \rangle$ , we get

$$m \frac{d^2 \langle \vec{r}_i \rangle}{dt^2} = - \vec{\nabla}_i \left[ \sum_{j \neq i} \langle V_{ij} (\vec{r}_i - \vec{r}_j) \rangle \right] \quad (5.14)$$

where  $\langle V_{ij} (\vec{r}_i - \vec{r}_j) \rangle$  is the average potential between the  $i^{\text{th}}$  and the  $j^{\text{th}}$  wave packets and is given by the double folding integral

$$\langle V_{ij} (\vec{r}_i - \vec{r}_j) \rangle = \iint \phi_i^*(\vec{r}_i) \phi_j^*(\vec{r}_j) V_{ij}(\vec{r}_i - \vec{r}_j) \phi_i(\vec{r}_i) \phi_j(\vec{r}_j) d^3 r_i d^3 r_j \quad \dots (5.15)$$

or

$$\langle V_{ij} (\vec{r}_i - \vec{r}_j) \rangle = \iint \rho_i(\vec{r}_i) \rho_j(\vec{r}_j) V_{ij} (\vec{r}_i - \vec{r}_j) d^3 r_i d^3 r_j \dots (5.16)$$

For a central potential  $V_{ij}(\vec{r}_i - \vec{r}_j)$ , the effective potential  $\langle V_{ij} \rangle$  is a function of the separation between the two centroids only, viz  $|\langle \vec{r}_i \rangle - \langle \vec{r}_j \rangle|$ .

Because of the finite size of the wave packets,  $\langle v_{ij}(r_i - r_j) \rangle$  is in general not equal to  $v_{ij} (|\langle r_i \rangle - \langle r_j \rangle|)$ . The equality is maintained only in the special case when  $v_{ij}$  is at the most quadratic in  $(r_i - r_j)$  or, if  $\sigma$  is very small. The right hand side of the equation 5.14 is the average force experienced by the  $i^{\text{th}}$  wave packet due to all the other wave packets in the system.

Numerical procedure for calculation of the trajectories of the centroids is similar to the description given in chapter 2 for point particles.

#### 5.2.4 Ground-State Properties Of Nuclei

The ground-state of a cluster of "frozen" wave packets representing a nucleus is obtained by finding the ground state configuration of the centroids of the wave packets by the methods described in chapter 2 for the point particle calculations. Calculations of the ground-state properties is described below.

(1) The nuclear-matter density  $\rho(r)$  at any given point  $r$  in space is given by

$$\begin{aligned} \rho(r) &= \sum_{i=1}^A |\phi_i(r)|^2 \\ &= \sum_{i=1}^A \rho_i(r) \end{aligned} \quad (5.17)$$

where  $A$  is the mass number of a given nucleus and  $\rho_i(r)$  is given

by equation (5.1).

A cluster of finite number of point nucleons, or wave packets does not have complete spherical symmetry. Therefore, for the purpose of calculating an average radial density distribution, we take an average of  $\rho(r)$  (eq. 5.1) evaluated at a large number of randomly chosen points in the volume of the nucleus at a particular radius ( $r$ ).

(2) The rms radius ( $R$ ) of a nucleus is given by

$$R = \langle r^2 \rangle^{1/2} = \left[ \frac{\int \rho(r) r^2 d^3r}{\int \rho(r) d^3r} \right]^{1/2} \quad (5.18)$$

where  $\rho(r)$  is the nucleon density given by eq.5.17. With the expression for  $\rho_i$  given by equation 5.1, we get

$$\langle r^2 \rangle^{1/2} = \left[ \frac{\sum_{i=1}^A (\langle r_i \rangle^2 + 3\sigma_i^2)}{A} \right]^{1/2} \quad (5.19)$$

With the second assumption (equation 5.11), we get

$$\langle r^2 \rangle^{1/2} = \left[ 3\sigma^2 + \frac{1}{A} \sum_{i=1}^A \langle r_i \rangle^2 \right]^{1/2}$$

and with equation 5.8, we get

$$\langle r^2 \rangle^{1/2} = \left[ r_N^2 + \frac{1}{A} \sum_{i=1}^A \langle r_i \rangle^2 \right]^{1/2} \quad (5.20)$$

The second term in eq. 5.20 is the rms radius of the distribution of the centroids of the wave packets. The first term in eq. 5.20 is the result of folding the wave packets on this distribution, which also corresponds to the size of a nucleus.

(3) The binding energy  $E_0$  is given by

$$E_0 = \sum_{i=1}^A \langle T_i \rangle + \sum_{i=1}^{A-1} \sum_{j>i}^A \langle v_{ij}(r_i - r_j) \rangle \quad (5.21)$$

where, the first term is the total zero-point kinetic energy and the second term is the total potential energy. We have assumed here that in the ground state of a nucleus all the wave packets are stationary, i.e.,

$$\langle P_i \rangle = 0$$

The zero-point kinetic energy  $\langle T_i \rangle$  associated with the wave packets is given by (see Chapter 6)

$$\langle T_i \rangle = \frac{\langle p_i^2 \rangle}{2m} = \frac{3\hbar^2}{2m (4\sigma_i^2)} \quad (5.22)$$

Since we have assumed that all the  $\sigma$ 's are constant in time, it follows from the eq. 5.22 that  $\langle T_i \rangle$  is also constant. Therefore, it contributes only a constant term to the binding energy (eq. 5.21) in the present case. Therefore, in the calculations that follow we first neglect this term in the

expression for the binding energy (eq. 5.21) and in the latter calculations we include this term also.

(4) The nuclear compressibility coefficient (K) is given by

$$K = k_F^2 \frac{\partial^2 (E_0/A)}{\partial k_F^2} \bigg|_{\rho=\rho_0} \quad (5.23a)$$

For a finite nucleus it is given by

$$K = R^2 \frac{\partial^2 (E_0/A)}{\partial R^2} \bigg|_{R=R_{g.s.}} \quad (5.23b)$$

where  $R_{g.s.}$  is the rms radius in the ground state.<sup>4</sup>

### 5.2.5 Potentials and Forces

For the present study, we choose the same form of the NN potential given by eq. (4.1 ) i.e.

$$v_{ij}^N(r_{ij}) = -V_0 (1 - C/r_{ij}) \exp(-r_{ij}^2/r_0^2) \quad (5.24)$$

where,  $r_{ij} = |r_i - r_j|$

We also choose the Coulomb potential between the point protons given by

$$v_{ij}^C(r_{ij}) = 1.44/r_{ij} \quad (\text{MeV}) \quad (5.25)$$

and consider the potential between like pairs to be weaker than that between unlike pairs by about 20% as in the case of calculations in chapter 4.

The double folding integrals (eq. 5.16) for the above potentials for the nucleon wave packets given by eq.5.1 are evaluated in the Appendix B. The result for NN potential (eq. 5.24) with the assumption (2) gives

$$\begin{aligned}
\langle v_{ij}^N(r_i-r_j) \rangle = & -v_o \left[ \frac{r_o^3}{(r_o^2 + 4\sigma^2)^{3/2}} \right. \\
& - \frac{C}{\langle r_{ij} \rangle} \frac{r_o}{(r_o^2 + 4\sigma^2)^{1/2}} \left. \operatorname{erf} \left( \frac{r_o \langle r_{ij} \rangle}{2\sigma (r_o^2 + 4\sigma^2)^{1/2}} \right) \right] \\
& \times \exp \left( -\frac{\langle r_{ij} \rangle^2}{(r_o^2 + 4\sigma^2)} \right) \quad (5.26)
\end{aligned}$$

where

$$\langle r_{ij} \rangle = | \langle r_i \rangle - \langle r_j \rangle | \quad (5.27)$$

is the separation between the centroids of the  $i^{\text{th}}$  and the  $j^{\text{th}}$  wave packets, and  $\operatorname{erf}(x)$  is the error integral given by

$$\operatorname{erf}(x) = \frac{1}{2\pi} \int_0^x e^{-t^2} dt \quad (5.28)$$

The result for the Coulomb potential (eq. 5.25) is given by

$$\langle v_{ij}^C(r_i-r_j) \rangle = \frac{1.44}{\langle r_{ij} \rangle} \operatorname{erf} \left( \frac{\langle r_{ij} \rangle}{2\sigma} \right) \quad (\text{MeV}) \quad (5.29)$$

In the limit of  $\sigma \rightarrow 0$  the expressions (5.26) and (5.29) reduce to the expressions (5.24) and (5.25) respectively.

Magnitude of the average force between the two wave packets  $\langle -\nabla V_{ij} \rangle$  is easily found by differentiating  $\langle V_{ij} \rangle$  with respect to  $\langle r_{ij} \rangle$ . Differentiating eq. 5.26 for the NN potential with respect

to  $\langle r_{ij} \rangle$ , we get

$$\begin{aligned} \langle -\nabla V_{ij}^N \rangle = V_0 & \left[ \frac{-2\langle r_{ij} \rangle r_o^3}{(r_o^2 + 4\sigma^2)^{5/2}} - \frac{C r_o^2}{4\pi\sigma(r_o^2 + 4\sigma^2)} \frac{1}{\langle r_{ij} \rangle} \exp\left[ \frac{-\langle r_{ij} \rangle^2}{4\sigma^2} \frac{r_o^2}{(r_o^2 + 4\sigma^2)} \right] \right. \\ & \left. + \left[ \frac{2C r_o}{(r_o^2 + 4\sigma^2)^{3/2}} + \frac{1}{\langle r_{ij} \rangle^2} \frac{C r_o}{(r_o^2 + 4\sigma^2)^{1/2}} \right] \operatorname{erf}\left[ \frac{\langle r_{ij} \rangle}{2\sigma} \frac{r_o}{(r_o^2 + 4\sigma^2)^{1/2}} \right] \right] \\ & \times \exp\left[ \frac{-\langle r_{ij} \rangle^2}{(r_o^2 + 4\sigma^2)} \right] \quad (5.30) \end{aligned}$$

Similarly for the Coulomb interaction from eq. 5.29 we get

$$\begin{aligned} \langle -\nabla V_{ij}^C \rangle = 1.44 & \left[ \frac{1}{\langle r_{ij} \rangle^2} \operatorname{erf}\left[ \frac{\langle r_{ij} \rangle}{2\sigma} \right] - \frac{1}{4\pi\sigma} \frac{1}{\langle r_{ij} \rangle} \exp\left[ \frac{-\langle r_{ij} \rangle^2}{4\sigma^2} \right] \right] \quad (\text{MeV}) \\ & \dots\dots (5.31) \end{aligned}$$



### 5.3 RESULTS AND DISCUSSIONS

We consider two different values of  $\sigma$  corresponding to two different values of  $r_N$  (rms radius of a nucleon).

#### 5.3.1 The case of $r_N = 0.8$ fm

First we choose a value of  $\sigma$  such that the rms radius of each nucleon ( $r_N$ ) is equal to the experimental rms charge radius of protons which is approximately equal to 0.8 fm. Since all the wave packets are frozen, the zero-point energy (eq. 5.22) is constant and since we are interested in studying the effect of the finite size of nucleons on the NN potentials, we first neglect this constant term in the calculation of the binding energy in eq. 5.21 and in the determination of the potential parameters. Later in section 5.3.1(c) we include this term also in eq. 5.21 and study its effects on the NN potential and the fusion cross sections.

In chapter 4 we found that the fusion cross sections for the  $^{16}\text{O}+^{16}\text{O}$  and  $^{40}\text{Ca}+^{40}\text{Ca}$  reactions, calculated by considering nucleons as point particles in the classical microscopic approach and with the NN potential given by eq. 5.24, agreed well with the experiments for a value of the range parameter ( $r_0$ ) equal to 1.2 fm (potential P3 and P4 in chapter 4). Therefore, for the present study also we choose the same form of the NN potential and  $r_0 = 1.2$  fm.

We adjust the parameters  $V_0$  and  $C$  such that in the ground

state of  $^{16}\text{O}$  the rms radius given by eq. 5.20 and the binding energy given by eq. 5.21 (with  $\langle T_i \rangle = 0$ ) have values close to the corresponding experimental values for the  $^{16}\text{O}$  nucleus. This set of parameters (called potential  $\langle W1 \rangle$ ) is given in Table 5.1 along with the ground state properties of  $^{16}\text{O}$ .

### (a) Effects Of The Finite Size On :

#### (i) Coulomb and NN potentials

The Coulomb potential between two point like protons eq. (5.25) and its folding potential eq. (5.29) for  $r_N = 0.8$  fm are plotted in Figure 5.1. Comparison of the two potentials shows that they differ significantly from each other only for  $\langle r_{ij} \rangle < 1.60\text{fm}$ .

In Figure 5.2 the NN potential  $v_{ij}^N$  (eq. 5.24) with the parameters  $W1$  and  $\sigma=0$ ) is plotted and compared with the potential  $P3$  of chapter 4. While the potential  $P3$  for point particles is a narrow potential with shallow depth and a large repulsive-core radius, we find that  $v_{ij}^N$  (potential  $W1$ ) in the present calculation (derived for a nucleon size of  $0.8$  fm) is a much deeper potential with a smaller repulsive-core radius and a smaller radius of the minimum.

The effective double folding NN potential  $\langle v_{ij}^N \rangle$  (potential  $\langle W1 \rangle$ ) is also plotted in Figure 5.2 and compared with the potential  $P3$  and  $v_{ij}^N(W1)$ . We notice that the potential  $\langle W1 \rangle$  also has a smaller repulsive-core radius compared to the potential  $P3$ . The tail of the potential  $\langle W1 \rangle$  is longer than the tail of the

TABLE 5.1

Parameters of the effective NN potential and the calculated ground-state properties of  $^{16}\text{O}$

Potential	$\langle W1 \rangle$	$\langle W2 \rangle$	P3	P5	Expt
$r_N(\text{fm})$	0.80	1.40	0.00	0.00	
$r_O(\text{fm})$	1.20	1.20	1.20	1.20	
C (fm)	1.34	0.99	2.35	2.23	
$V_O(\text{MeV})$	590.0	495.0	3360.0	2090.0	
Binding energy (MeV)	-127.6	-127.6	-127.6	-127.6	-127.6
$[\Sigma \langle r_i^2 \rangle]^{1/2}$ (fm)	2.61	2.34	2.73	2.61	
rms radius (fm)	2.73	2.73	2.73	2.61	2.73
K (MeV)	440.0	170.0	995.0	1015.0	

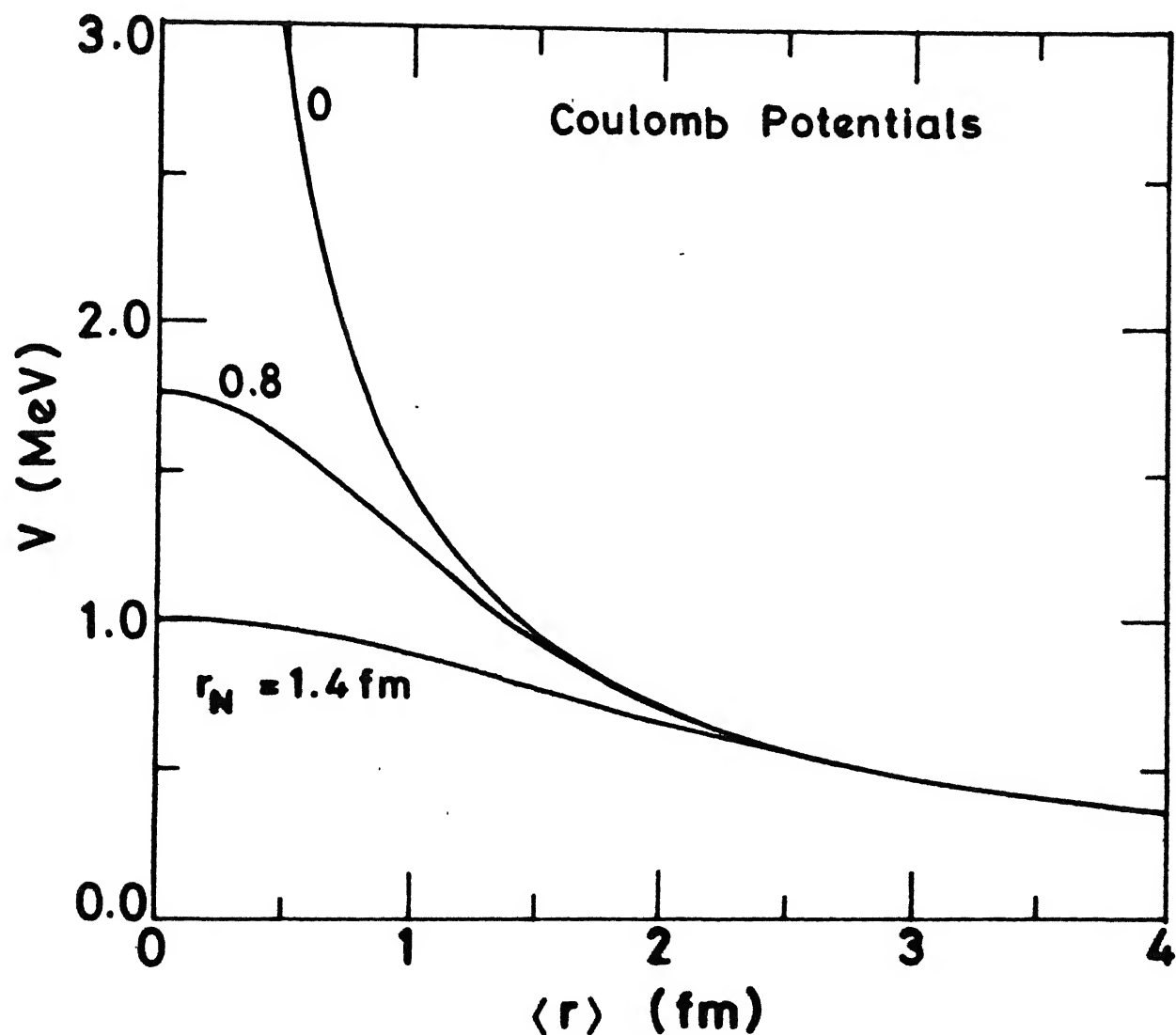


FIGURE 5.1

The effective Coulomb potential (eq. 5.29) for gaussian wave-packets with  $r_N = 0.8$  fm and  $1.4$  fm are compared with the Coulomb potential (eq. 5.25) between two point charges ( $r_N = 0$  fm)

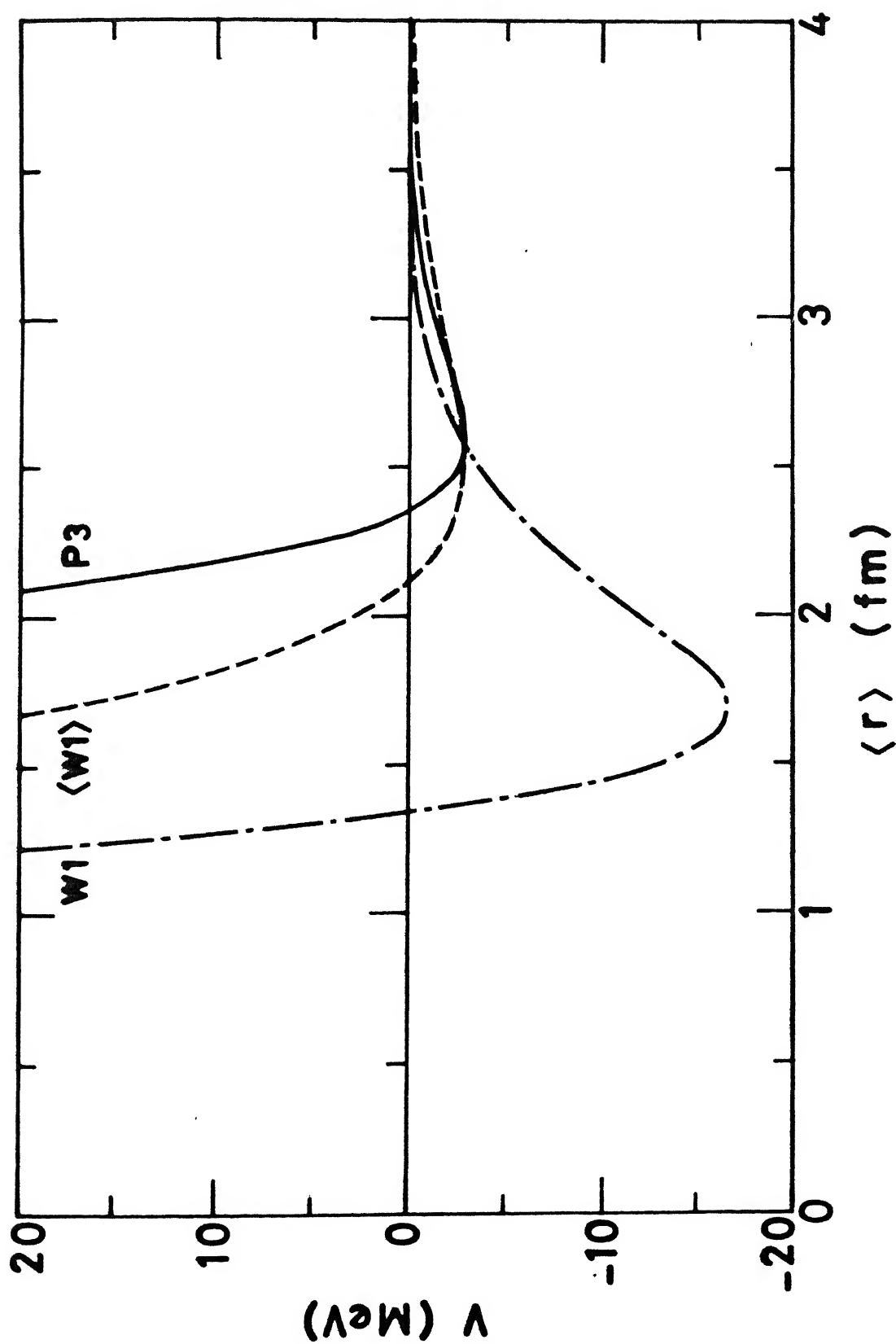


FIGURE 5.2

Comparison of the effective NN potential  $\langle W1 \rangle$  for gaussian wave-packets ( $r_N = 0.8$  fm) to a potential W1 with the same parameters but for point particles ( $r_N = 0$  fm). The potentials  $\langle W1 \rangle$  and W1 are compared with the potential P3 for point particles also.

potential P3 (see Figure 5.3 also). Thus, due to the overlap of the two wave packets, we find that  $\langle W1 \rangle$  is spread out in both the directions, i.e., it has a smaller core and a longer tail, compared to the potential P3 with the same range parameter  $r_0$ .

However, the depth of the potential P3 and  $\langle W1 \rangle$  are nearly equal because both the potentials reproduce approximately the same total potential energy, which in the special case of  $\langle T_i \rangle = 0$  is also the binding energy. The minimum of the potential  $\langle W1 \rangle$  is located at  $\langle r_{ij} \rangle = 2.51$  fm which is less than the  $r_{\min}$  of the potential P3 (2.60 fm). The difference in the positions of the minima of the two potentials (about 0.1 fm) is nearly equal to the difference in the rms radius of  $^{16}\text{O}$  with the potential P3 and the rms radius of the distribution of centroids (corresponding to the second term in eq. 5.20) in  $^{16}\text{O}$  with potential  $\langle W1 \rangle$ .

#### (ii) Nuclear Compressibility Coefficient (K)

We calculate the nuclear compressibility coefficient (K) given by eq. 5.23b. The calculated value of K for  $^{16}\text{O}$  with the potential  $\langle W1 \rangle$  is about 440 MeV (see Table 5.1). Since  $\langle W1 \rangle$  is a wider potential compared to the potential P3, we find that the compressibility coefficient for  $^{16}\text{O}$  with  $\langle W1 \rangle$  is much smaller than the value calculated with the potential P3. This value is close to the value obtained for  $^{16}\text{O}$  in the HF and RPA calculations in Ref. 5.

#### ~~(iii) Nuclear Density Distribution~~

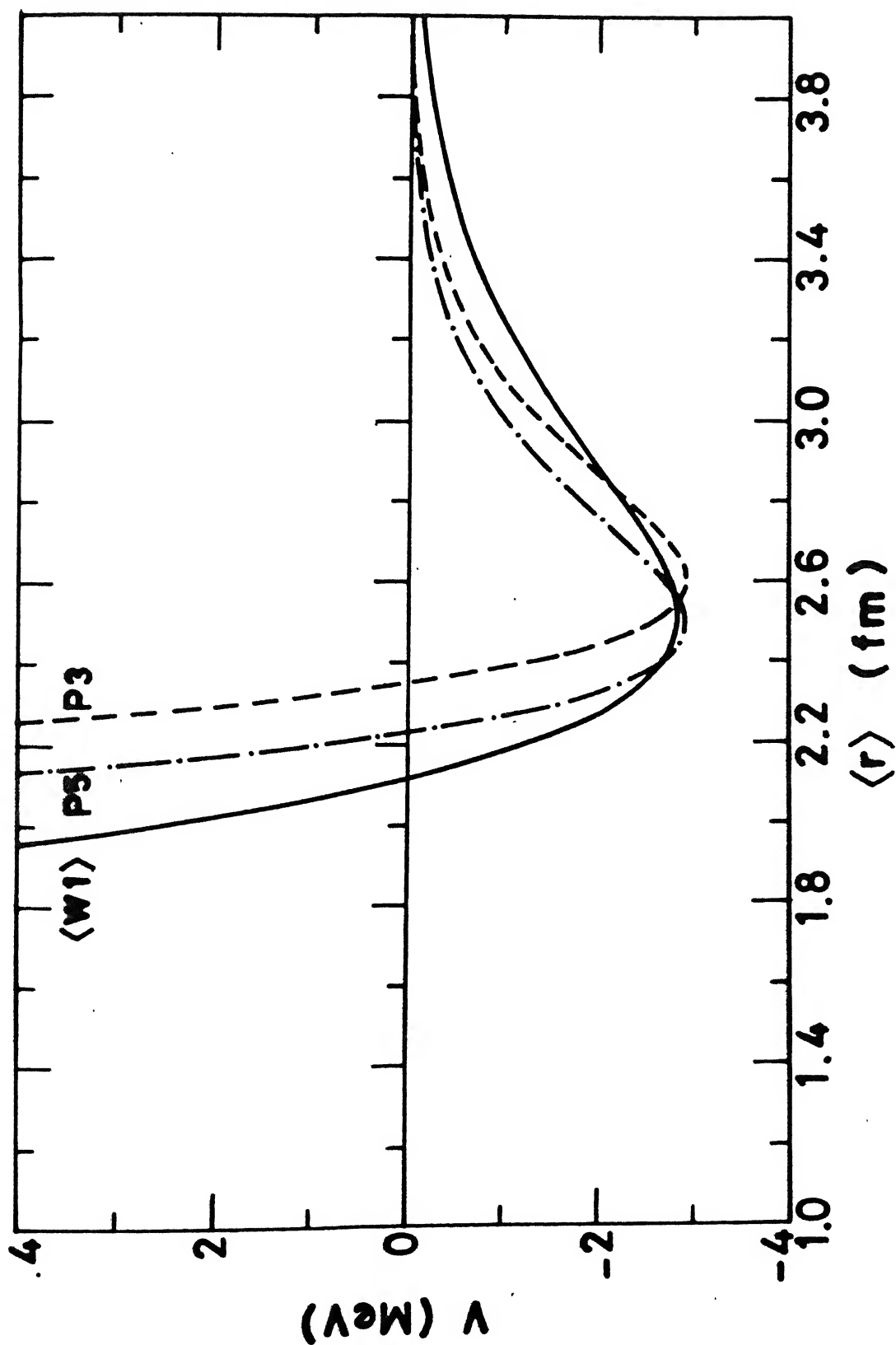


FIGURE 5.3

Comparison of the effective NN potential P3 and P5 for point particles and potential  $\langle W1 \rangle$  for gaussian wave-packets with  $r_N = 0.8$  fm. Parameters of the potentials are given in Table 5.1

### (iii) Nuclear Density Distribution

Due to the finite size of nucleons, the frozen wave packet calculation shows remarkable differences with the point particle calculations in the nuclear density distributions. The average radial density distribution of nucleons  $\rho(r)$  for  $^{16}\text{O}$  with  $r_N = 0.8$  fm and the potential  $\langle W1 \rangle$  is shown in Figure 5.4. For a comparison with the point particle calculations, we show in Figure 5.5a the distribution of point nucleons in  $^{16}\text{O}$  with the potential P3. Whereas the point particle calculation shows a discontinuous density distribution in Figure 5.5a, the density distribution with the frozen wave packet calculation in Figure 5.4 shows a continuous and a nearly smooth density distribution having a distinct surface region with a tail.

Figure 5.5b shows the distribution of centroids in  $^{16}\text{O}$  with the potential  $\langle W1 \rangle$ . This distribution is similar to that shown for the point particle calculation with the potential P3 in Figure 5.5a, but is shifted towards the lower radii because of the smaller rms radius of the distribution of the centroids. The density distribution with the potential  $\langle W1 \rangle$  in the Figure 5.4 has a bump and wiggles on this bump in the region ( $r = 1.6 - 3.4$  fm) where most of the centroids of the wave packets are located. The wiggles indicate that  $r_N = 0.8$  fm is not large enough to generate a smooth density distribution in the present calculations.

A comparison of  $\rho(r)$  in Figure 5.4 with the experimental density distribution<sup>6</sup> for  $^{16}\text{O}$  shows that  $\rho(r)$  in the present



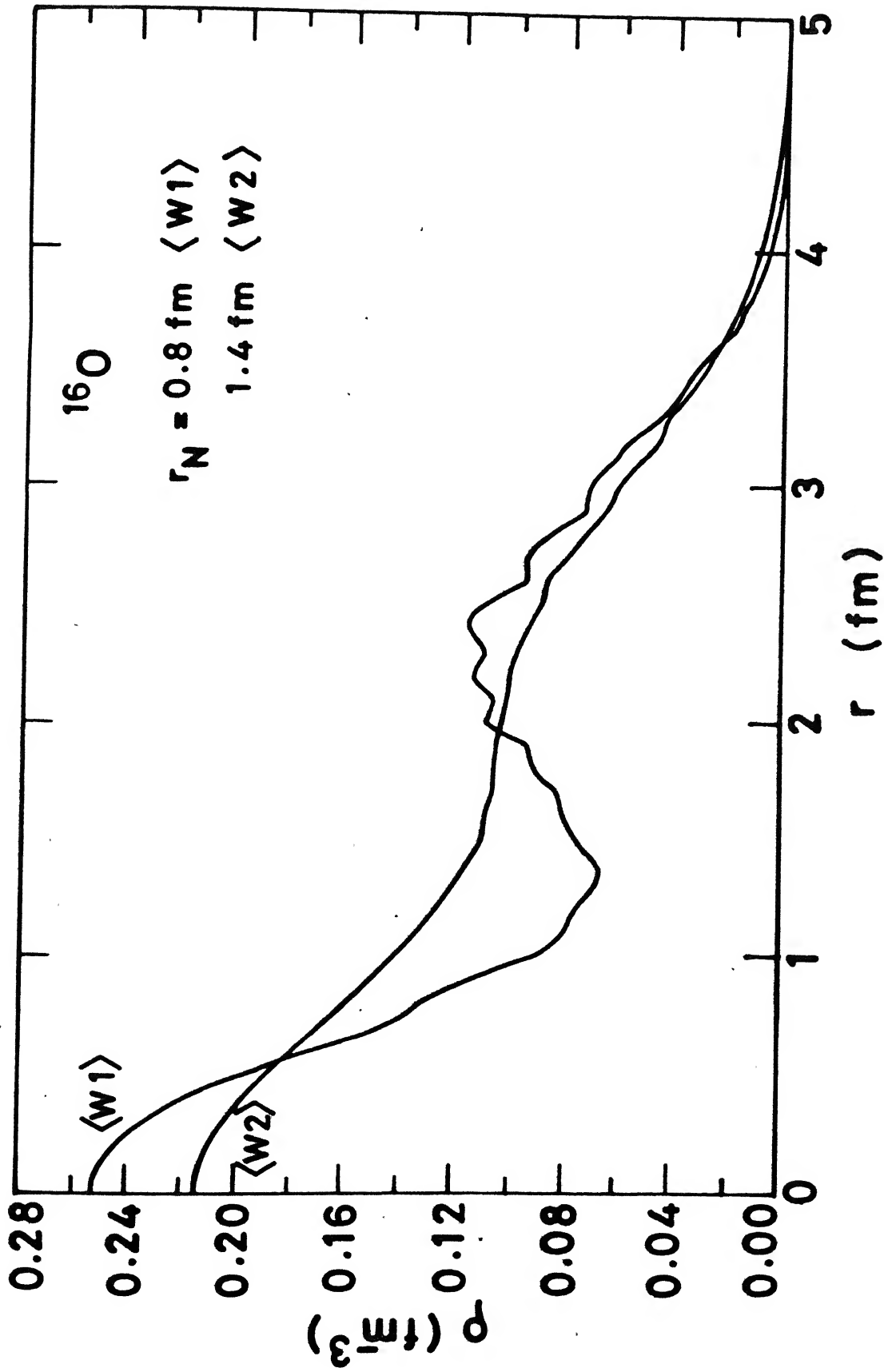


FIGURE 5.4

Calculated radial density distributions  $\rho(r)$  of nucleons in the ground-state of  $^{16}\text{O}$  with the potential  $\langle W1 \rangle$  ( $r_N = 0.8 \text{ fm}$ ) and with the potential  $\langle W2 \rangle$  ( $r_N = 1.4 \text{ fm}$ ).

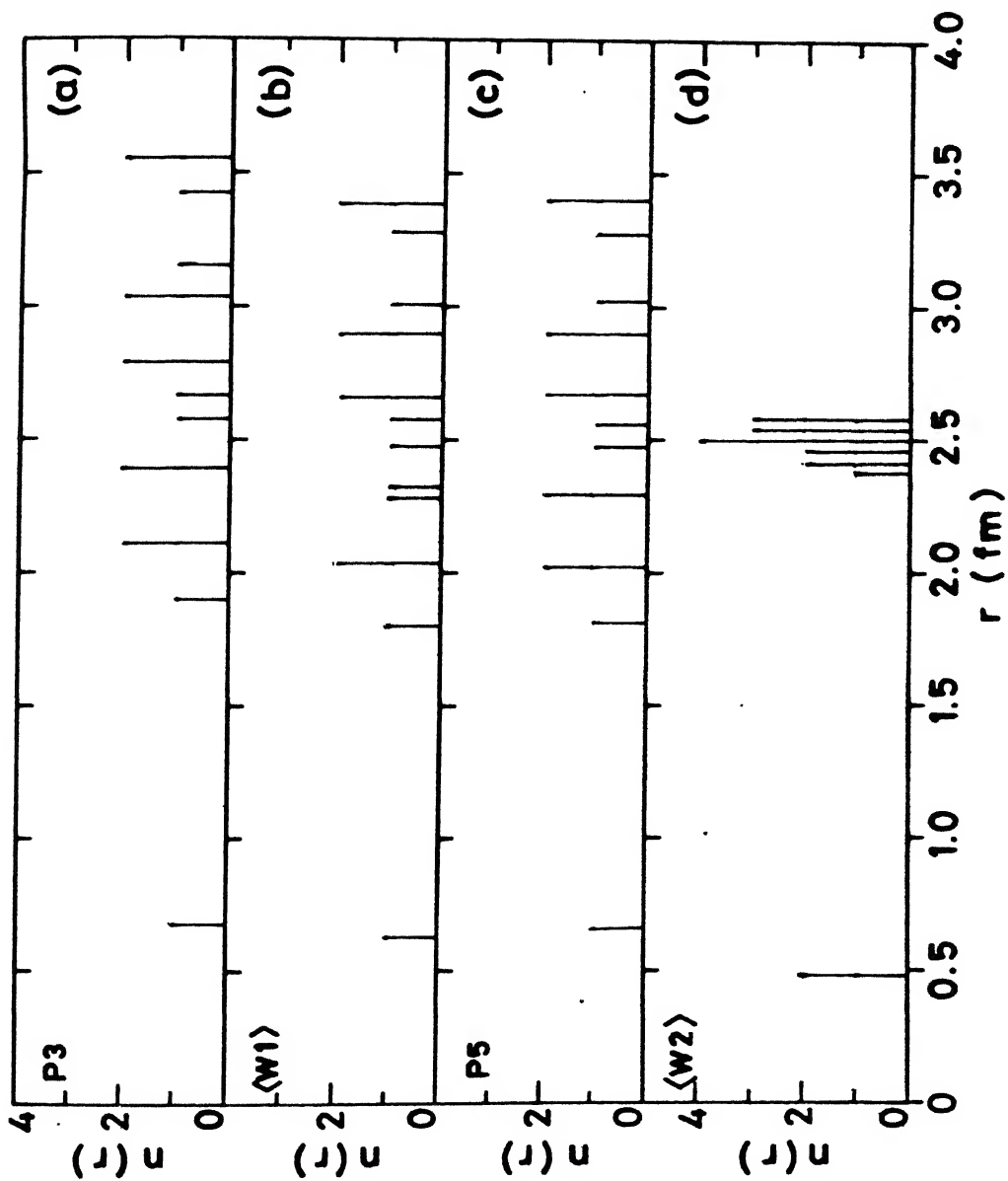


FIGURE 5.5 (a-d)

Radial distribution  $n(r)$  of the position of the point particles or the centroids of the wave-packets in the ground-state of  $^{16}\text{O}$  with the potential: (a) P3 for point nucleons, (b)  $\langle W1 \rangle$  for gaussian wave-packets with  $r_N = 0.8$  fm, (c) P5 for point nucleons; and (d)  $\langle W2 \rangle$

calculation has a large value at very small radial distances. The reason for this higher density at smaller radii is the presence of a single nucleon in the equilibrium position near the centre of the nucleus in the present case (see Figure 5.5b) which contributes excessively to the average density.

#### (iv) Fusion Cross Sections

We calculate the fusion cross section for the  $^{16}\text{O}+^{16}\text{O}$  reaction with the potential  $\langle W1 \rangle$ . Due to the kind of approximations involved, the present calculations are similar to those of chapter 4 with the point particles replaced by the centroids of the frozen wave packets and the NN potential replaced by its double folding integral (eq. 5.26), but the rms radius given by eq. 5.20.

The calculated fusion cross sections for the  $^{16}\text{O}+^{16}\text{O}$  reaction with the potential  $\langle W1 \rangle$  at  $E_{\text{CM}} = 16.7, 32.8$  and  $66.8$  MeV, averaged over 12 initial random orientations, are shown in Figure 5.6 and compared with the point particle calculations with the potential P3. The calculations of Chapter 4 showed that the fusion cross sections for heavy-ion reactions are sensitive to the tail of the NN potentials. Since the potential  $\langle W1 \rangle$  is wider and has a tail which is slightly longer than the tail of the potential P3 (Figure 5.3) we find that fusion cross sections with the potential  $\langle W1 \rangle$  are also slightly higher than the fusion cross sections with the potential P3.

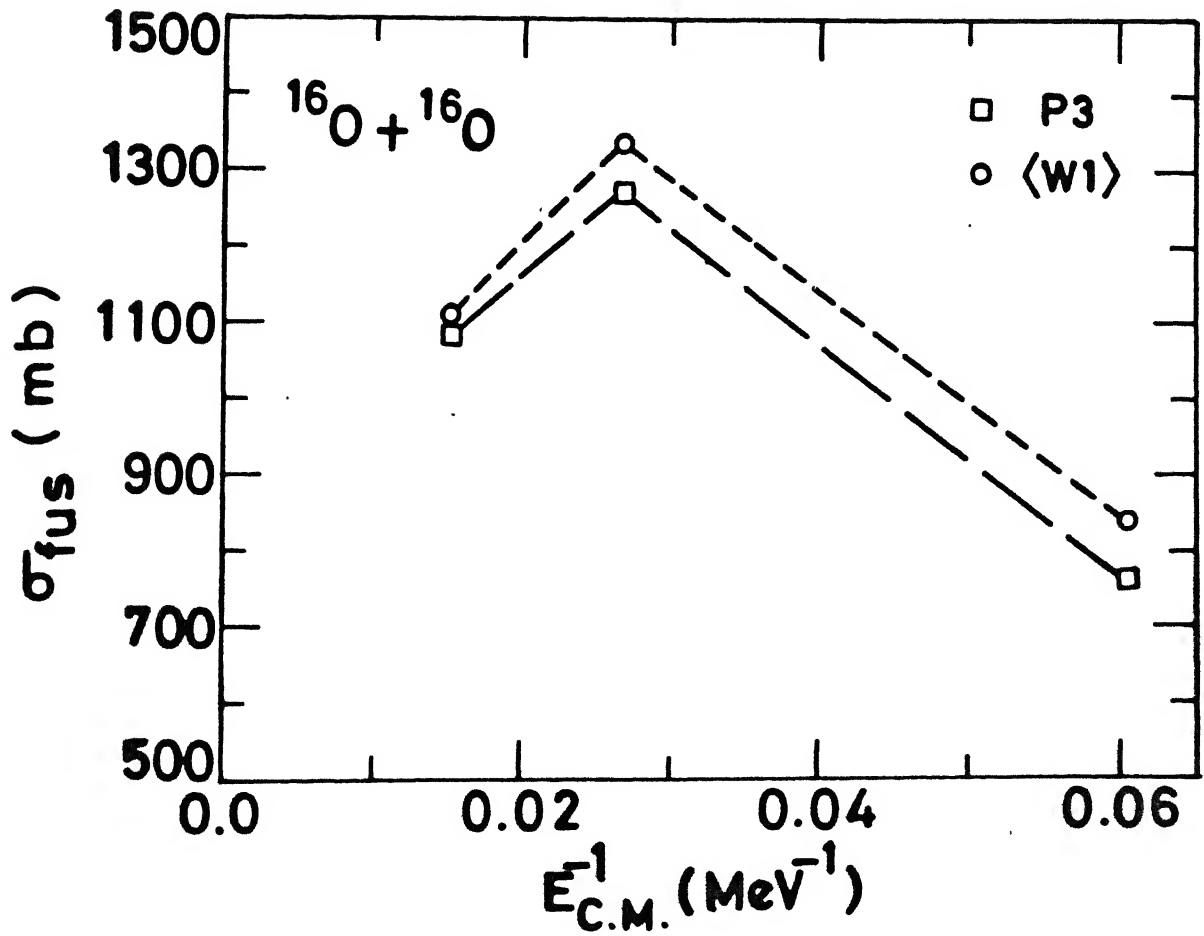


FIGURE 5.6

Comparison of the calculated fusion cross sections for the  $^{16}\text{O} + ^{16}\text{O}$  reaction with the potential P3 and potential <W1> with  $r_N = 0.8$  fm.

### (b) An Equivalent-Radius Point Particle Calculation

In some classical microscopic calculations<sup>7</sup> which treat nucleons as essentially point particles, the parameters of the NN potential are fitted to the rms radius given by eq. 5.20 to account for the finite size of nucleons. No other finite size effect on the NN potential is explicitly considered. Therefore, for the purpose of comparison with such a prescription, we again consider nucleons as point particles. We take the Coulomb potential given by eq. 5.25 and determine the parameters of the NN potential given by eq. 5.24 for  $r_0 = 1.2$  fm, such that the rms radius given by eq. 5.20 and the binding energy of  $^{16}\text{O}$  are close to the experimental values. Parameters of this potential (called potential P5) are given in Table 5.1.

Potential P5 is plotted and compared with the potentials  $\langle W1 \rangle$  and potential P3, in Figure 5.3. Since the rms radius of the distribution of centroids (second term in eq. 5.20) in  $^{16}\text{O}$  with  $\langle W1 \rangle$  and the rms radius of  $^{16}\text{O}$  with the potential P5 are identical (2.61 fm), we find that the two potentials have nearly identical positions of minima and nearly the same depths. However, the potentials P3 and P5 also have larger repulsive-cores compared to that for  $\langle W1 \rangle$ . The potential  $\langle W1 \rangle$  is also wider compared to both the potentials P3 and P5.

The calculated compressibility (K) for  $^{16}\text{O}$  with the potential P5 is about 1015 MeV which is much larger than the corresponding value for  $\langle W1 \rangle$ ; and it is nearly equal to that for the potential

P3. The distribution of nucleons in  $^{16}\text{O}$  with P5 is shown in the Figure 5.5c which is similar to that with the potential  $\langle W1 \rangle$  in the Figure 5.5b and is shifted inwards compared to the distribution in the Figure 5.5a for P3.

The calculated fusion cross section for the  $^{16}\text{O}+^{16}\text{O}$  reaction with the potential P5 at  $E_{\text{CM}} = 16.7$  MeV is compared with the other results at the same energy in Table 5.2. Since the rms radius of the distribution of nucleons (with  $r_N = 0$  in eq. 5.20) in  $^{16}\text{O}$  with the potential P5 is less than the rms radius of  $^{16}\text{O}$  with the potential P3, we find that the value of the fusion cross section with P5 is also smaller compared to that with P3 and with  $\langle W1 \rangle$ .

Thus, from the above discussion we observe that the main effect of the finite extension of the nucleons on the NN potential is the smaller core radius and an increased width of the potential.

### (c) Inclusion Of Zero-Point Energy

For the  $r_N = 0.8$  fm case, we now include the zero-point kinetic energy  $\langle T_1 \rangle$  given by eq. 5.22 in the binding energy (eq. 5.21). Since all the wave packets are frozen, all the  $\alpha$ 's are constant. Therefore,  $\langle T_1 \rangle$  is constant and inclusion of this constant term in eq. 5.21 represents merely a re-scaling of the total potential energy. Therefore, the rms radius of the distribution does not change and only  $V_0$  in eq 5.26 is readjusted to give the correct binding energy. This new set of parameters

TABLE 5.2

Fusion cross sections for the  $^{16}\text{O}+^{16}\text{O}$  reaction at  $E_{\text{CM}} = 16.7$  MeV with different potentials.

Potentials	$\sigma_{\text{fus}}$ (mb)
<W2+>	1327
<W1+>	1130
<W2>	1106
<W1>	838
P3	764
P5	680

(denoted by the potential  $\langle W1+\rangle$ ) is given in Table 5.3.

The potential  $\langle W1+\rangle$  is plotted and compared with  $\langle W1\rangle$  in the Figure 5.7. The zero-point energy  $\langle T_i \rangle$  corresponding to  $r_N = 0.8$  fm has a rather large value (72.8 MeV). To compensate for this large positive term in eq. 5.21, the potential  $\langle W1+\rangle$  has a very large depth ( $V_{\min} = -26.6$  MeV) compared to the depth of  $\langle W1\rangle$  ( $V_{\min} = -2.8$  MeV), though the minima of the two potentials are located at the same separation  $\langle r_{ij} \rangle$ . At large values of  $\langle r_{ij} \rangle$ , the potential  $\langle W1+\rangle$  has a strongly attractive tail compared to the tail of  $\langle W1\rangle$ . Since the effect of the repulsive (positive) zero-point kinetic energy term is included only in the binding energy and thus in the potential, this repulsive term does not appear in the dynamics in the present calculations. Therefore, due to the strong attractive long tail of  $\langle W1+\rangle$ , we find that the calculated fusion cross section for the  $^{16}\text{O}+^{16}\text{O}$  reaction at  $E_{\text{CM}} = 16.7$  MeV with  $\langle W1+\rangle$  has a very large value compared to that with the potential  $\langle W1\rangle$  (see Table 5.2). A proper inclusion of this repulsive  $\langle T_i \rangle$  term is discussed in chapter 6.



TABLE 5.3

The ground-state properties of  $^{16}\text{O}$  and the parameters of the effective NN potentials  $\langle W1 \rangle$  and  $\langle W2 \rangle$  modified to include zero-point kinetic energy in the binding energy.

Potential	$\langle W1 \rangle$	$\langle W2 \rangle$	Expt
$r_N$ (fm)	0.80	1.40	
$r_O$ (fm)	1.20	1.20	
C (fm)	1.34	0.99	
$V_O$ (MeV)	5520.0	1840.0	
$\langle T \rangle / A$ (MeV)	72.8	23.8	
Binding energy (MeV)	-127.6	-127.6	-127.6
$[\Sigma \langle r_i^2 \rangle]^{1/2}$ (fm)	2.61	2.34	
rms radius			
$\langle r^2 \rangle^{1/2}$ (fm)	2.73	2.73	2.73

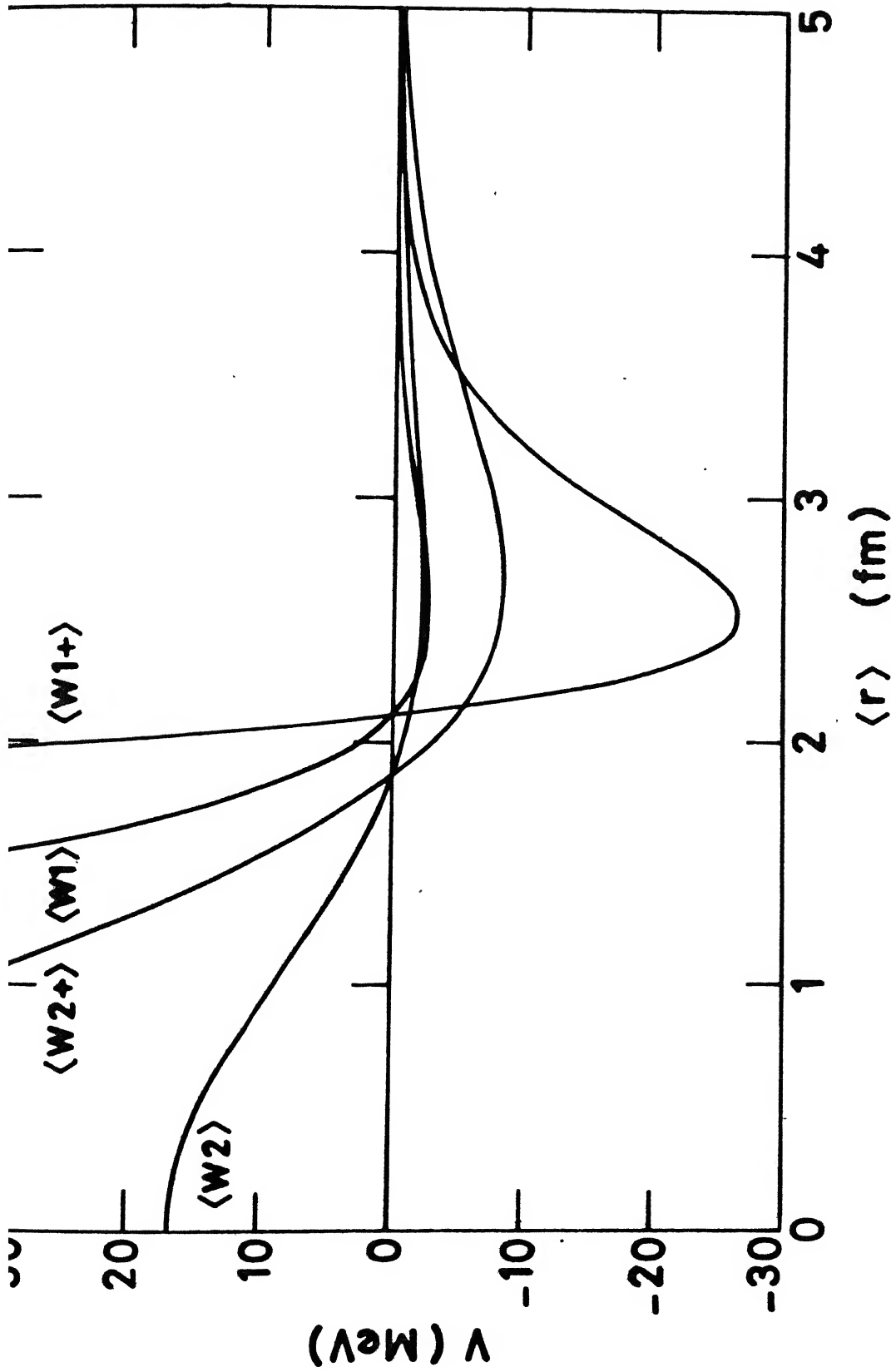


FIGURE 5.7

Comparison of the effective NN potentials  $\langle W1 \rangle$  and  $\langle W2 \rangle$  for the gaussian wave-packets with  $r_N = 0.8$  fm and 1.4 fm, respectively, and the corresponding potentials  $\langle W1+ \rangle$  and  $\langle W2+ \rangle$  with the inclusion of the corresponding constant zero-point energies.

### 5.3.2 The Case Of $r_N = 1.4$ fm

Since the zero-point energy  $\langle T_i \rangle$  for  $r_N = 0.8$  fm has a very large value (72.8 MeV), we now consider a value of  $r_N$  such that  $\langle T_i \rangle$  is of the correct order of magnitude.<sup>8</sup> Therefore, we choose  $r_N = 1.4$  fm for which  $\langle T_i \rangle = 23.8$  MeV.

Firstly, we again neglect  $\langle T_i \rangle$  in eq. 5.21 to study the effects of the increased size of the wave packets. With  $r_N = 1.4$  fm and  $r_O = 1.2$  fm we adjust the parameters  $V_O$  and  $C$  such that the calculated rms radius (eq. 5.20) and the binding energy (eq. 5.21) of the ground state of  $^{16}\text{O}$  are close to the experimental values. This set of parameters (called potential  $\langle W2 \rangle$ ) is given in Table 5.1.

#### (a) Effects Of The Finite Size On :

##### (i) Coulomb and NN Potentials

The Coulomb potential (eq. 5.29) for  $r_N = 1.4$  fm is plotted in Figure 5.1 and compared with the Coulomb potential between point charges (eq. 5.25). This potential is also compared with the Coulomb potential for  $r_N = 0.8$  fm., in Figure 5.1. The Coulomb potential for  $r_N = 1.4$  fm differs significantly from the point charge Coulomb potential for  $\langle r_{ij} \rangle < 3.0$  fm.

The potential  $\langle W2 \rangle$  is plotted and compared with the potential  $\langle W1 \rangle$  in Figures 5.7 and 5.8. The potential  $\langle W2 \rangle$  has an even smaller radius of the core compared to the potential  $\langle W1 \rangle$ , and due

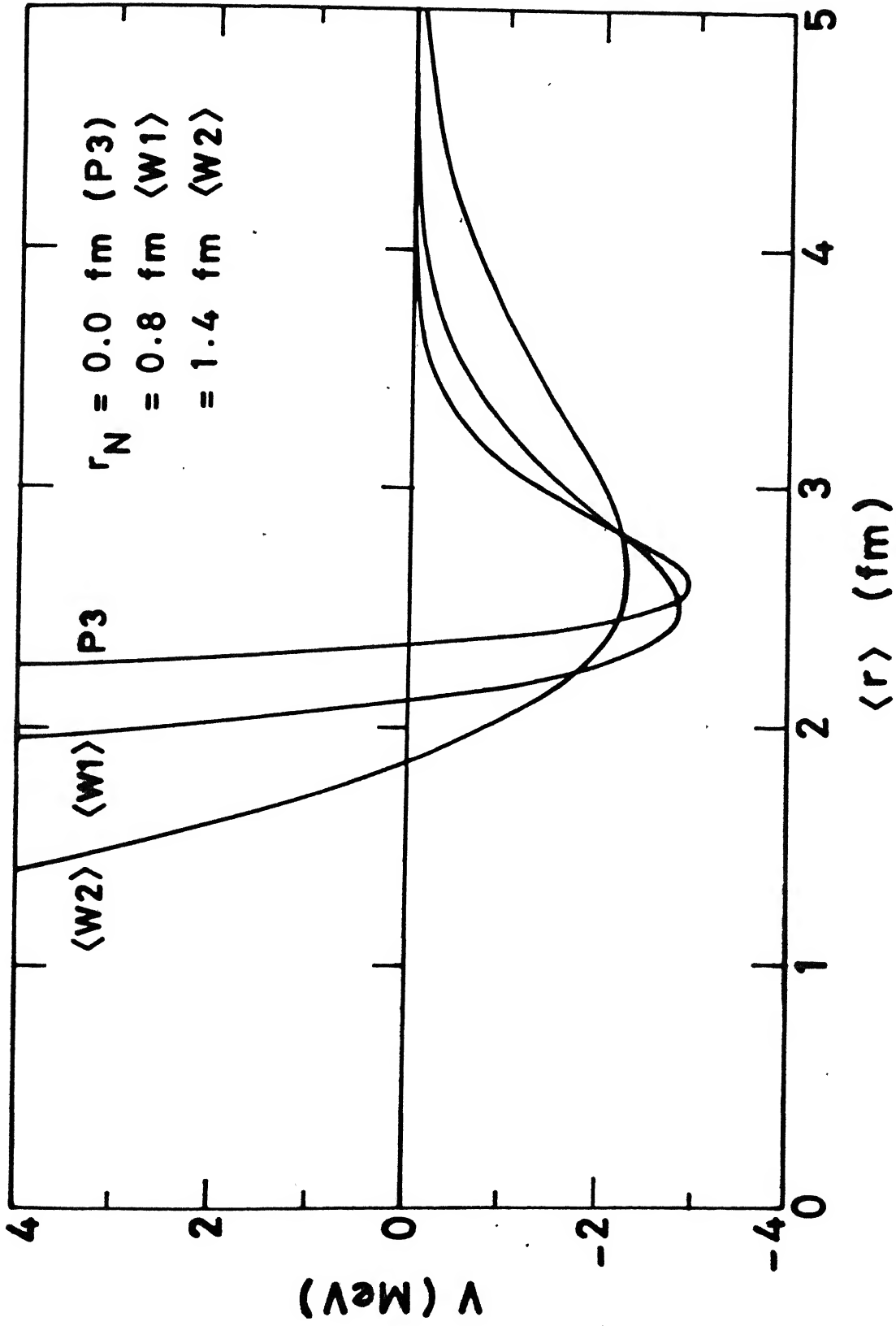


FIGURE 5.8

Plots of the potentials P3 for point particles and the potentials  $\langle W1 \rangle$  and  $\langle W2 \rangle$  for the gaussian wave-packets with  $r_N = 0.8 \text{ fm}$  and  $1.4 \text{ fm}$ , respectively.

to the increased size of the nucleons it is spread over much more than the potential  $\langle W1 \rangle$ . Thus a comparison of the potentials  $P3$ ,  $\langle W1 \rangle$ , and  $\langle W2 \rangle$  (i.e., for  $r_N = 0.0, 0.8$  and  $1.4$  fm respectively) in Figure 5.8 shows that, as  $r_N$  is increased, the corresponding potentials become wider with a smaller core radius and an extended tail.

The  $\sigma = 0$  potential corresponding to the potential  $\langle W2 \rangle$  (called the potential  $W2$ ) is shown in Figure 5.9 and compared with the potential  $W1$ . The potential  $W2$  is much deeper than the potential  $W1$  and has a smaller radius of the core.

#### (ii) Nuclear Compressibility Coefficient ( $K$ )

The calculated value of the compressibility coefficient ( $K$ ) for  $^{16}\text{O}$  with the potential  $\langle W2 \rangle$  is about 170 MeV, which is less than the corresponding value for  $^{16}\text{O}$  with the potential  $\langle W1 \rangle$ .

#### (iii) Nuclear Density Distribution

The average density distribution  $\rho(r)$  (eq. 5.17) for  $^{16}\text{O}$  with  $r_N = 1.4$  fm and potential  $\langle W2 \rangle$  is also shown in Figure 5.4. We notice from this Figure that due to the increased spreading of the wave packets this density distribution is smoother than the distribution with the potential  $\langle W1 \rangle$  and  $r_N = 0.8$  fm. The distribution of centroids of the wave packets in  $^{16}\text{O}$  with  $\langle W2 \rangle$  is shown in Figure 5.5d. From Figures 5.5(a-d) we note that with the higher value of  $\sigma$  (or  $r_N$ ), most of the centroids are located inside

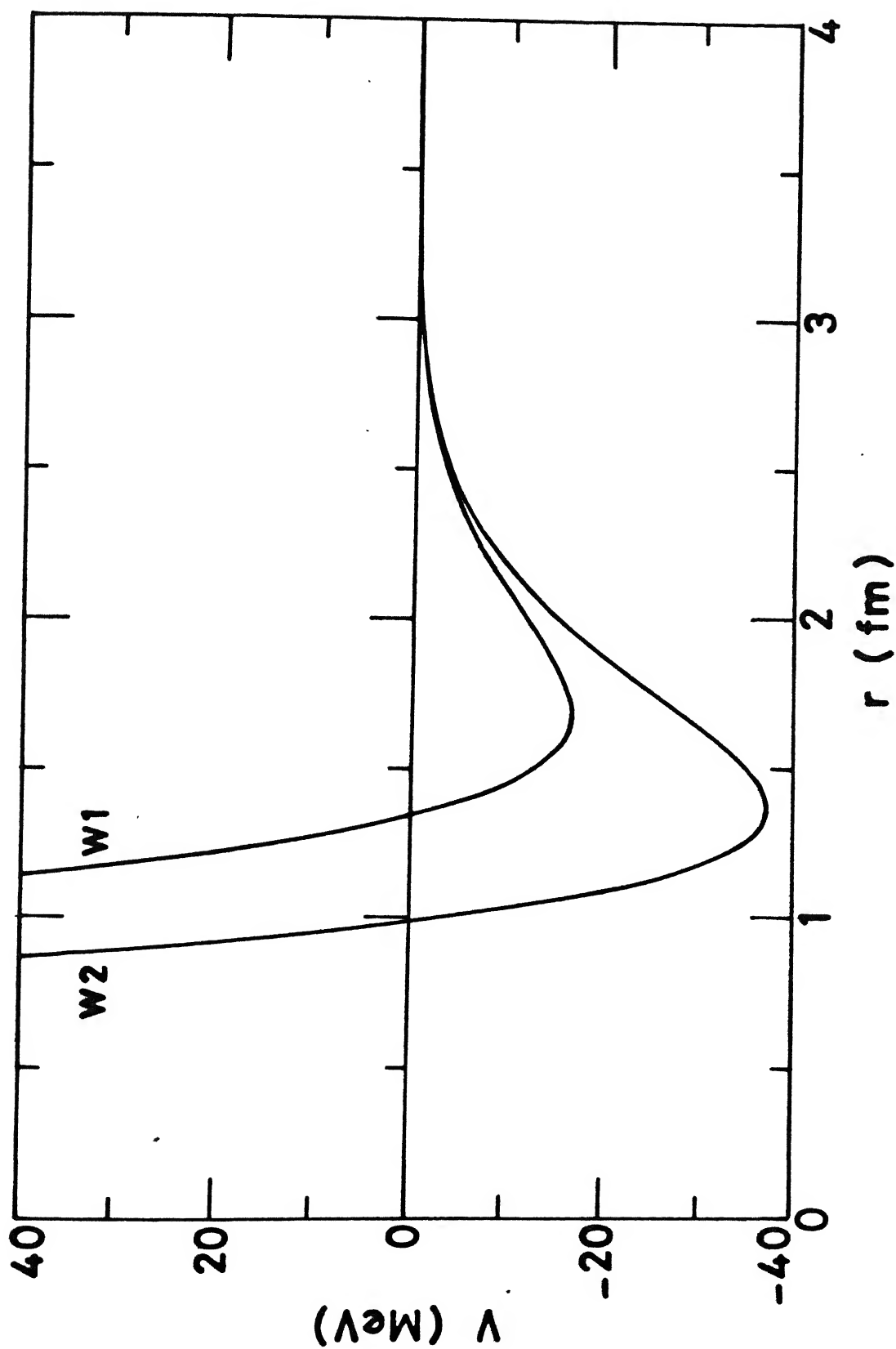


FIGURE 5.9

Plot of the potentials W1 and W2 with the parameters of the respective potentials  $\langle W1 \rangle$  and  $\langle W2 \rangle$  but for the case of  $\sigma = 0$ .

a thin spherical shell on the surface. The tail of the density distribution, or the spreading of the nuclear matter in this case is brought about by the spreading of the wave packets, whereas for the smaller value of  $\sigma$  or for the point particle case the spreading at the surface is accomplished by the distribution of the particles itself.

#### (iv) Fusion Cross Sections

The fusion cross section for the  $^{16}\text{O}+^{16}\text{O}$  reaction at  $E_{\text{CM}} = 16.7$  MeV with the potential  $\langle W2 \rangle$  is given in the Table 5.2. A comparison with the other results in Table 5.2 shows that it is higher than the fusion cross section with the potential  $\langle W1 \rangle$ , and it is very high compared to the calculated value with the potential P3 as well as compared to the experimental data. Though, the rms radius of the distribution of the centroids in  $^{16}\text{O}$  with the potential  $\langle W2 \rangle$  is 2.34 fm, which is less than that with the potential  $\langle W1 \rangle$  (2.61 fm), this high value of the fusion cross section is clearly due to the very long attractive tail of the potential  $\langle W2 \rangle$  (see Figure 5.8) which is much longer than the tail of the potentials  $\langle W1 \rangle$  and P3.

### (b) Inclusion Of The Zero-Point Energy

As in the case of  $r_N = 0.8$  fm, we include the zero-point energy  $\langle T_i \rangle$  in the binding energy (eq. 5.21) in the present case also. The parameters of the potential  $\langle W2+ \rangle$ , with the inclusion of  $\langle T_i \rangle$  in eq. 5.21, are given in Table 5.3. The potential  $\langle W2+ \rangle$  is compared with the potential  $\langle W2 \rangle$  and  $\langle W1+ \rangle$  in Figure 5.7. The potential  $\langle W2+ \rangle$  is deeper than the potential  $\langle W2 \rangle$ , like the potential  $\langle W1+ \rangle$  which is deeper than the potential  $\langle W1 \rangle$ , but since  $\langle T_i \rangle$  for  $r_N = 1.4$  fm is less than the zero-point energy for  $r_N = 0.8$  fm (see Table 5.2), we find that  $\langle W2+ \rangle$  is less deep than the potential  $\langle W1+ \rangle$  near the minimum. The two potentials, however, cross over again due to the increased spreading in  $\langle W2+ \rangle$  for  $r_N = 1.4$  fm and thus the tail of the potential  $\langle W2+ \rangle$  is longer than the tail of  $\langle W1+ \rangle$ . Therefore, the fusion cross section for the  $^{16}\text{O} + ^{16}\text{O}$  reaction at  $E_{\text{CM}} = 16.7$  MeV with the potential  $\langle W2+ \rangle$  given in Table 5.2 is higher than the corresponding fusion cross section with the potential  $\langle W1+ \rangle$ .



#### 5.4 SUMMARY AND CONCLUSIONS

In the study presented above we replaced point nucleons by the frozen gaussian wave packets in order to account for the finite size of nucleons in the nucleus. We studied the effect of the finite size of nucleons on the NN potential, nuclear compressibility, nuclear density distribution, and fusion cross sections by choosing two different values of the width of the gaussian wave packets, corresponding to the rms radius of a nucleon equal to 0.8 fm and 1.4 fm respectively.

In chapter 4 we found that with the point nucleon calculations the NN potential that reproduced the ground state properties of nuclei correctly had a very large repulsive core radius; and to reproduce the heavy-ion fusion cross sections also, it was necessary to choose a smaller value of the range parameter ( $r_0$ ). This resulted in a short range, narrow potential with a very high compressibility coefficient (about 1000 MeV). In the present calculations, however, we find that with an increase in the size of the wave packets, the NN potential which reproduces the ground state properties of a nucleus has smaller repulsive core radius and the width also increases, which results in a smaller value of the compressibility coefficient ( $K$ ). However, due to the long tail and the increased attraction between the colliding nuclei, the calculated fusion cross sections are enhanced.

With point particles the nuclear density distribution is discontinuous with peaks occurring at the sites of the nucleons.

However, with the increasing width of the wave packets in the present calculations, we find that the density distribution becomes smoother. For  $r_N = 1.4$  fm, we find that in the ground state of  $^{16}\text{O}$  nucleus most of the centroids of the wave packets are located inside a thin spherical shell on the surface which is reminiscent of the shell structure of the nuclei. We also find that  $r_N = 0.8$  fm, which is equal to the experimental rms radius of protons, is rather small for the present calculations which results in some fluctuations in the density and a very high value of the zero-point kinetic energy (73 MeV).

The present calculations demonstrate that, as compared to a point particle description, the use of wave packets gives a better description of a <sup>nucleus</sup> nucleus and the NN potential. However, with the frozen width approximation for the wave packets in the present calculations, inclusion of the zero-point kinetic energy in the binding energy calculations makes the NN potential even deeper with an even longer attractive tail. Since this repulsive energy term is constant ( because of the frozen constant width ), the increased attraction in the NN potential only enhances the heavy-ion fusion cross sections still further. In the next chapter we propose a semi-classical wave packet approach which attempts to remove some of the assumptions made in this chapter.

## REFERENCES

- 1 C.W. Jager, H. De Vries, and C. De vries, Atomic Data and Nucl. Data Tables **14**, 479 (1974)
- 2 L.I. Schiff, *Quantum Mechanics*, (McGraw-Hill, 1955).
- 3 A. Messiah, *Quantum Mechanics*, Vol. I (John Wiley & sons, 1966).
- 4 P. Ring and P. Schuck, *The Nuclear Many-Body Problem*, (Springer-Verlag, 1980)
- 5 J.P. Blaizot, D. Gogny, and B. Grammaticos, Nucl. Phys. **A265**, 315 (1976).
- 6 A. de Shalit and H. Feshbach, *Theoretical Nuclear Physics*, Vol. I (John Wiley and sons, 1974).
- 7 C.N. Panos and G.S. Anagnostatos, J. Phy. **G 8**, 1651 (1982);  
G.S. Anagostatos C.N. Panos, Phy. Rev. **C26**, 260 (1982).
- 8 J.M. Wilcox and B.J. Moyer, Phys. Rev. **99**, 875 (1955).

## CHAPTER 6

## SEMICLASSICAL MICROSCOPIC APPROACH WITH GAUSSIAN WAVE PACKETS

## 6.1 INTRODUCTION

It was noted in earlier chapters that due to the problem of premature evaporation of nucleons from the nuclei, it is difficult to explicitly introduce the zero-point kinetic energy of the motion of nucleons in nuclei in the classical microscopic approach. By replacing the "frozen" gaussian wave packets for the classical point nucleons, the zero-point energy was incorporated in the total energy in calculations presented in chapter 5 sections 5.3.1(c) and 5.3.2 (b). However, since the wave packets were assumed to be "frozen" i.e. the width of the wave packets remained constant, the zero-point energy presented a constant term in the total energy which modified the effective NN potential. As it is a constant term, it does not appear in the dynamics of the "frozen" wave packets. Further, the widths of the wave packets were chosen with a given value which was assumed to be the same for all the nucleons in a finite nucleus.

Therefore, in the present chapter we remove the above constraint of the same constant value for the widths of the wave packets and develop a semi-classical microscopic approach which also explicitly incorporates the effects of the Fermi gas kinetic energy or "Pauli-repulsion"<sup>1</sup> in the dynamics of the gaussian

wave-packets. The details of the approach to find the static ground-state configuration and the dynamic evolution of a many-body gaussian wave-packet system are given in section 6.2. As an example we study the dynamic evolution of a simple two wave-packet system for some given initial conditions in section 6.3.1. In section 6.3.2 we find the ground state configuration of  $^{16}\text{O}$ . Finally, the conclusions are given in section 6.4.

## 6.2 CALCULATIONAL DETAILS

### 6.2.1 Nucleon Wave Packets

We assume that each nucleon in a nucleus is described by the minimum uncertainty single-particle wave functions, which are normalized 3-dimensional gaussian wave packets.<sup>2</sup>

A general 3-dimensional wave packet is given by

$$\phi_i(x_i, y_i, z_i) = \phi_i(x_i) \phi_i(y_i) \phi_i(z_i) \quad (6.1)$$

where,

$$\phi_i(x_i) = \frac{1}{(2\pi\sigma_{x_i}^2)^{1/4}} \exp\left[ -\frac{(x_i - \langle x_i \rangle)^2}{4\sigma_{x_i}^2} + \frac{i}{\hbar} \langle p_{x_i} \rangle (x_i - \langle x_i \rangle) \right] \quad \dots (6.2)$$

and similarly for  $\phi_i(y_i)$  and  $\phi_i(z_i)$ .<sup>2</sup> For the sake of simplicity, as in chapter 5, we choose spherically symmetric gaussian wave-packets with

$$\sigma_x = \sigma_y = \sigma_z = \sigma \quad (6.3)$$

and

$$\phi_1(\vec{r}_1) = \frac{1}{(2\pi\sigma_1^2)^{3/4}} \exp \left[ \frac{-(\vec{r}_1 - \langle \vec{r}_1 \rangle)^2}{4\sigma_1^2} + \frac{i}{\hbar} \langle \vec{p}_1 \rangle (\vec{r}_1 - \langle \vec{r}_1 \rangle) \right] \quad \dots(6.4)$$

The properties of the gaussian wave-packets (eq. 6.4), described in chapter 5, are again listed below.

$$1. \quad \int \phi_1^* \phi_1 \, dx \, dy \, dz = 1 \quad (6.5a)$$

$$2. \quad \langle \vec{r}_1 \rangle = \int \phi_1^*(r_1) \vec{r}_1 \phi_1(r_1) \, d^3r_1 \quad (6.5b)$$

$$3. \quad \langle \vec{p}_1 \rangle = \int \phi_1^*(r_1) (-i\hbar \vec{\nabla}_1) \phi_1(r_1) \, d^3r_1 \quad (6.5c)$$

$$4. \quad \langle r_1^2 \rangle = \langle r_1 \rangle^2 + 3\sigma_1^2 \quad (6.5d)$$

$$5. \quad \langle p_1^2 \rangle = \langle p_1 \rangle^2 + \frac{3}{4} \frac{\hbar^2}{\sigma_1^2} \quad (6.5e)$$

$$6. \quad (\Delta r_1)^2 = \langle r_1^2 \rangle - \langle r_1 \rangle^2. \text{ and} \quad (6.5f)$$

$$(\Delta p_1)^2 = \langle p_1^2 \rangle - \langle p_1 \rangle^2, \quad \text{with}$$

$$(\Delta r_1)^2 \cdot (\Delta p_1)^2 = \frac{9}{4} \hbar^2 \quad \text{and}$$

$$(\Delta x_i)^2 \cdot (\Delta p_{x_i})^2 = \frac{\hbar^2}{4} \quad \text{etc.}$$

$$\begin{aligned}
 7. \quad \rho_1(r) &= |\phi_1(r)|^2 \\
 &= \frac{1}{(2\pi\sigma_1^2)^{3/2}} \exp \left[ -\frac{(r_1 - \langle r_1 \rangle)^2}{2\sigma_1^2} \right] \quad (6.5g)
 \end{aligned}$$

### 6.2.2 Many Particle Nuclear Wave-Function and Nuclear Hamiltonian

The many-body nuclear Hamiltonian is given by

$$H = \sum_i \frac{-\hbar^2}{2m} \nabla_i^2 + \sum_i \sum_{j>i} v_{ij} (r_i - r_j) \quad (6.6)$$

Since nucleons are fermions, the A-particle nuclear wave-function is antisymmetric with respect to the exchange of particles. However, in the present approach we assume that the A-particle wave function  $\psi$  is the product wave function of the A single-particle wave functions given by eq. 6.4, i.e.

$$\psi = \prod_{i=1}^A \phi_i \quad (6.7)$$

The important effect of the exclusion principle is included in the present approach as described later. However, at this stage we assume the Hartree-ansatz (eq. 6.7) and find the expectation value of the Hamiltonian (eq. 6.6), which is given by

$$\langle H \rangle = \sum_i \left\langle \frac{-\hbar^2}{2m} \nabla_i^2 \right\rangle + \sum_i \sum_{j>i} \langle v_{ij}(r_i - r_j) \rangle \quad (6.8)$$

where

$$\langle v_{ij}(r_i - r_j) \rangle = \iint \phi_i^*(r_i) \phi_j^*(r_j) v_{ij}(r_i - r_j) \phi_i(r_i) \phi_j(r_j) d^3 r_i d^3 r_j \quad (6.9)$$

and  $\langle P_i^2 \rangle$  is given by eq. 6.5e. Therefore, we get

$$\langle H \rangle = \left[ \sum_i \frac{\langle P_i \rangle^2}{2m} + \frac{3}{4} \frac{\hbar^2}{2m} \frac{1}{\sigma_i^2} \right] + \sum_i \sum_{j>i} \langle v_{ij} \rangle \quad (6.10)$$

The first term on the right hand side of eq. 6.10 is the total kinetic energy of motion of the centroids of the wave packets. The second term gives the quantum mechanical part of the total kinetic energy, and the third term is the total potential energy. The nuclear density  $\rho(r)$  is given by

$$\rho(r) = \sum_i \frac{1}{(2\pi\sigma_i^2)^{3/2}} \exp \left[ -\frac{(r - \langle r_i \rangle)^2}{2\sigma_i^2} \right] \quad (6.11)$$



### 6.2.3 Determination of $\sigma$

The expression 6.10 is the same expression as that used in chapter 5 to calculate the total energy. However, in chapter 5 it was assumed that all the  $\sigma_i$  remain constant and moreover specific values of  $\sigma_i$  were chosen which were the same for all the nucleons. At this stage in the present approach we now remove these assumptions for  $\sigma_i$  in eq. 6.10 and determine the width  $\sigma_i$  of each wave packet from the following considerations.

The second term on the right hand side of the expression for  $\langle H \rangle$  (eq. 6.10) is the quantum mechanical part of the total energy. In the ground state of a nucleus we assume that  $\langle P_i \rangle = 0$ , that is, the centroids of the wave packets are stationary. Therefore, the total kinetic energy in the ground state is equal to the quantum mechanical zero-point energy,

$$T_{QM} = \sum_i \frac{3}{4} \frac{\hbar^2}{2m} \frac{1}{\sigma_i^2} \quad (6.12)$$

The average kinetic energy per nucleon ( $\langle T \rangle / A$ ) in the ground state of a degenerate Fermi-gas is given by<sup>1</sup>

$$\langle T \rangle / A = \frac{3}{5} \frac{\hbar^2}{2m} \left[ \frac{3\pi^2}{2} \right]^{2/3} \rho^{2/3} \quad (6.13)$$

where  $\rho$  is the constant density of the nuclear matter. To account for the inhomogeneity in finite systems, usually terms containing gradients of the density  $\rho$  (Weizsäcker term)<sup>3</sup> are added to the kinetic energy density. However, for simplification we neglect such terms and calculate the kinetic energy of a nucleon in the

local density approximation by substituting  $\rho$  in eq. 6.13 by the actual density  $\rho(r=\langle r \rangle)$  at every nucleon site. Therefore, the total Fermi-gas kinetic energy ( $T_F$ ) is given by

$$T_F = \sum_i \frac{3}{5} \frac{\hbar^2}{2m} \left[ \frac{3\pi^2}{2} \right]^{2/3} \rho_{(r=\langle r_i \rangle)}^{2/3} \quad (6.14)$$

In the ground state the total kinetic energy calculated from eq. 6.14 must, therefore be equal to the total kinetic energy calculated from eq. 6.12. In excited states, we have  $\langle P_i \rangle \neq 0$  and the total kinetic energy is given by the first two terms in  $\langle H \rangle$  (eq. 6.10) while the average Fermi kinetic energy in eq. 6.14 requires corrections for non-zero temperatures in the excited states.<sup>4</sup> However, as far as the quantum mechanical part of the total energy in the excited state is concerned we assume that it can still be obtained from either eq. 6.12 or, eq. 6.14, i.e. we assume that  $T_{QM} = T_F$ .

By equating the right hand sides of the two equations (eq. 6.12 and 6.14) we get, for each nucleon

$$\frac{3}{4} \frac{\hbar^2}{2m} \frac{1}{\sigma_i^2} = \frac{3}{5} \frac{\hbar^2}{2m} \left[ \frac{3\pi^2}{2} \right]^{2/3} \rho_{(r=\langle r_i \rangle)}^{2/3}$$

or

$$\rho(r=\langle r_i \rangle) = \left[ \frac{5}{4} \left( \frac{2}{3\pi^2} \right)^{2/3} \frac{1}{\sigma_i^2} \right]^{3/2} \quad (6.15)$$

where  $\rho(r = \langle r_i \rangle)$  from eq. 6.11 is given by

$$\rho(r=\langle r_i \rangle) = \sum_j \frac{1}{(2\pi\sigma_j^2)^{3/2}} \exp\left[-\frac{(\langle r_i \rangle - \langle r_j \rangle)^2}{2\sigma_j^2}\right] \quad (6.16)$$

Separating the  $j=i$  term in eq. 6.16, and equating eq. 6.15 and 6.16 for  $\rho(r=\langle r_i \rangle)$ , we get,

$$\begin{aligned} \frac{1}{(2\pi\sigma_i^2)^{3/2}} + \sum_{j \neq i} \frac{1}{(2\pi\sigma_j^2)^{3/2}} \exp\left[-\frac{(\langle r_i \rangle - \langle r_j \rangle)^2}{2\sigma_j^2}\right] \\ = \left(\frac{5}{4}\right)^{3/2} \left(\frac{2}{3\pi^2}\right) \frac{1}{\sigma_i^3} \end{aligned} \quad (6.17)$$

Denoting  $R_1, R_2, \dots, R_A$  for  $\langle r_1 \rangle, \langle r_2 \rangle, \dots, \langle r_A \rangle$  respectively, for simplicity, and solving for  $\sigma_i$  in eq. 6.17, we get an expression for  $\sigma_i$  given by

$$\sigma_i = b \left[ \sum_{j \neq i} \frac{1}{\sigma_j^3} \exp\left[-\frac{(R_i - R_j)^2}{2\sigma_j^2}\right] \right]^{-1/3} \quad (6.18)$$

where

$$b = \left[ (2\pi)^{3/2} \left[ \left(\frac{5}{4}\right)^{3/2} \left(\frac{2}{3\pi^2}\right) - \frac{1}{(2\pi)^{3/2}} \right] \right]^{1/3} \quad (6.19)$$

For  $i = 1, 2, \dots, A$ , eq. 6.18 forms a set of  $A$  non-linear coupled equations for  $\sigma_i$  which can be solved by a self-consistent iterative procedure. Starting with any given initial values of  $\sigma_i$

the solution of eq. 6.18 gives a unique set of values for the width of the wave packets.  $\sigma_i$ 's do not depend on the choice of the interaction potential but are entirely determined by the instantaneous state of a given configuration  $\{R_i(t)\}$ . Therefore, we find

$$\sigma_i = \sigma_i(R_1(t), R_2(t), \dots, R_A(t)) \equiv \sigma_i(\{R_i(t)\}) \quad (6.20)$$

The  $\sigma_i$ 's do not have explicit time dependence. The implicit time dependence, however, does appear in  $\sigma_i$ 's due to the time dependence of the configuration  $\{R_i(t)\}$  which is described in section 6.2.6. Though we have used the product wave function ansatz for the nuclear wave function (eq. 6.7) which explicitly neglects all the correlations, we have built-in some correlations through the above prescription and the dependence of the width ( $\sigma_i$ ) of every wave packet on the entire configuration  $\{R_i(t)\}$ .

Figure 6.1 shows some examples of configurations for the simple cases of  $A=2, 3$  and  $4$ . The values of the width  $\sigma_i$  are determined from eq. 6.18 for the 3-dimensional gaussian wave packets (eq. 6.4) which are centred at the points shown in the figure. Figure 6.1 demonstrates the configuration dependence of  $\sigma_i$ 's. The  $A = 2$  case is further discussed in section 6.3.1 and a ground state configuration of an  $A = 16$  ( $^{16}\text{O}$ ) nucleus is obtained in section 6.3.2.

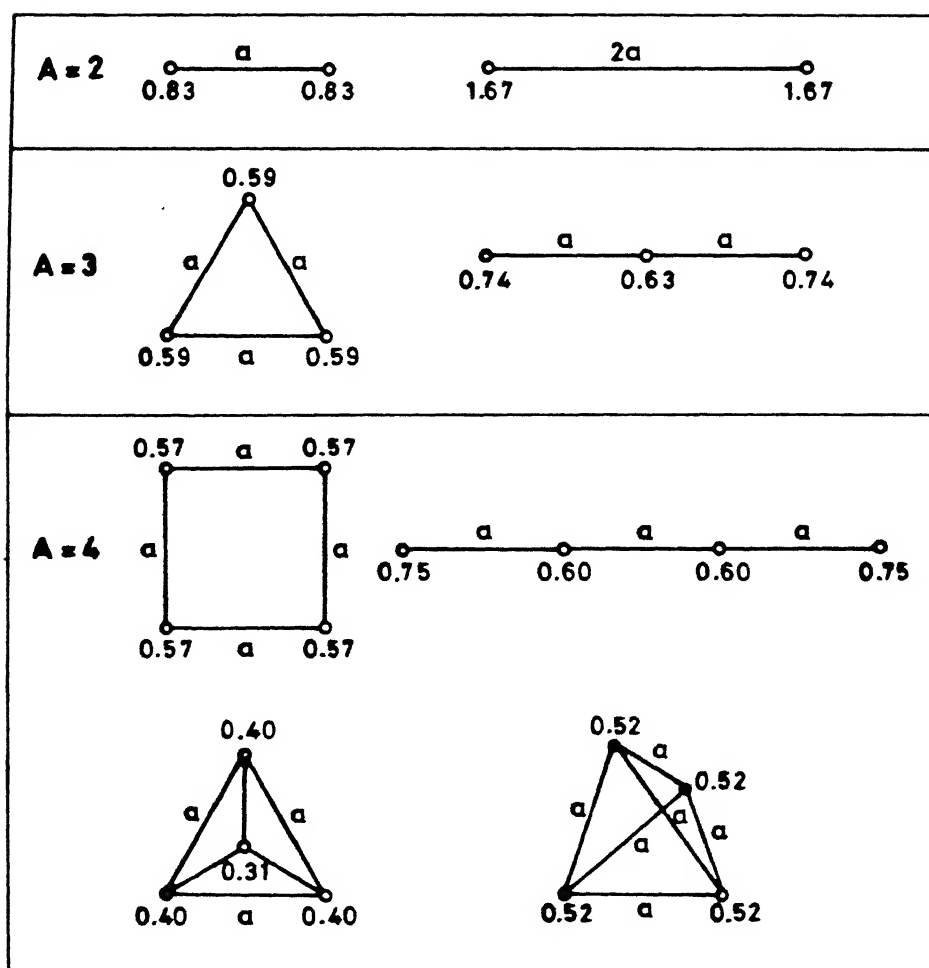


FIGURE 6.1

Some configurations of the 3-dimensional gaussian wave-packets in the simple cases of  $A = 2, 3$ , and  $4$ . The points shown are the sites where the centroids of the wave-packets are located and the numbers are the width ( $\sigma$ ) of the corresponding wave-packets in fm.; the length  $a$  is equal to 1.0 fm.

### 6.2.4 Two-Body Potentials

For the present study we choose the same form of the two-body potentials which are used in chapters 4. The NN-potential is given by

$$v_{ij}^N(r_{ij}) = -V_0 (1 - C/r_{ij}) \exp(-r_{ij}^2/r_0^2) \quad (6.21)$$

and the usual Coulomb interaction between protons is given by

$$v_{ij}^C(r_{ij}) = 1.44/r_{ij} \text{ (MeV)} \quad (6.22)$$

The expectation value  $\langle v_{ij} \rangle$  (eq. 6.9) of the above potentials are derived in the Appendix B. The result for the NN potential (eq. 6.21) gives

$$\begin{aligned} \langle v_{ij}^N(r_{ij}) \rangle = & -V_0 \left[ \frac{r_0^3}{R_0^3} - \frac{C}{R_{ij}} \frac{r_0}{R_0} \operatorname{erf} \left( \frac{R_{ij}}{(2\sigma_i^2 + 2\sigma_j^2)^{1/2}} \frac{r_0}{R_0} \right) \right] \\ & \times \exp \left[ \frac{-R_{ij}^2}{R_0^2} \right] \end{aligned} \quad (6.23)$$

where

$$R_{ij} = |R_i - R_j| = |\langle r_i \rangle - \langle r_j \rangle| \quad (6.24)$$

and

$$R_0 = (r_0^2 + 2\sigma_i^2 + 2\sigma_j^2)^{1/2} \quad (6.25)$$

and  $\operatorname{erf}(x)$  is the error function.

The integral (eq.6.9) for the Coulomb potential (eq. 6.22) gives .

$$\langle v_{ij}^C(r_{ij}) \rangle = \frac{1.44}{R_{ij}} \operatorname{erf} \left[ \frac{R_{ij}}{(2\sigma_i^2 + 2\sigma_j^2)^{1/2}} \right]^{(\text{MeV})} \quad (6.26)$$

If  $\sigma_i = \sigma_j = \sigma$  then  $\langle v_{ij}^N(r_{ij}) \rangle$  (eq. 6.23) and  $\langle v_{ij}^C(r_{ij}) \rangle$  (eq 6.26) reduce to the corresponding expressions(5.26 and 5.29) in chapter 5.

### 6.2.5 Ground State Solution Of Many-Body Systems

In the ground state we have  $\langle P_i \rangle = 0$  as discussed earlier. Therefore, the expectation value of the Hamiltonian  $\langle H \rangle$  or the total energy is given by

$$\langle H \rangle = \sum_i \left[ -\frac{3}{4} \frac{\hbar^2}{2m} \cdot \frac{1}{\sigma_i^2} \right] + \sum_i \sum_{j>i} \langle v_{ij} \rangle \quad (6.27)$$

To find the ground state configuration and the ground state binding energy we use the variational principle. We choose the trial single-particle wave functions  $\{\phi_i\}$  by picking up a randomly generated configuration  $\{R_i\}$  of the position of the centroids of the gaussian wave packets. To start with, we also choose  $\{\sigma_i\}$  randomly. However, since  $\{\sigma_i\}$  are uniquely determined for a given configuration  $\{R_i\}$  by solving eq. 6.18, we do not treat  $\{\sigma_i\}$  as variational parameters in this approach. We then cyclically minimize the total energy of the system given by  $\langle H \rangle$  in eq. 6.27 with respect to small variations  $\delta R_i$  of the coordinates of the centroids of individual wave packets, taking one at a time and keeping the other centroids fixed. This method is similar to the

"STATIC" method described in chapter 2 (Section 2.2.(a)).

However, an important difference arises between the method described here and the "STATIC" method described in chapter 2 (section 2.2(a)). In chapter 2, it was sufficient to calculate and minimize the total potential energy of the individual nucleons in each variation, since, due to the fixed positions of all the other nucleons the interaction energy between the fixed nucleons does not change. However, it should be noticed that in the present method, though we keep all the other  $\{R_i\}$  fixed for each variation, due to the dependence of  $\sigma_i$  on the positions of all the centroids  $\{R_i\}$ , a single variation of the centroid coordinate of a given wave packet changes the values of  $\sigma$  for all the wave packets. Therefore, the interaction energy between the fixed wave packets also changes due to the dependence of each  $\langle v_{ij} \rangle$  on  $\sigma_i$  and  $\sigma_j$  (eq. 6.23, 6.26). Thus, it is necessary in this case to minimize the total energy (eq.6.27) instead of minimizing only the total energy  $U_i$  of each wave packet given by

$$U_i = \frac{3}{4} \frac{\hbar^2}{2m} \frac{1}{\sigma_i^2} + \sum_{j \neq i} \langle v_{ij} \rangle$$

Except for this departure the basic structure of the algorithm, however, remains much the same as that of the method "STATIC" in section 2.2(a).

The ground state binding energy is calculated from eq. 6.27 with the ground state wave functions, and the rms radius is given by



$$\langle r^2 \rangle^{1/2} = \left[ \frac{\sum_i (\langle r_i \rangle^2 + 3\sigma_i^2)}{A} \right]^{1/2} \quad (6.28)$$

### 6.2.6 Dynamic Evolution of a Many-Particle Gaussian Wave Packet System.

If  $H_{cl}(r_1, r_2, \dots, r_A, p_1, p_2, \dots, p_A)$  is the classical Hamiltonian of a many-body system then in the Hamiltonian Formulation of classical mechanics the equations of motion of  $r_i$  and  $p_i$  are given by<sup>5</sup>

$$\frac{d\vec{r}_i}{dt} = \frac{\partial H_{cl}(r_1, r_2, \dots, r_A, p_1, p_2, \dots, p_A)}{\partial p_i} \quad (6.29a)$$

and

$$\frac{d\vec{p}_i}{dt} = - \frac{\partial H_{cl}(r_1, r_2, \dots, r_A, p_1, p_2, \dots, p_A)}{\partial r_i} \quad (6.29b)$$

We assume that the gaussian wave packets remain gaussian at all times, though this is strictly true only for the potentials with upto quadratic terms only. With this assumption the dynamic evolution of the wave packets is obtained by the equations of motion for the centroids of the wave packets  $\{R_i\}$  while the widths

$\{\sigma_i\}$  are determined in the present approach by eq. 6.18 from the instantaneous configuration of the centroid positions  $\{R_i(t)\}$ .

We adopt a semi-classical picture in which we replace the classical variables  $\{r_i, p_i\}$  and the classical Hamiltonian  $H_{cl}\{r_i, p_i\}$  by their respective expectation values, viz  $\{R_i = \langle r_i \rangle, P_i = \langle p_i \rangle\}$  and  $\langle H \rangle$  (eq. 6.10). For the two-body potentials which are chosen in section 6.2.4, it is clear from the equations 6.23 and 6.26 and from eq. 6.20 that  $\langle H \rangle$  given by eq. 6.10 is a function of  $\{R_i\}$  and  $\{P_i\}$  only, that is  $\langle H \rangle = \mathcal{H}(\{R_i, P_i\})$ . Therefore, we also replace  $\partial/r_i$  and  $\partial/p_i$  in equation 6.29 by  $\partial/\partial R_i$  and  $\partial/\partial P_i$  respectively. Thus, we get the equations of motion for the mean values  $\{R_i\}$  and  $\{P_i\}$  of the wave packets from the eq. 6.29;

$$\frac{dR_k}{dt} = \frac{\partial \mathcal{H}(\{R_i, P_i\})}{\partial P_k} \quad (6.30a)$$

$$\frac{dP_k}{dt} = -\frac{\partial \mathcal{H}(\{R_i, P_i\})}{\partial R_k} \quad (6.30b)$$

for  $k=1, 2, \dots, A$ . With the  $\langle H \rangle$  given by eq. 6.10, eq. 6.30 become

$$\frac{dR_k}{dt} = \frac{P_i}{m} \quad (6.31)$$

$$m \frac{d^2 R_k}{dt^2} = \frac{-\partial \langle H \rangle}{\partial R_k} \quad (6.32)$$

The equations 6.31 and 6.32 are the equations of motion for the centroids of the wave packets.

The right hand side of eq. 6.32 is the net force acting on the  $k^{\text{th}}$  wave packet and it is found by taking the gradient of eq. 6.10 with respect to  $R_k$ , giving

$$\begin{aligned} \frac{-\partial \langle H \rangle}{\partial R_k} = & \left[ \sum_i \frac{3 \hbar^2}{4 m} \left( \frac{2}{\sigma_i^3} \right) \frac{\partial \sigma_i(R_1, R_2, \dots, R_A)}{\partial R_k} \right] \\ & + \left[ \sum_i \sum_{j \neq i} \frac{-\partial \langle v_{ij} \rangle}{\partial R_k} \right] \end{aligned} \quad (6.33)$$

As discussed in section 6.2.5, since  $\langle v_{ij} \rangle$  depends on  $\sigma_i$  and  $\sigma_j$  (eq. 6.23, 6.26) and due to the dependence of  $\sigma$  on  $(R_1, R_2, \dots, R_A)$ ,  $\langle v_{ij} \rangle$  becomes non-local in character. Therefore, all the terms in the potential energy in eq. 6.10 are required to be differentiated with respect to  $R_k$  and the second bracket on the right hand side of eq. 6.33 does not reduce simply to

$\sum_{j \neq i} -\partial \langle v_{ij} \rangle / \partial R_k$  as in the case of point particles or the frozen wave packets.

$\partial \sigma_i / \partial R_k$  in eq. 6.33 are obtained by differentiating  $\sigma_i$  in eq. 6.18 with respect to  $R_k$ , giving

$$\frac{\partial \sigma_i(R_1, R_2, \dots, R_A)}{\partial R_k} = \left( \frac{\sigma_i^4}{b^3} \right) \sum_{j \neq i} \left[ \frac{1}{\sigma_j^4} \left[ \frac{R_{ij}}{\sigma_j} \frac{\partial R_{ij}}{\partial R_k} + \left( 3 - \frac{R_{ij}^2}{\sigma_j^2} \right) \frac{\partial \sigma_j}{\partial R_k} \right] \right. \\ \left. \times \exp \left[ - R_{ij}^2 / 2\sigma_j^2 \right] \right] \quad (6.34)$$

where,  $R_{ij} = R_i - R_j$ .

Thus at any given instant  $t$ , we first find  $\{\sigma_i\}$  from eq. 6.18 with the instantaneous configuration  $\{R_i(t)\}$  and then similarly solve the  $A$ -coupled eqs. 6.34 to find  $\partial \sigma_i / \partial R_k$  for  $i=1, 2, \dots, A$ . Similarly, we find  $\partial \sigma_i / \partial R_k$  for  $k=1, 2, \dots, A$ . Thus the eqs. 6.31 and 6.33 together with  $\sigma_i$  and  $\partial \sigma_i / \partial R_k$  as described above and  $\partial \langle v_{ij} \rangle / \partial R_k$  found from eq. 6.23 and eq. 6.26 completely determine the time evolution of a many-particle gaussian wave-packet system in this semi-classical microscopic approach.

### 6.3 RESULTS AND DISCUSSIONS

The equations in section 6.2.6 can be solved in principle to find the dynamic evolution of any A-particle system. However, due to the iterative solutions of the equations for  $\sigma_i$  and  $\partial\sigma_i/\partial R_K$ , and also due to the non-local character of  $\langle v_{ij} \rangle$ , computations may become tedious in practice for large values of A and require several orders of magnitude more computer time compared to the corresponding calculations in the earlier chapters. Therefore, in the present work, as an example of the dynamic evolution, we study the simplest case of A=2 only. The A=2 case is easier to solve and it demonstrates the effects of "Pauli repulsion". Also, in section 6.3.2 we give an example of a many-particle system such as  $^{16}\text{O}$ , and find its ground state configuration.

#### 6.3.1 Study of a Two-Body System

The expectation value  $\langle H \rangle$  (eq. 6.10) for a two wave packet system is given by

$$\langle H \rangle = \frac{\langle P_1 \rangle^2}{2m} + \frac{\langle P_2 \rangle^2}{2m} + \frac{3}{4} \frac{\hbar^2}{2m} \frac{1}{\sigma_1^2} + \frac{3}{4} \frac{\hbar^2}{2m} \frac{1}{\sigma_2^2} + \langle v_{12} \rangle \quad (6.35)$$

For a two wave packet system it is easy to find an expression for the widths  $\sigma_1$  and  $\sigma_2$  of the two wave packets. We note that due to the symmetry of the system the widths of the two wave packets have the same values, i.e.  $\sigma_1 = \sigma_2 = \sigma$ . Then, eq. 6.35 reduces to

$$\langle H \rangle = \frac{\langle P_1 \rangle^2}{2m} + \frac{\langle P_2 \rangle^2}{2m} + \frac{3}{4} \frac{\hbar^2}{2m} \left( \frac{2}{\sigma^2} \right) + \langle v_{12} \rangle \quad (6.35)$$

and eq. 6.18 gives

$$\sigma = b \left[ \exp(-R_{12}^2/2\sigma^2) \right]^{-1/3}$$

or, solving for  $\sigma^2$  we get

$$\sigma^2 = \frac{-R_{12}^2}{2 \ln b^3}$$

or,

$$\sigma = a R_{12} \quad (6.36)$$

where

$$R_{12} = |R_1 - R_2| = |\langle r_1 \rangle - \langle r_2 \rangle|$$

and

$$a = (2 \ln b^{-3})^{-1/2}$$

With the value of  $b$  given by eq. 6.19, we find  $a=0.833$ .

We now discuss expression (6.35) for two particular cases of  $v_{12} = 0$  and  $v_{12} \neq 0$ .

(a) Case of  $v_{12} = 0$

For  $v_{12} = 0$  and  $\alpha$  given by eq. 6.36, eq. 6.35 gives,

$$\langle H \rangle = \frac{\langle P_1 \rangle^2}{2m} + \frac{\langle P_2 \rangle^2}{2m} + \frac{3}{4} \frac{\hbar^2}{2m} \left[ \frac{2}{a^2 R_{12}^2} \right] \quad (6.37)$$

and we find

$$\frac{-\partial \langle H \rangle}{\partial R_1} = \frac{3}{4} \frac{\hbar^2}{2m} \frac{4}{a^2} \frac{\hat{R}_{12}}{R_{12}^3} \quad (6.38a)$$

and

$$\frac{-\partial \langle H \rangle}{\partial R_2} = \frac{3}{4} \frac{\hbar^2}{2m} \frac{-4\hat{R}_{12}}{a^2 R_{12}^3} \quad (6.38b)$$

where  $\hat{R}_{12}$  is a unit vector along  $(\vec{R}_1 - \vec{R}_2)$ .

Substituting the eq. 6.38 in eq. 6.32, we find the equations of motion for the centroids  $R_1$  and  $R_2$  respectively, given by

$$m \frac{d^2 R_1}{dt^2} = \left[ \frac{3\hbar^2}{2ma^2} \right] \frac{\hat{R}_{12}}{R_{12}^3} \quad (6.39a)$$

and

$$m \frac{d^2 R_2}{dt^2} = - \left[ \frac{3\hbar^2}{2ma^2} \right] \frac{\hat{R}_{12}}{R_{12}^3} \quad (6.39b)$$

Thus, we find that even though the two-body interaction

between the two wave-packets is zero ( $v_{12}=0$ ), the two wave packets are acted upon by a repulsive force given by eq. 6.39. In a dynamic evolution the centroids of the two wave packets move apart and go to  $\infty$  as time  $t \rightarrow \infty$ ; while the wave packets spread out with their width  $\sigma$  increasing according to eq. 6.36, as  $R_{12}$  increases.

Therefore, the third term in eq. 6.37 can also be considered as a "Pauli repulsive potential" between the two wave-packets. This term acts to prevent close encounters of the wave packets, as it goes to  $+\infty$  as  $R_{12} \rightarrow 0$ .

(b) Case of  $v_{12} \neq 0$  :

For  $v_{12} \neq 0$ , we have

$$\langle H \rangle = \frac{\langle P_1 \rangle^2}{2m} + \frac{\langle P_2 \rangle^2}{2m} + \frac{3}{4} \frac{\hbar^2}{2m} \left[ \frac{2}{a^2 R_{12}^2} \right] + \langle v_{12} \rangle \quad (6.40)$$

with  $\sigma_1 = \sigma_2 = \sigma$ ,  $\langle v_{12}^N \rangle$  in eq. 6.23 reduces to

$$\langle v_{12}^N \rangle = -V_0 \left[ \frac{r_0^3}{R_0^3} - \frac{C}{R_{12}} \frac{r_0}{R_0} \operatorname{erf} \left( \frac{r_0}{2aR_0} \right) \right] \exp \left( \frac{-R_{12}^2}{R_0^2} \right) \quad (6.41)$$

where  $R_0 = (r_0^2 + 4a^2 R_{12}^2)^{1/2}$

Differentiating eq. 6.41 with respect to  $R_{12}$ , we get



$$\begin{aligned}
\frac{-\partial \langle v_{12}^N \rangle}{\partial R_{12}} = V_0 \left[ \frac{-2r_0^3}{R_0^5} \left( 6a^2 + \frac{r_0^2}{R_0^2} \right) R_{12} + \frac{C r_0^2}{4\pi} \frac{4a}{R_0^4} \right. \\
\left. \exp \left( \frac{-r_0^2}{4a^2 R_0^2} \right) + \left\{ \frac{2Cr_0}{R_0^3} \left( 2a^2 + \frac{r_0^2}{R_0^2} \right) + \frac{Cr_0}{R_0} \frac{1}{R_{12}^2} \right\} \right. \\
\left. \operatorname{erf} \left( \frac{r_0}{2aR_0} \right) \right] \times \exp \left( -R_{12}^2 / R_0^2 \right) \quad (6.42)
\end{aligned}$$

We choose an arbitrary set of parameters ( $V_0 = 3200$  MeV,  $C = 0.8$  fm and  $r_0 = 1.2$  fm) for  $\langle v_{12}^N \rangle$  and find the ground state configuration for the two wave packet system by the method described in section 6.2.5. In the ground state of the <sup>two</sup> wave packet system with the above potential parameters, we find  $R_{12}^0 = 1.23$  fm,  $\sigma_1 = \sigma_2 = 1.03$  fm,  $\langle r^2 \rangle^{1/2} = 1.89$  fm,  $\langle v_{12}^N \rangle = -48.9$  MeV,  $T_{QM} = 29.9$  MeV and the total energy  $E = -19.0$  MeV.

The potential  $\langle v_{12}^N \rangle$  (eq. 6.41) with the above set of parameters is plotted in Figure 6.2 as a function of  $R_{12}$ .  $T_{QM}$  and  $(T_{QM} + \langle v_{12}^N \rangle)$  are also plotted in Figure 6.2. From Figure 6.2 we find that  $(T_{QM} + \langle v_{12}^N \rangle)$  has a minimum at  $R_{12} = 1.23$  fm, which is equal to  $-19.0$  MeV. Thus, we see that the determination of the ground state by the method described in section 6.2.5 indeed produces the minimum of  $\langle H \rangle$  for the two wave packets system. It is also to be noticed that the minimum of  $(T_{QM} + \langle v_{12}^N \rangle)$  is not at the same value of  $R_{12}$  as that for  $\langle v_{12}^N \rangle$ .

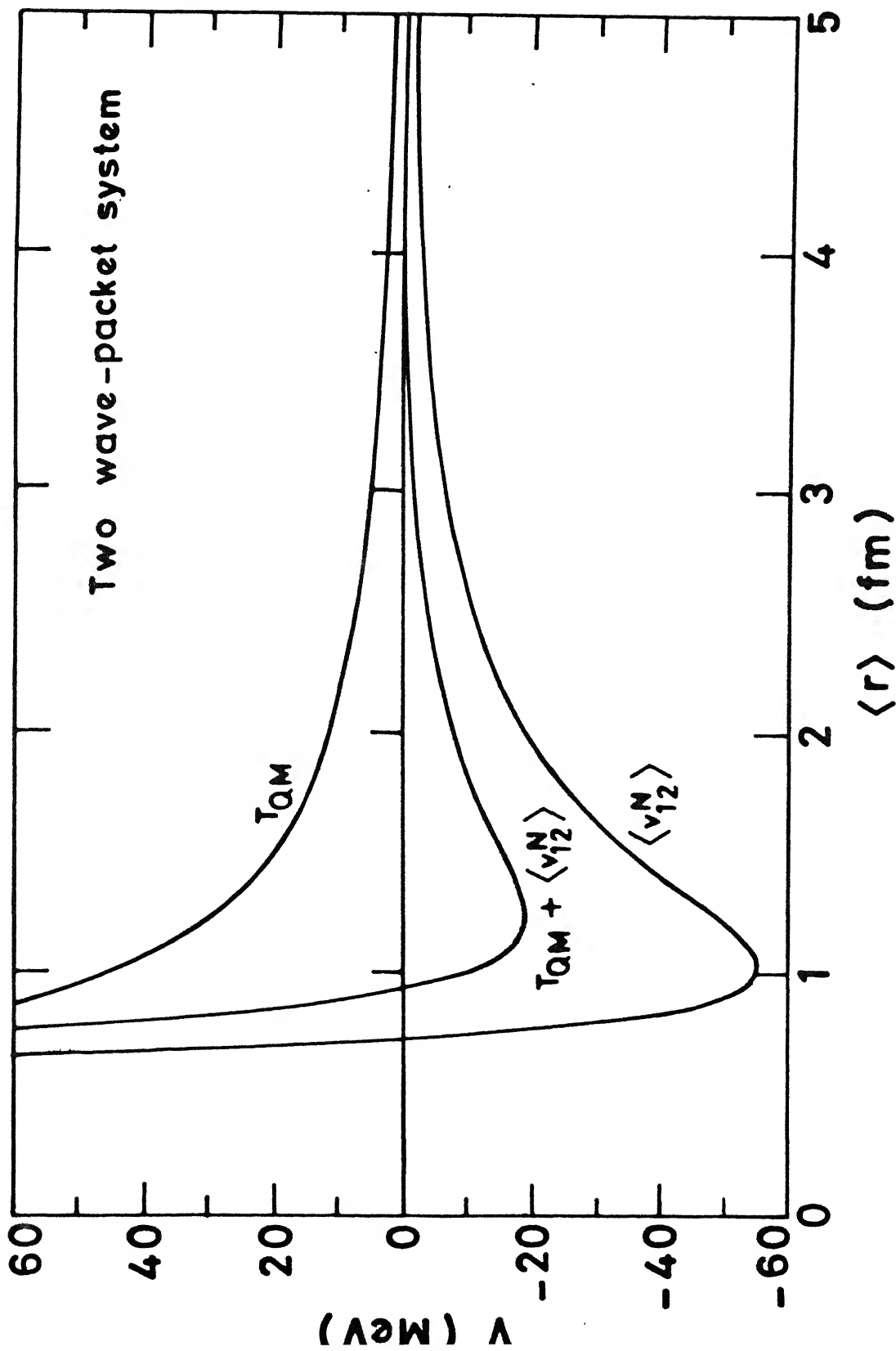


FIGURE 6.2

Potential  $\langle v_{12}^N \rangle$ , Q.M. kinetic energy  $T_{QM}$  and  $(\langle v_{12}^N \rangle + T_{QM})$  for two wave-packets versus the centroid separation  $R_{12}$  for the parameters  $V_0 = 3200$  MeV,  $C = 0.8$  fm, and  $r_0 = 1.2$  fm.

The dynamic evolution of the two wave packets described above, with the ground state as the initial condition, does not produce any change in its state. Therefore, the ground state obtained above is indeed an equilibrium configuration.

Starting with the following initial conditions given by  $\langle P_1 \rangle = 0$ ,  $\langle P_2 \rangle = 0$ , and  $R_{12} = 2.0$  fm, we study the time development of the two wave-packet system. The total energy  $\langle H \rangle$  and the total linear momentum ( $\vec{\langle P_1 \rangle} + \vec{\langle P_2 \rangle}$ ) is conserved. Figure 6.3 shows the time evolution of the centroids ( $R_1$  and  $R_2$ ), the distance  $R_{12}$  between the centroids, and the width of the wave packets  $\sigma$ . We see from Figure 6.3 that  $R_{12}$  oscillates between  $R_{12} = 2.0$  fm and  $R_{12} = 0.8$  fm corresponding to the respective turning points in Figure 6.2.  $\sigma$  also oscillates in phase with  $R_{12}$  and with the same frequency.

### 6.3.2 Study of a Many-Body System (Ground State of $^{16}\text{O}$ )

In this section we find the ground state configuration of  $^{16}\text{O}$ , as an example of the application of the semi-classical method described in section 6.2.5. We neglect the spin degree of freedom and consider each nucleon as described by a gaussian wave packet (eq. 6.4). We choose the NN-potential and the Coulomb potential given by expressions (6.23 and 6.26). We also consider the strength of the NN interaction between the like nucleons to be less than that between the unlike nucleons by about 20% as considered in chapters 4 and 5.

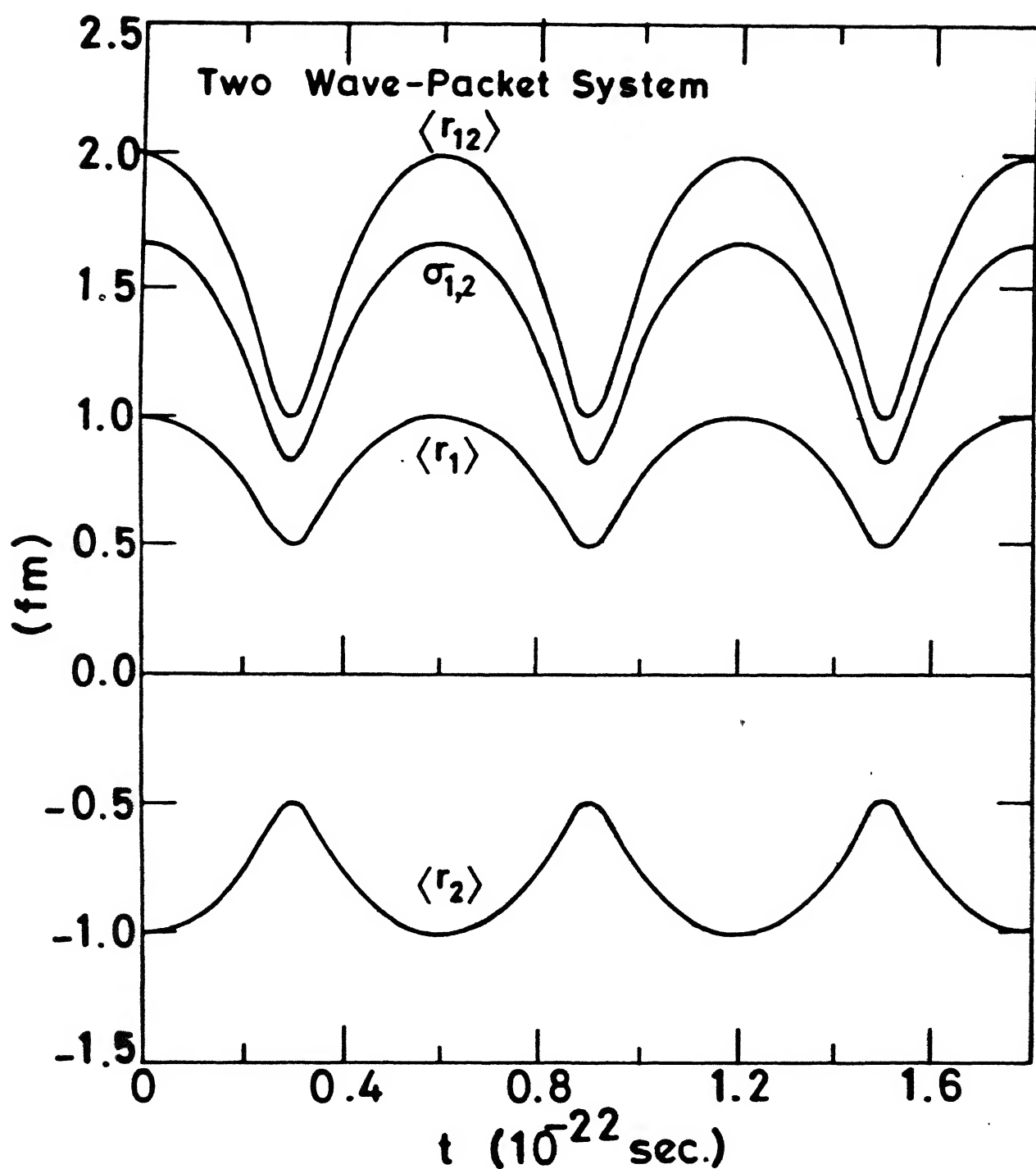


FIGURE 6.3

Time evolution of the centroid positions  $R_1$  and  $R_2$ , centroid separation  $R_{12}$  and the width  $\sigma_1$  and  $\sigma_2$  of the two wave-packets with the potentials shown in the Figure 6.2.

We choose  $r_0 = 1.2$  fm and adjust the parameters  $V_0$  and  $C$  in eq. 6.23 such that the binding energy and the rms radius of  $^{16}\text{O}$  in its ground state are close to the corresponding experimental values. Parameters of this potential (eq 6.23) and the corresponding ground state properties of  $^{16}\text{O}$  are given in Table 6.1.

The distribution  $n(\sigma)$  of the width ( $\sigma_1$ ) of the wave packets in the ground state of  $^{16}\text{O}$  is shown in Figure 6.4 and the radial distribution  $n(r)$  of the position of the wave packets is given in Figure 6.5. The value of  $\sigma_1$  varies from 0.78 fm for a wave packet in the central core region of the nucleus to about 0.99 fm for a wave packet on the surface. The average value of  $\sigma_1$  is about 0.92 fm.

The calculated value of the average kinetic energy per nucleon ( $\langle T \rangle / A$ ) for the above ground state configuration of  $^{16}\text{O}$  nucleus is about 19 MeV, which is in close agreement with the experimentally determined value ( $16 \pm 3$  MeV) from ref. 7.

The nuclear density distribution is calculated as described in chapter 5 section 5.2.4. The total nucleon density ( $\rho = \rho_p + \rho_n$ ) is plotted in Figure 6.6. Comparison with the density distributions calculated in chapter 5 (Figure 5.4) shows that the density distribution calculated in the present case is similar to that with the potential  $\langle W2 \rangle$  in chapter 5, but it is much smoother also.

Finally, we calculate the compressibility coefficient ( $K$ ) for the ground state of  $^{16}\text{O}$ . Calculation of  $K$  is also similar to

TABLE 6.1

Parameters of the effective NN potential and ground-state properties of  $^{16}\text{O}$

	Calculated	Experimental
$V_0$ (MeV)	3150.0	
$C$ (fm)	1.01	
$r_0$ (fm)	1.20	
Total Nuclear Potential energy (MeV)	-440.2	
Total Coulomb energy (MeV)	12.9	
$\langle T \rangle / A$ (MeV)	18.8	$16 \pm 3^7$
Binding energy (MeV)	-127.1	-127.6
$\langle r^2 \rangle^{1/2}$ (fm)	2.73	2.73
$K$ (MeV)	230	

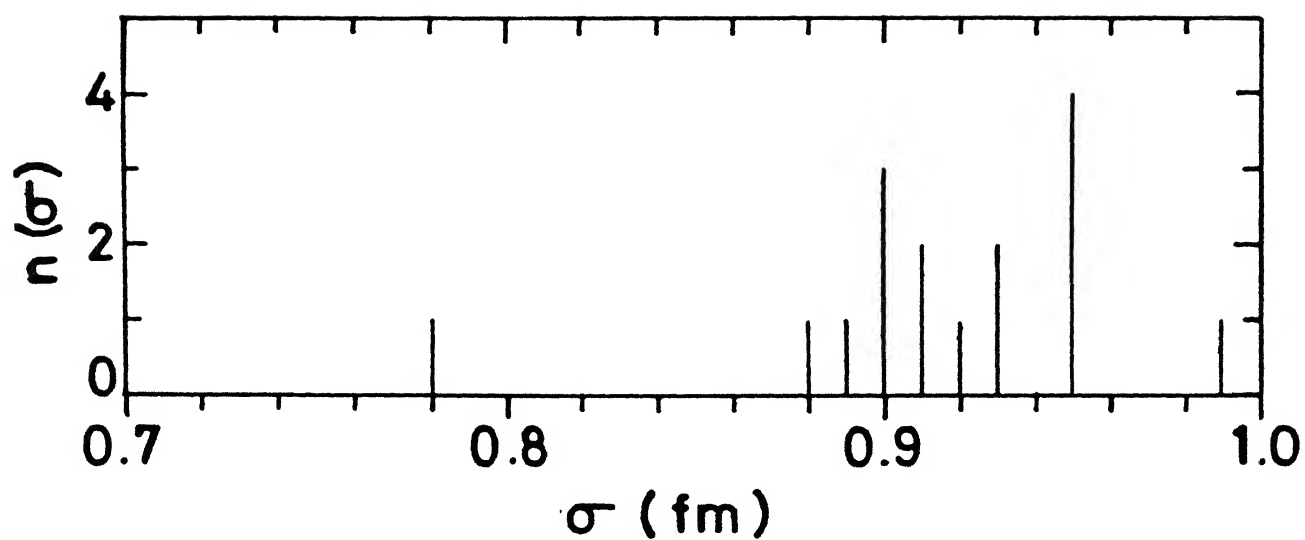


FIGURE 6.4 The distribution ( $n(\sigma)$ ) of the number of wave-packets with widths  $\sigma$  in the ground-state of  $^{16}\text{O}$  for the potential given in the Table 6.1.

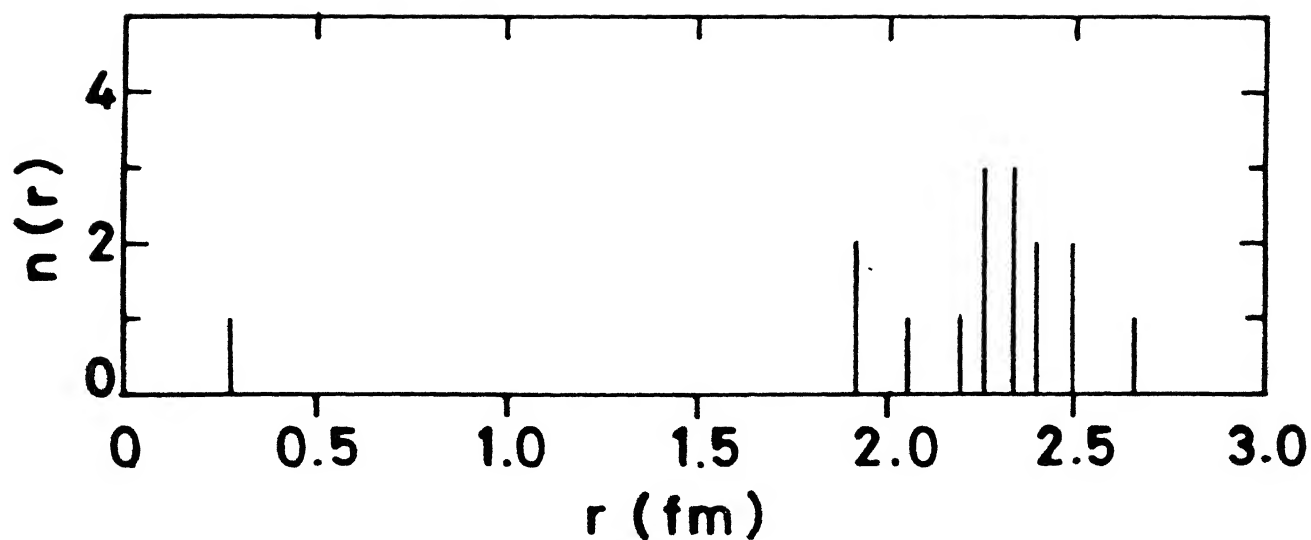


FIGURE 6.5 The distribution ( $n(r)$ ) of the number of wave-packets with their centroids located at radius ( $r$ ) in the ground state of  $^{16}\text{O}$ .



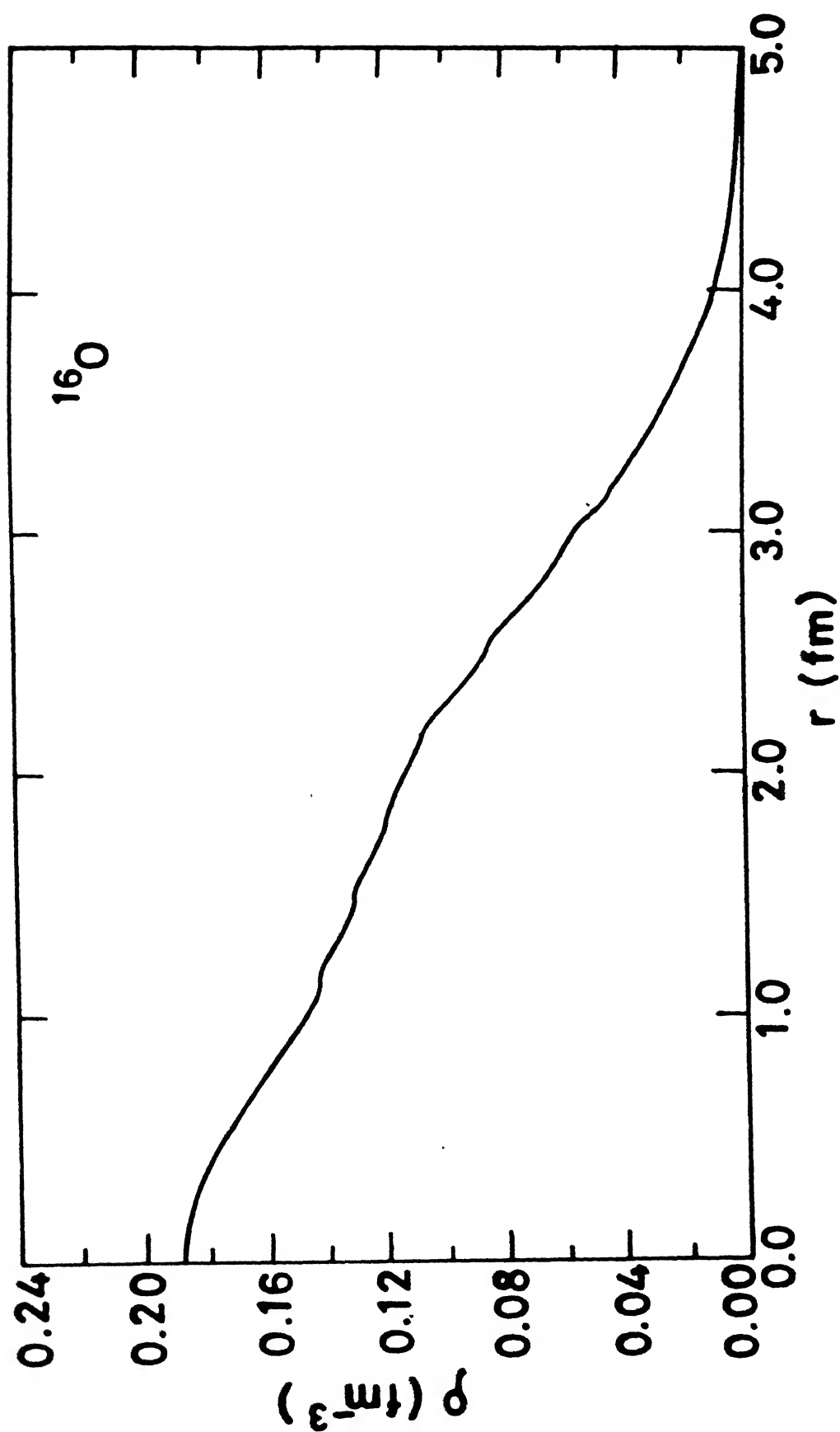


FIGURE 6.6 Calculated radial density ( $\rho(r)$ ) of nucleons in the ground-state of  $^{16}\text{O}$ .

that described in chapter 5 section 5.2.4. However, at each value of the nuclear radius we calculate the total energy after redetermining all the  $\sigma_1$ 's from eq. (6.18) for the compressed or the expanded configuration as the case may be. In Figure 6.7 we plot the average kinetic energy per nucleon ( $\langle T \rangle / A$ ), the average potential energy per nucleon  $V = (\sum_i \sum_{j>i} \langle v_{ij} \rangle) / A$  and the total energy per nucleon ( $E/A$ ) as a function of the rms radius ( $R = \langle r^2 \rangle^{1/2}$ ) of the compressed or the expanded configuration around the ground state. The calculated value of the compressibility coefficient  $K$  for  $^{16}\text{O}$  in the present calculation is about 230 MeV. This value is slightly higher than the value calculated for  $^{16}\text{O}$  in chapter 5 section 5.3.2 with the potential  $\langle W2 \rangle$  and it is also slightly higher compared to the RPA and the constrained Hartree-Fock calculations given in Ref. 8.

In Figure 6.8 we plot  $\langle v_{12}^N \rangle$ ,  $T_{QM}$  and  $(T_{QM} + \langle v_{12}^N \rangle)$  with the parameters given in Table 6.1 for a two wave-packet case (deuteron). It is seen from the Figure 6.8 that  $(T_{QM} + \langle v_{12}^N \rangle)$  does not have any bound state for a two wave-packet system. Therefore, in the present case the deuteron is unbound with the potential parameters given in table 6.1. The reason for this discrepancy may be in the explicit neglect of the spin degree of freedom and the exchange forces which are neglected in the present approach. It may also be necessary to consider non-spherical gaussian wave packets (eq. 6.1 and 6.2) with  $\sigma x_1$ ,  $\sigma y_1$  and  $\sigma z_1$ , since the transverse components of the width of two wave-packets may not change with respect to the inter-centroid separation  $R_{12}$ . Thus reducing their contribution to the total

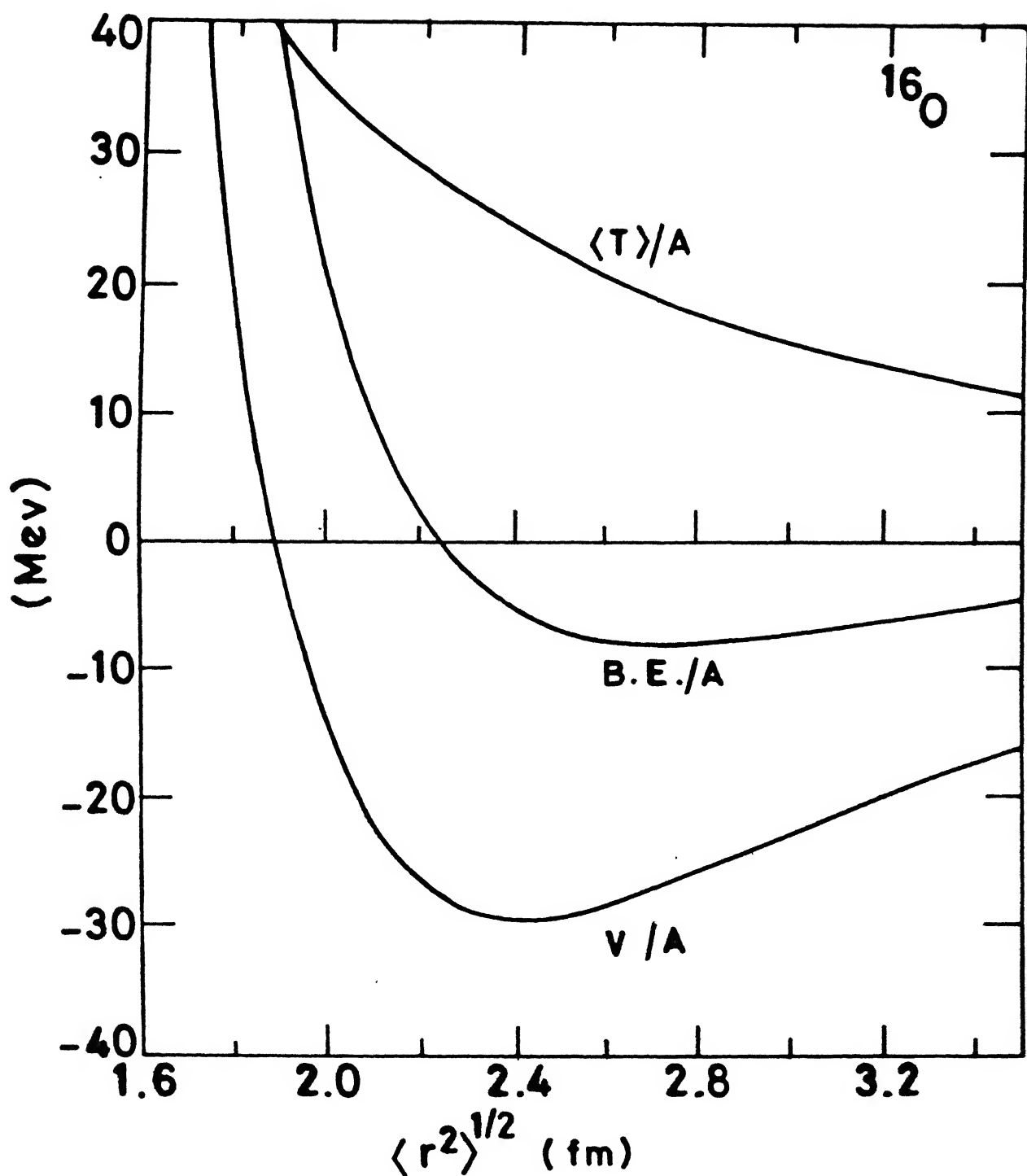


FIGURE 6.7

Plot of the average kinetic energy per nucleon ( $\langle T \rangle / A$ ), average potential energy per nucleon ( $V/A$ ), and the total energy per nucleon versus rms radius ( $R$ ) of the compressed or expanded configurations of  $^{16}\text{O}$  around  $R = R_{gs}$ .

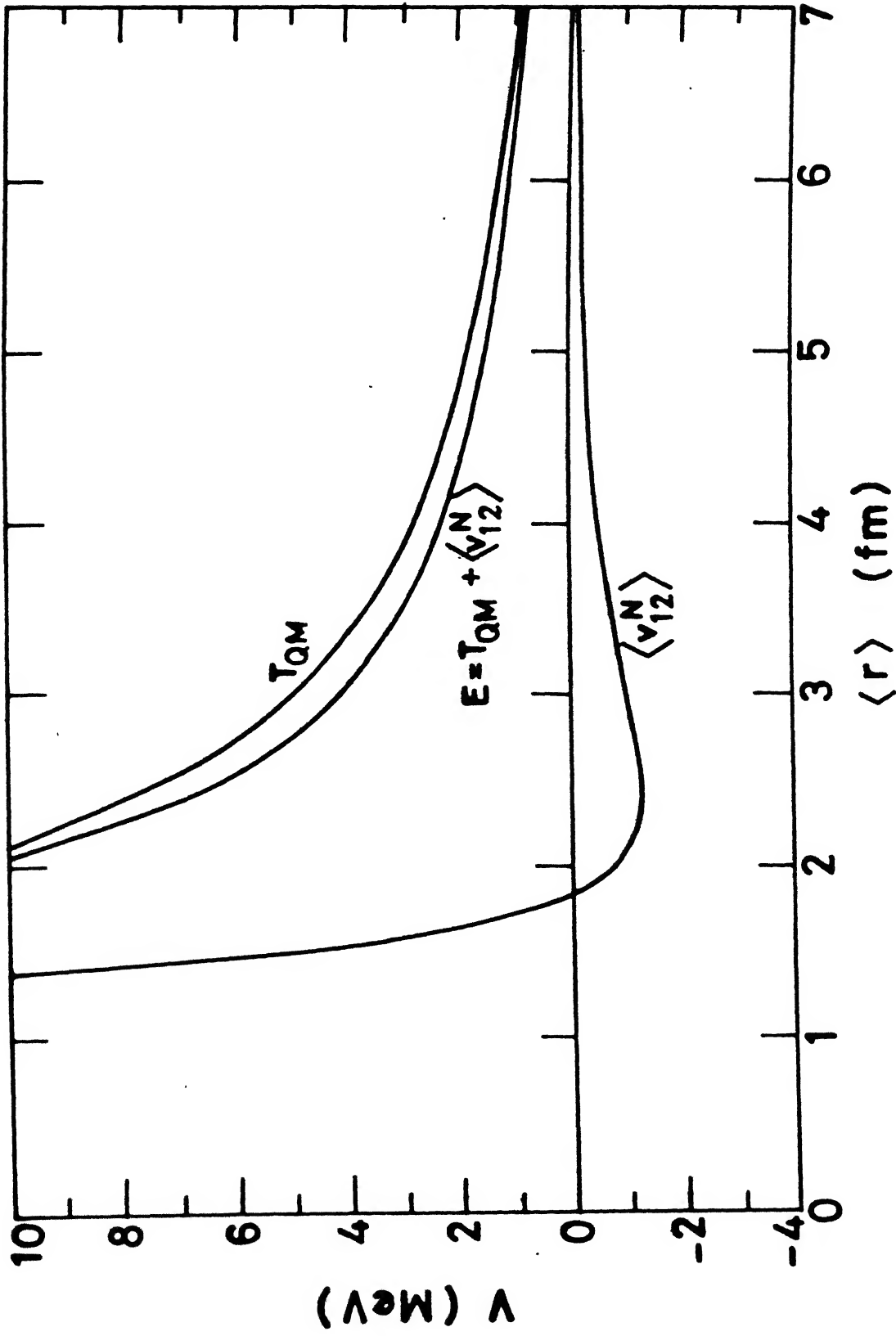


FIGURE 6.8

Potential  $\langle v_{12}^N \rangle$ , Q.M. kinetic energy  $T_{QM}$  and  $(\langle v_{12}^N \rangle + T_{QM})$  Vs. the centroid separation  $R_{12}$  in the case of a two wave-packet system with the potential given in Table 6.1.

repulsive kinetic energy ( $T_{QM}$ ).

#### 6.4 SUMMARY AND CONCLUSIONS

In the semi-classical microscopic approach presented above we assumed that each nucleon in a nucleus can be described by a minimum uncertainty gaussian wave packet. We further assumed that the wave packets always remain gaussian, but removed some of the assumptions made earlier in chapter 5 regarding the width of the wave packets. Using the Fermi-gas kinetic energy and the local density approximation we determined the width of every individual wave packet in the nucleus and its quantum mechanical part of the kinetic energy. We found that the width of a wave packet depends on its location in the instantaneous configuration. Thus, in this approach all the nucleons respect the uncertainty relation, and the effect of the "Pauli repulsion" arising from the exclusion principle in a many-body fermionic system is also incorporated.

Assuming the quantum mechanically derived expectation value  $\langle H \rangle$  of a many-body system in the Hartree-ansatz, as a new classical many-body Hamiltonian, we discussed the dynamic evolution of the expectation values of the position  $\{R_i\}$  and momentum  $\{P_i\}$  of the wave packets.

As a simple example, we studied the dynamic evolution of a two wave packet system and found that even in the absence of any two body interaction ( $v_{12} = 0$ ), the two wave packets move apart

due to the "Pauli-repulsion" - the wave packets spread out as they move apart. The zero-point fermi energy or the "Pauli-repulsion" for the two wave-packet system is found to vary as inverse square of the distance between the centroids of the two wave packets.

In a potential well the centroids of the two-wave packets show an oscillatory motion between the two turning points at the same total energy. The widths of the wave packets also oscillate with the same frequency and in phase with the motion of the centroids.

We also determined the ground state configuration of  $^{16}\text{O}$  nucleus by cyclically minimizing the total energy with respect to small variations of the individual centroid coordinates. By reproducing the ground state binding energy and the rms radius of  $^{16}\text{O}$ , by adjusting the potential parameters, we find that the average kinetic energy per nucleon in the ground state configuration of  $^{16}\text{O}$  is also in close agreement with the experimental value.<sup>7</sup> The calculated compressibility coefficient has a reasonable value compared to the other theoretical calculations and the nuclear density is also smooth.

It may be worthwhile to mention here that E.J. Heller (Ref. <sup>9</sup> and <sup>10</sup>) also developed two semiclassical methods for the dynamic evolution of the gaussian wave packets. One of the method is based on the Ehrenfest theorem which, however, is good only for a locally quadratic potential.<sup>9</sup> The other method is based on the Hartree-ansatz and the variational principle.<sup>10</sup> Recently, the

second approach was extended by Singer and Smith (Ref. 11) for gaussian wave packet simulation of some many-particle molecular systems. However, in the approach of Ref. (11) the exchange effects and quantum mechanical correlations for a fermionic system are neglected. Also, the widths of all the gaussian wave packets are assumed to be equal in Ref. 11. Though we also use the Hartree-ansatz for the many-body wave functions, the important effect of the exclusion principle is incorporated in the present approach through the use of a degenerate Fermi-gas kinetic energy function.

Aichelin and Stöcker (Ref. 12) have also used gaussian wave packets in a high-energy heavy-ion collision calculation. However, in the calculation of Ref. 12 the width of the wave packets are assumed to be constant and have the same given value for all the wave packets representing individual nucleons.

The semi-classical microscopic approach described in the present chapter for the dynamic evaluation of wave packets can be applied in the study of heavy-ion collisions. However, due to the enormity of the numerical task, it may take few orders of magnitude more computational time compared to the corresponding calculations presented in the earlier chapters. As discussed in section 6.3.2, it may be necessary to include the spin degree of freedom in the interaction potential to reproduce correct nuclear properties<sup>e</sup> for a range of nuclei. Also, it may be necessary to consider non-spherical gaussian wave packets, as discussed in

section 6.3.2 and also due to the fact that in high energy heavy-ion collisions high degree of asymmetry is involved as in the case of "side-splash" of nuclear matter (section 4.3.2). Nevertheless, the semiclassical approach developed here deserves further studies.



## REFERENCE

- 1 A. de Shalit and H. Feshbach, *Theoretical Nuclear Physics*, Vol. I (John Wiley and sons, 1974).
- 2 L.I. Schiff, *Quantum Mechanics*, (McGraw-Hill, 1955).
- 3 P. Ring and P. Schuck, *The Nuclear Many-Body Problem*, (Springer-Verlag, 1980)
- 4 J. Nemeth, M. Barranco, C. Ngo, and E. Tomasi, *Z. Phys.* **A323**, 419 (1986).
- 5 H. Goldstein, *Classical Mechanics*, (Addison Wesley ).
- 6 A. Messiah, *Quantum Mechanics*, Vol. I (John Wiley & sons, 1966).
- 7 J.M. Wilcox and B.J. Moyer, *Phys. Rev.* **99**, 875 (1955).
- 8 J.P. Blaizot, D. Gogny, and B. Grammaticos, *Nucl. Phys.* **A265**, 315 (1976).
- 9 E.J. Heller, *J. Chem. Phys.* **62**, 1544 (1975).
- 10 E.J. Heller, *J. Chem. phys.* **64**, 63 (1976).
- 11 K. Singer and W. Smith, *Molecular Physics* **57**, 761 (1986).
- 12 J. Aichelin and H. Stöcker, *Phys. Lett.* **176B**, 14 (1986).

## APPENDIX A

## INITIAL COULOMB TRAJECTORIES OF HEAVY-IONS

In this appendix we give the formulae for finding the positions and velocities of the ions in the centre-of-mass reference frame, at a given ion-ion separation ( $R_{CM}$ ).

Let  $b$  be the impact parameter for an  $A_1 + A_2$  collision, and let  $V$  be the initial velocity of the ion ( $A_1$ ) with mass  $m_1$  moving in the  $(-x)$ -direction as shown in the Figure A.1. In Figure A.1,  $C$  and  $C'$  are the two focii of the hyperbola that corresponds to the Coulomb trajectory of the ion  $A_1$ . The origin of the C.M. frame is established at  $C$ .

The components of the position  $\vec{R}_1 \equiv (x_1, y_1)$  and velocity  $\vec{v}_1 \equiv (v_{x_1}, v_{y_1})$  of ion ( $A_1$ ) are given by,

$$x_1 = r \cos \theta$$

$$y_1 = r \sin \theta$$

$$v_{x_1} = v_r \cos \theta - v_\psi \sin \theta$$

$$v_{y_1} = v_r \sin \theta + v_\psi \cos \theta$$

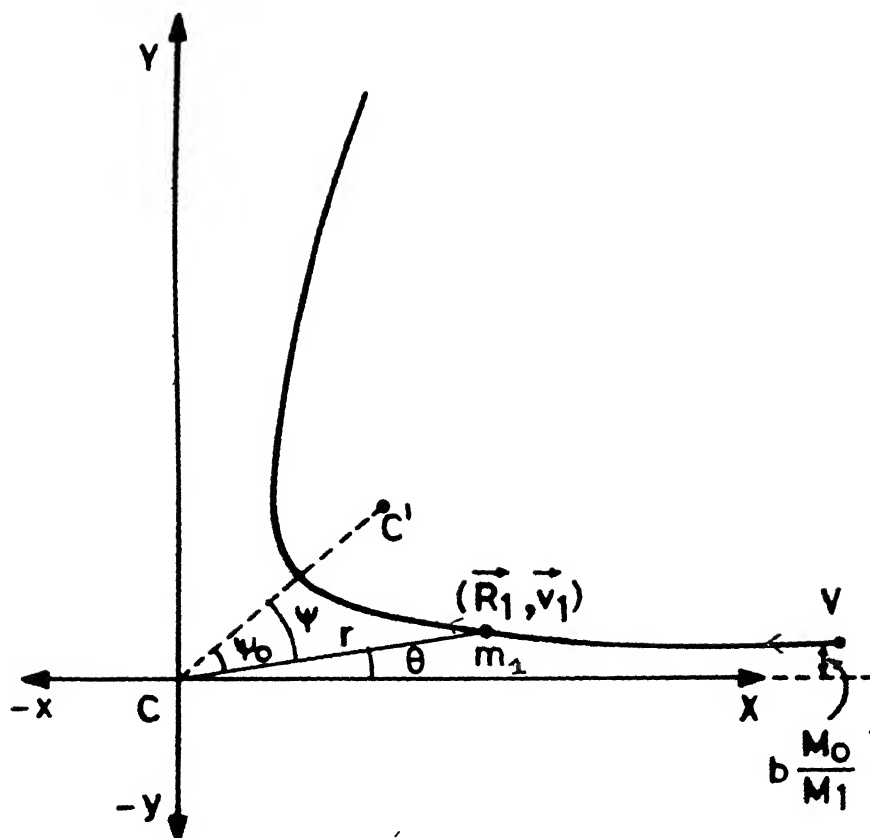


FIGURE A.1

Schematic diagram showing the Coulomb trajectory of one of the ion in the centre-of-mass reference frame. C and C' are the two focii of the hyperbola that corresponds to the trajectory of the ion.

where

$$r = R_{\text{CM}} \frac{M_0}{M_1}$$

$$\theta = \psi_0 - \psi$$

$$\cos \psi_0 = 1/\epsilon$$

$$\cos \psi = \frac{1}{\epsilon} \left[ 1 + \frac{a(\epsilon^2 - 1)}{r} \right]$$

$$v_r = \frac{dr}{dt} = \frac{dr}{d\psi} \frac{d\psi}{dt}$$

$$= \frac{- \left( \frac{M_0}{M_1} \right)^2 v b \epsilon \sin \psi}{a (\epsilon^2 - 1)}$$

$$v_\psi = r \frac{d\psi}{dt}$$

$$= \frac{- \left( \frac{M_0}{M_1} \right)^2 v b}{r}$$

With,

$$\text{reduced mass} : M_0 = \frac{M_1 M_2}{(M_1 + M_2)}$$

$$\text{Eccentricity} : \quad e = \left[ 1 + \left( \frac{2b}{d} \right)^2 \right]^{1/2}$$

$$\text{Collision parameter:} \quad a = \frac{d}{2} \frac{M_0}{M_1}$$

where,  $d$  is the distance of closest-approach for a head-on collision ( $b=0$ ), and it is given by

$$d = \frac{2|Z_1 Z_2| e^2}{M_0 v^2}$$

The components of the position  $\vec{R}_2 = (x_2, y_2)$  and velocity  $\vec{v}_2 \equiv (v_{x2}, v_{y2})$  of the other colliding ion ( $A_2$ ) are given by

$$x_2 = - \frac{M_1}{M_2} x_1, \quad y_2 = - \frac{M_1}{M_2} y_1$$

$$v_{x2} = - \frac{M_1}{M_2} v_{x1}, \quad v_{y2} = - \frac{M_1}{M_2} v_{y1}$$

#### REFERENCE:

R.D. Evans, *The Atomic Nucleus* (McGraw Hill, 1955), Appendix B.

## APPENDIX B

## EVALUATION OF DOUBLE-FOLDING INTEGRALS FOR THE TWO-BODY POTENTIALS

$$\langle v_{ij}(|r_i - r_j|) \rangle = \iint \phi_i^*(r_i) \phi_j^*(r_j) v_{ij}(|r_i - r_j|) \phi_i(r_i) \phi_j(r_j) d^3 r_i d^3 r_j \dots (1)$$

with  $\phi$ 's given by

$$\phi_i(r_i) = \frac{1}{(2\pi\sigma_i^2)^{3/4}} \exp \left[ -\frac{(r_i - \langle r_i \rangle)^2}{4\sigma_i^2} + \frac{i}{\hbar} \langle p_i \rangle \cdot (r_i - \langle r_i \rangle) \right] \dots (2)$$

we get

$$\begin{aligned} \langle v_{ij} \rangle = \frac{1}{(2\pi\sigma_i\sigma_j)^3} \iint \exp \left[ -\frac{(r_i - \langle r_i \rangle)^2}{2\sigma_i^2} \right] v_{ij}(|r_i - r_j|) \\ \cdot \exp \left[ -\frac{(r_j - \langle r_j \rangle)^2}{2\sigma_j^2} \right] d^3 r_i d^3 r_j \end{aligned} \quad (3)$$

Let us, for simplicity, choose the origin of the coordinate system at  $\langle r_i \rangle = 0$ , and let  $\langle r_j \rangle = r$ , then we get

$$\langle v_{ij} \rangle = \frac{1}{(2\pi\sigma_i\sigma_j)^3} \iint \exp \left[ - \left( \frac{r_i^2}{2\sigma_i^2} + \frac{(r_j-r)^2}{2\sigma_j^2} \right) \right]$$

$$v_{ij}(|r_i - r_j|) d^3r_i d^3r_j \quad \dots (4)$$

Now, consider the argument of the exponential in the above integral (eq. 4). Multiplying and dividing this term by  $(\sigma_i^2 + \sigma_j^2)$ , we get

$$\begin{aligned} & \frac{r_i^2}{2\sigma_i^2} + \frac{(r_j-r)^2}{2\sigma_j^2} \\ &= \frac{1}{2(\sigma_i^2 + \sigma_j^2)} \left[ \left( r_i^2 + \frac{\sigma_j^2}{\sigma_i^2} r_i^2 \right) + \left( (r_j-r)^2 + \frac{\sigma_i^2}{\sigma_j^2} (r_j-r)^2 \right) \right] \\ &= \frac{1}{2(\sigma_i^2 + \sigma_j^2)} \left[ \left( r_i^2 + \frac{\sigma_j^2}{\sigma_i^2} r_i^2 \right) - 2r_i(r_j-r) \right. \\ & \quad \left. + \left( (r_j-r)^2 + \frac{\sigma_i^2}{\sigma_j^2} (r_j-r)^2 \right) + 2r_i(r_j-r) \frac{\sigma_i\sigma_j}{\sigma_j\sigma_i} \right] \\ &= \frac{1}{2(\sigma_i^2 + \sigma_j^2)} \left[ (r_j-r_i-r)^2 + \left( \frac{\sigma_j}{\sigma_i} r_i + \frac{\sigma_i}{\sigma_j} (r_j-r) \right)^2 \right] \quad (5) \end{aligned}$$

Let us make the following transformations

$$\sigma^2 = (\sigma_i^2 + \sigma_j^2)/2 \quad (6)$$

$$R = r_j - r_i \quad (7a)$$

$$R' = \frac{\sigma_j}{\sigma_i} r_i + \frac{\sigma_i}{\sigma_j} (r_j - r) \quad (7b)$$

$$d^3 r_i d^3 r_j = |J| d^3 R d^3 R' \quad (8)$$

The Jacobian  $|J|$  for the above transformations is easily found :

$$|J| = \left[ \frac{\sigma_i \sigma_j}{(\sigma_i^2 + \sigma_j^2)} \right]^3 \quad (9)$$

With the transformations (eq. 7) and substitution (eq.6), the identity in eq. 5 becomes

$$\frac{r_i^2}{2\sigma_i^2} + \frac{(r_j - r)^2}{2\sigma_j^2} = \left[ \frac{(R - r)^2}{4\sigma^2} + \frac{R'^2}{4\sigma^2} \right] \quad (10)$$

Therefore, substituting eq. 8 and 10 with eq. 9, the double folding integral eq. 5 reduces to a product of two integrals over  $R'$  and  $R$  respectively :

$$\langle v_{ij} \rangle = \frac{1}{(4\pi\sigma^2)^3} I_{R'} \cdot I_R \quad (11)$$

where



$$\begin{aligned}
 I_{R'} &= \int \exp \left[ \frac{-R'^2}{4\sigma^2} \right] d^3R', \\
 &= (\pi \cdot 4\sigma^2)^{3/2}
 \end{aligned} \tag{12}$$

and

$$\begin{aligned}
 I_R &= \int \exp \left[ \frac{-(R-r)^2}{4\sigma^2} \right] v(|R|) d^3R. \\
 &= \exp \left[ \frac{-r^2}{4\sigma^2} \right] \int_0^\infty dR R^2 \exp \left[ \frac{-R^2}{4\sigma^2} \right] v(|R|) \times \\
 &\quad \int_0^\pi d\theta \sin \theta \cdot \exp \left[ \frac{-(R^2 - 2Rr \cos \theta)}{4\sigma^2} \right] \int_0^{2\pi} d\phi
 \end{aligned}$$

Carrying out the  $\phi$  and  $\theta$  integrations, we get

$$I_R = \frac{8\pi\sigma^2}{r} \exp \left[ \frac{-r^2}{2\sigma^2} \right] \int_0^\infty v(|R|) R \exp \left[ \frac{-R^2}{4\sigma^2} \right] \sinh \left( \frac{r}{2\sigma^2} R \right) dR \tag{13}$$

Let

$$\frac{r}{2\sigma^2} = \beta \tag{14}$$

Substituting eq. 12 and 13 for integrals  $I_{R'}$  and  $I_R$  respectively, in eq. 11, and also making use of the substitution given by eq. 14, we get

$$\langle v_{ij} \rangle = \frac{1}{\sqrt{\pi} \sigma r} \exp \left[ \frac{-r^2}{2\sigma^2} \right] \int_0^\infty v(|R|) R \sinh(\beta R) \exp \left[ \frac{-R^2}{4\sigma^2} \right] dR$$

... (15)

Now, we evaluate the above integral  $\langle v_{ij} \rangle$  for the NN potential and the Coulomb potential.

(a) NN Potential

$$v_{ij}^N(|R|) = -V_0 (1-C/R) \exp(-R^2/r_0^2) \quad (16)$$

Substituting eq. 16 in eq. 15, we get

$$\begin{aligned} \langle v_{ij}^N \rangle = & \frac{-V_0}{\sqrt{\pi} \sigma r} \exp \left[ \frac{-r^2}{2\sigma^2} \right] \left[ \int_0^\infty R \sinh(\beta R) \exp \left[ \frac{-R^2}{4\sigma^2} \right] \exp \left[ \frac{-R^2}{r_0^2} \right] dR \right. \\ & \left. - C \int_0^\infty \sinh(\beta R) \exp \left[ \frac{-R^2}{4\sigma^2} \right] \exp \left[ \frac{-R^2}{r_0^2} \right] dR \right] \quad (17) \end{aligned}$$

Let

$$\alpha^2 = \frac{1}{4\sigma^2} + \frac{1}{r_0^2} \quad (18)$$

with this substitution, eq. 16 becomes

$$\langle v_{ij}^N \rangle = \frac{-V_0}{\sqrt{\pi} \sigma r} \exp \left[ \frac{-r^2}{2\sigma^2} \right] \left[ \int_0^\infty R \sinh(\beta R) \exp(-\alpha^2 R^2) dR - C \int_0^\infty \sinh(\beta R) \exp(-\alpha^2 R^2) dR \right] \quad (19)$$

The two integrals in the above equation can be found in the tables of integrals, such as in Ref. 1 or evaluated easily, the results are

$$\int_0^\infty R \sinh(\beta R) \exp(-\alpha^2 R^2) dR = \frac{\beta}{4\alpha^2} \sqrt{\frac{\pi}{\alpha^2}} \exp \left[ \frac{\beta^2}{4\alpha^2} \right] \quad (20)$$

and

$$\int_0^\infty \sinh(\beta R) \exp(-\alpha^2 R^2) dR = \frac{1}{2} \frac{\sqrt{\pi}}{\alpha} \exp \left[ \frac{\beta^2}{4\alpha^2} \right] \operatorname{erf} \left[ \frac{\beta}{2\alpha} \right] \quad (21).$$

where  $\operatorname{erf}(x) = \frac{2}{\sqrt{\pi}} \int_0^x e^{-t^2} dt$ , is the error function

Substituting integrals eq. 20 and 21 in eq. 19, we get

$$\langle v_{ij}^N \rangle = \frac{-V_0}{\sqrt{\pi} \sigma r} \exp \left[ \frac{-r^2}{2\sigma^2} \right] \left[ \frac{\beta}{4\alpha^2} \sqrt{\frac{\pi}{\alpha^2}} \exp \left[ \frac{\beta^2}{4\alpha^2} \right] - \frac{C}{2} \sqrt{\frac{\pi}{\alpha^2}} \exp \left[ \frac{\beta^2}{4\alpha^2} \right] \operatorname{erf} \left[ \frac{\beta}{2\alpha} \right] \right] \quad (22)$$

$$= -V_o \left[ \frac{1}{(2\sigma\alpha)^3} - \frac{C}{r} \frac{1}{(2\sigma\alpha)} \operatorname{erf} \left( \frac{\beta}{2\alpha} \right) \right] \exp \left[ -\frac{r^2}{2\sigma^2} + \frac{\beta^2}{4\alpha^2} \right]$$

(23)

Substituting for  $\alpha$  and  $\beta$  from eq. 14 and 18, respectively, in eq. 23, and simplifying the argument of the exponential, we get

$$\langle v_{ij}^N \rangle = -V_o \left[ \frac{r_o^3}{(r_o^2 + 4\sigma^2)^{3/2}} - \frac{C}{r} \frac{r_o}{(r_o^2 + 4\sigma^2)^{1/2}} \operatorname{erf} \left( \frac{r}{2\sigma} \frac{r_o}{(r_o^2 + 4\sigma^2)^{1/2}} \right) \right] \cdot \exp \left( -\frac{r^2}{r_o^2 + 4\sigma^2} \right)$$

.. (24)

where  $r = |\langle r_i \rangle - \langle r_j \rangle|$  and  $\sigma$  is given by eq. 6.

## (b) COULOMB POTENTIAL

$$V_{ij}^C(R) = \frac{1.44}{R} \text{ (MeV)} \quad (25)$$

Substituting in eq. 15, we get,

$$\langle v_{ij}^C \rangle = \frac{1}{\sqrt{\pi}\sigma r} \exp\left[\frac{-r^2}{2\sigma^2}\right] \int_0^\infty \left[\frac{1.44}{R}\right] R \sinh(\beta R) \exp\left[\frac{-R^2}{4\sigma^2}\right] dR \text{ (MeV)} \quad (26)$$

$$= \frac{1.44}{\sqrt{\pi}\sigma r} \exp\left[\frac{-r^2}{2\sigma^2}\right] \int_0^\infty \sinh(\beta R) \exp\left[\frac{-R^2}{4\sigma^2}\right] dR \text{ (MeV)} \quad (27)$$

From eq. 21, we get,

$$\langle v_{ij}^C \rangle = \frac{1.44}{\sqrt{\pi}\sigma r} \exp\left[\frac{-r^2}{2\sigma^2}\right] \left\{ \frac{1}{2}\sqrt{\pi} \cdot 2\sigma \exp(\beta^2 \sigma^2) \operatorname{erf}(\beta\sigma) \right\} \text{ (MeV)} \quad (28)$$

$$\langle v_{ij}^C \rangle = \frac{1.44}{r} \operatorname{erf}\left[\frac{r}{2\sigma}\right] \text{ (MeV)}$$

(29)

## Reference:

I.S. Gradshteyn and I.M. Ryzhik, *Tables of Integrals, Series, and Products* (Academic Press, New York, 1965).

108281

A106281

## Date Slip

This book is to be returned on the  
date last stamped.

1  
M249  
4-19-83  
Reed, M. J.

PHY-1988-D-GOD-CLA